The interaction between physical and sedimentary biogeochemical processes in south-west Spencer Gulf, South Australia.

Emlyn Morris Jones B. Sc. (Hons)

A thesis submitted in fulfillment for the degree of

Doctor of Philosophy

School of the Environment

Faculty of Science and Engineering

Flinders University of South Australia

March, 2010

Contents

Abstract

Located in the south-west region of Spencer Gulf, South Australia, a multi-million dollar aquaculture industry based on the ranching of southern bluefin tuna (*Thunnus maccoyii*) contributes significantly to the regional economy. The interaction between aquaculture activities and the environment is of significant interest to industry stakeholders, management authorities and the broader science community. No studies, to the best of my knowledge, have investigated the relationships between the hydrodynamics and biogeochemistry of the system and the ability of the benthic ecosystem to deal with the increased loads of organic material from aquaculture activities. This thesis uses a multidisciplinary approach combined with modern statistical techniques to explore the linkages between hydrodynamics, sediment geochemistry, sedimentary nutrient cycling and the aquaculture industry.

Modelling results have identified that swell entering the mouth of Spencer Gulf from directly south causes the greatest swell heights in the central tuna farming zone. Winds from the north-east through to south-east generate the greatest wind-wave heights in the central tuna farming zone. This is directly related to the available fetch. The energy

contained in the locally generated wind waves was the same order of magnitude as that of the dissipated oceanic swells. Yet the incoming swell poses the greatest risk to aquaculture activities as the increased wave length causes swell energy to penetrate to the seafloor.

The results of this work suggest that the sediment geochemistry is tightly coupled to both the hydrodynamic regime and the buildup of silt originating from aquaculture activities. In the more exposed regions of the tuna farming zone, periodic resuspension events caused by swell propagating into the area from the Southern Ocean, resuspend fine unconsolidated sediments into the lower 10 m of the water column. This material is then advected through the region by the residual (low-frequency) currents until it settles out in areas of lower energy. This process has created two distinct provinces within the region that can either be classified as depositional or erosional.

The combined effect of wave action and tidal currents have generated a heterogeneous distribution of biogeochemical properties within the sediments. Denitrification rates were measured in these heterogeneous sediments using a novel technique based on Bayesian statistics to explicitly account for the spatial variability of the sediment biogeochemistry. The denitrification rates were found to be generally low, largely due to the lack of organic matter entering the sediments. However, adjacent to aquaculture activities, the high organic loads stimulate sedimentary denitrification, with rates reaching values of up to three orders of magnitude greater than the control sites. Denitrification efficiencies were high adjacent to the aquaculture activities, with up to

95% of the dissolved inorganic nitrogen produced from the breakdown of organic matter in the sediments being removed. Variability in the denitrifcation efficiencies was related to the textural characteristics of the sediments, with high efficiencies in finer sediments. It is proposed that this is due to the lower permeability of these sediments restricting the advective exchange of porewater nutrients.

Declaration

I certify that this thesis does not incorporate, without acknowledgment, any material previously submitted for a degree or diploma in any university; and that to the best of my knowledge and belief it does not contain any material previously published or written by another person except where due reference is made in the text.

Emlyn Jones

October 2009

Acknowledgments

When starting a PhD it can appear an insurmountable task. With suggestions, guidance and support from many people, this task became not only achievable, but enjoyable!

Firstly, I would like to thank my supervisors: Jochen Kämpf (Flinders University) and Milena Fernandes (SARDI Aquatic Sciences). Jochen, you captured my attention with Geophysical Fluid Dynamics and Numerical Modelling while an undergraduate, which inspired me to pursue this discipline as a career. Milena, thank you for introducing me to marine chemistry, your patience with me in this unfamiliar realm has been extraordinary. Without both of your guidance and suggestions, the diversity of topics covered in this thesis would not have been possible.

The funding for this thesis came from the Aquafin Co-operative Research Centre: Risk and Response project. I would like to acknowledge this support, for without the funding, it would not have been possible to conduct such an extensive field campaign.

Thank you to all the people who assisted with the field work and laboratory analysis. Especially Sonja Hoare (nee Venema), Kate Rodda, Brenton Ebert, Bruce Miller-Smith, Yvette Eglington, Mandee Theil, Gen Mount and

Jeremy Barnett (SARDI). The professionalism of the RV Ngerin crew - Neil Chigwidden, Ralph Putz, Dave Kerr and Chris Small, soothed my paranoid mind during the deployment and recovery of my moorings, without this data this project would not have had nearly some much observational data.

To those who supplied forcing data for the wave models; Graham Warren, Aihong Zhong and Bruce Brooks from the Australian Bureau of Meteorology. I also wish to thank Brenton Perkins, Bob Northeast and Mike Mellow from the Flinders University Mechanical Workshop for their help and patience in designing the moorings used in this thesis. ADCP's can be fickle devices, I would like to thank Miguel Gilcoto for his time and knowledge during the programming of these devices. Thank you to Greg Collings (SARDI), Doug Fotheringham (DEH), Murray Townsend (DEH) and Sue Murray-Jones (DEH) for supplying the wave observations for M10 and also supporting the wave modelling along the Adelaide metropolitan coastline.

I would like to acknowledge the support of the South Australian Partnership for Advanced Computing (SAPAC) for providing a platform to run the wave models.

Thank you Tina Hines for porewater nutrient analyses (Water Studies Centre, Monash University), Stuart McClure (CSIRO Land and Water) for geochemical elemental and isotopic analyses, and Jamie Woodward (MAFRL, Murdoch University) for phosphorus analyses. Furthermore, I wish to thank the recently retired John Dighton (CSIRO Land and Water) for spending weeks teaching me how to use a GC-IRMS, I hope you're enjoying your newly found freedom.

Peter Lauer for supplying the sedimentary inorganic nutrient flux data

used to estimate the net loss of nitrogen from the sediments in Chapter 6.

Throughout my time at Flinders University I had many fruitful discussions with other staff. Thank you to John Bennett, Paul Sandery and Matthias Tomczak for those stimulating discussions.

On a more personal note, thank you to my friends, your quiet support has kept me sane over the last four years. Those mid-week dinners and more recently trips down to Tassie have helped keep me grounded and in touch with the real world.

My parents, Meril and Michael, for supporting me both academically and throughout life. The freedom you've given me to explore has shaped who I am. My brothers Owen, Evan and Deinion; Sunday nights and weekends at the farm were a great outlet.

Finally, Jill. You have willingly shared this journey with me and for your understanding, patience and love, I cannot thank you enough! Weekends can finally be weekends, holidays will be holidays and I look forward to spending so much more time with you in our new home!

Chapter 1

General introduction

The 3000 km southern coastline of Australia extends from Cape Leeuwin in the west to South-East Cape in Tasmania (Figure 1.1). Along sections of the shelf, strong upwelling during the months of January to April brings cool nutrient-rich water into the photic zone (Middleton & Bye, 2007), enhancing primary productivity in an otherwise oligotrophic ocean. This primary productivity supports vast schools of sardines (McClatchie *et al.* , 2007), which in turn are targeted by predators such as southern bluefin tuna (*Thunnus maccoyii* hereafter referred to as SBT), in higher trophic levels. Over 95% of Australia's quota of SBT are caught along the continental shelf of central South Australia. In response to the reduction of the SBT quota in the early 1990's a value-adding process, whereby the SBT are fattened over a 6 month period, has been adopted by the industry. The SBT are caught near the shelf break in the eastern Great Australian Bight, then towed to south-west Spencer Gulf (Figure 1.2). The SBT are then transferred to pontoons (Figure 1.3) in the tuna farming zone (TFZ), where they are fattened and then

harvested for export, often to Japan. The interaction between the aquaculture activities and the environment in the TFZ are of considerable interest to the tuna industry and management authorities.

Prior to 1996 the TFZ was mostly located within the sheltered Boston Bay, adjacent to Port Lincoln. In April of 1996, a severe weather event caused a widespread sediment resuspension episode which led to the mortality of up to 75% of fish (Clarke, 1996). Subsequently the TFZ was fully relocated to the more exposed region to the east of Boston Island, where it is thought that the more energetic conditions will decrease the amount of waste material deposited under the tuna pontoons. This chapter describes the regional setting of this area, introduces previous research and presents the aims and objectives of this thesis.

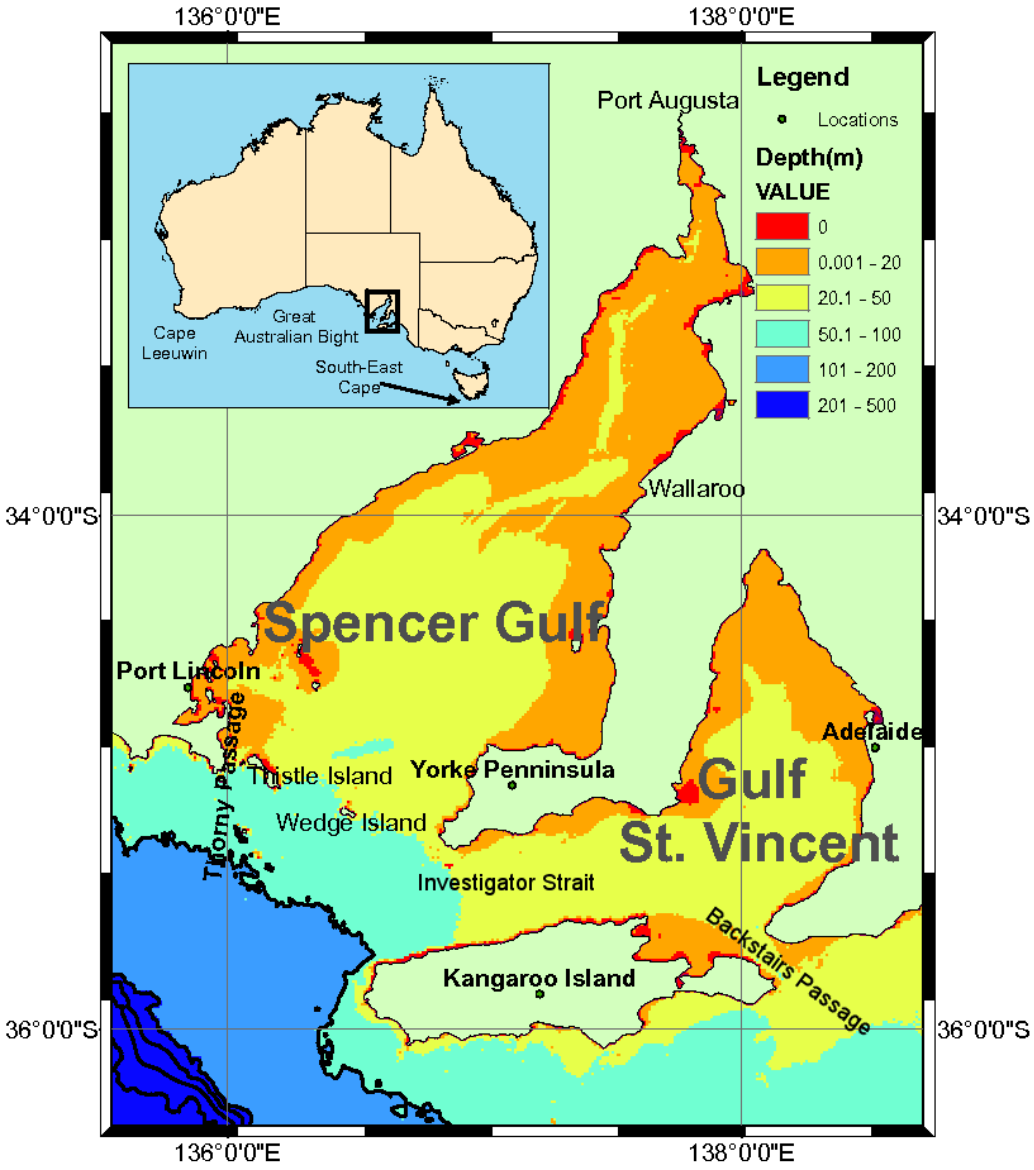

Figure 1.1: The central South Australian coastline depicting the major features of Spencer Gulf, Gulf St Vincent and Kangaroo Island.

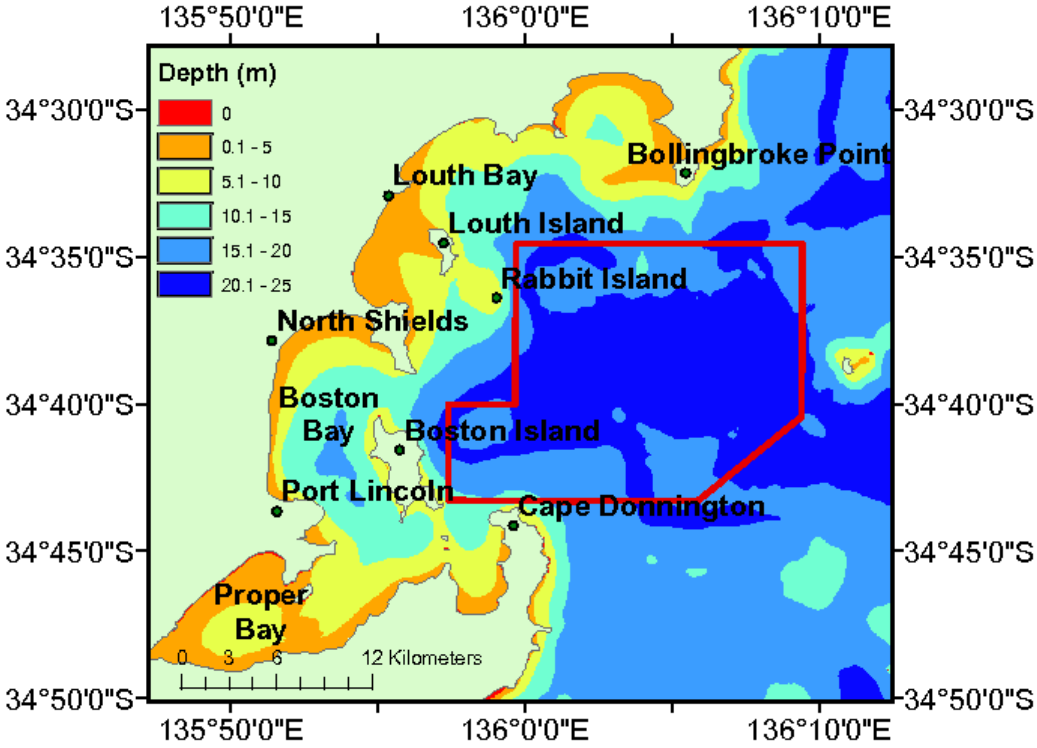

Figure 1.2: The south-west region of Spencer Gulf with the post 1996 tuna farming zone denoted with the red border.

Figure 1.3: A pontoon used for the farming of southern bluefin tuna.

1.1 Regional setting

1.1.1 Bathymetry

The dominant features of the central South Australian coastline are Gulf St Vincent, Spencer Gulf and Kangaroo Island (Figure 1.1). The southern entrance to Spencer Gulf contains a number of small islands on its western side, including Thistle Island and a small group in the centre dominated by Wedge Island. Kangaroo Island lies directly south of Gulf St Vincent and is separated from the mainland by two passages of water, Investigator Strait and Backstairs Passage. Most of the coastlines in the region are low and rocky, consisting of limestone and carbonate sediments. The continental shelf extends some 80-200 km south of the mainland and Kangaroo Island to the shelf break where it abruptly drops to the abyssal plain at 4000 m depth. Several submarine canyons bisect the shelf break to the south of Kangaroo Island. These canyons have recently been the subject of process studies and surveys with regard to their role in upwelling events and the supply of nutrients to shelf waters (McClatchie *et al.* , 2006; Kämpf, 2007).

1.1.2 Physical oceanography

Within this region the physical oceanography has been of great interest in recent years. The shelf circulation is complex with the Flinders current following the shelf break at depths of between 200 - 500 m (Middleton & Bye, 2007). The influence of synoptic weather patterns generates coastally-trapped waves which propagate to the east, particularly in the summer months. It is unclear

if and how these waves modify the circulation in the Gulfs (Middleton & Bye, 2007). As suggested by Kämpf (2007) the presence of shelf break canyons may aid in the transport of cool deep nutrient-rich water on to the shelf. This, in conjunction with the well understood Ekman generated upwelling, suggests the presence of a pool of cold, nutrient-rich water that resides on the shelf west of Kangaroo Island, persisting through the summer months (McClatchie *et al.* , 2006).

Historically, Spencer Gulf has been studied in detail and the circulation has been described by a number of authors (Noye, 1984; Nunes & Lennon, 1986; Lennon *et al.* , 1987; Petrusevics, 1993). There is agreement that Spencer Gulf is an inverse estuary whereby the salinity increases towards the north. Furthermore, it has been suggested by Lennon *et al.* (1987), and confirmed with satellite imagery (Petrusevics, 1993), that due to heating in summer a density front establishes across the mouth of the Gulf. This front limits the exchange between Gulf and oceanic waters. Recent evidence suggests that some of the upwelled water may actually cross the density front in the lower layers, occasionally reaching the TFZ (Herzfeld *et al.* , 2009). During winter, a gravity current forms and flows down the eastern side of Spencer Gulf spilling on to the shelf and down the du Couedic canyon on the shelf break (Lennon *et al.* , 1987) (Figure 1.4).

The circulation within Spencer Gulf can be divided into two distinct regions; the southern region, extending from the entrance up to Wallaroo, and the northern region from Wallaroo to the head of the Gulf near Port Augusta. The southern region exhibits weak residual clockwise circulation which is a result of the local wind forcing (Herzfeld *et al.* , 2009). During

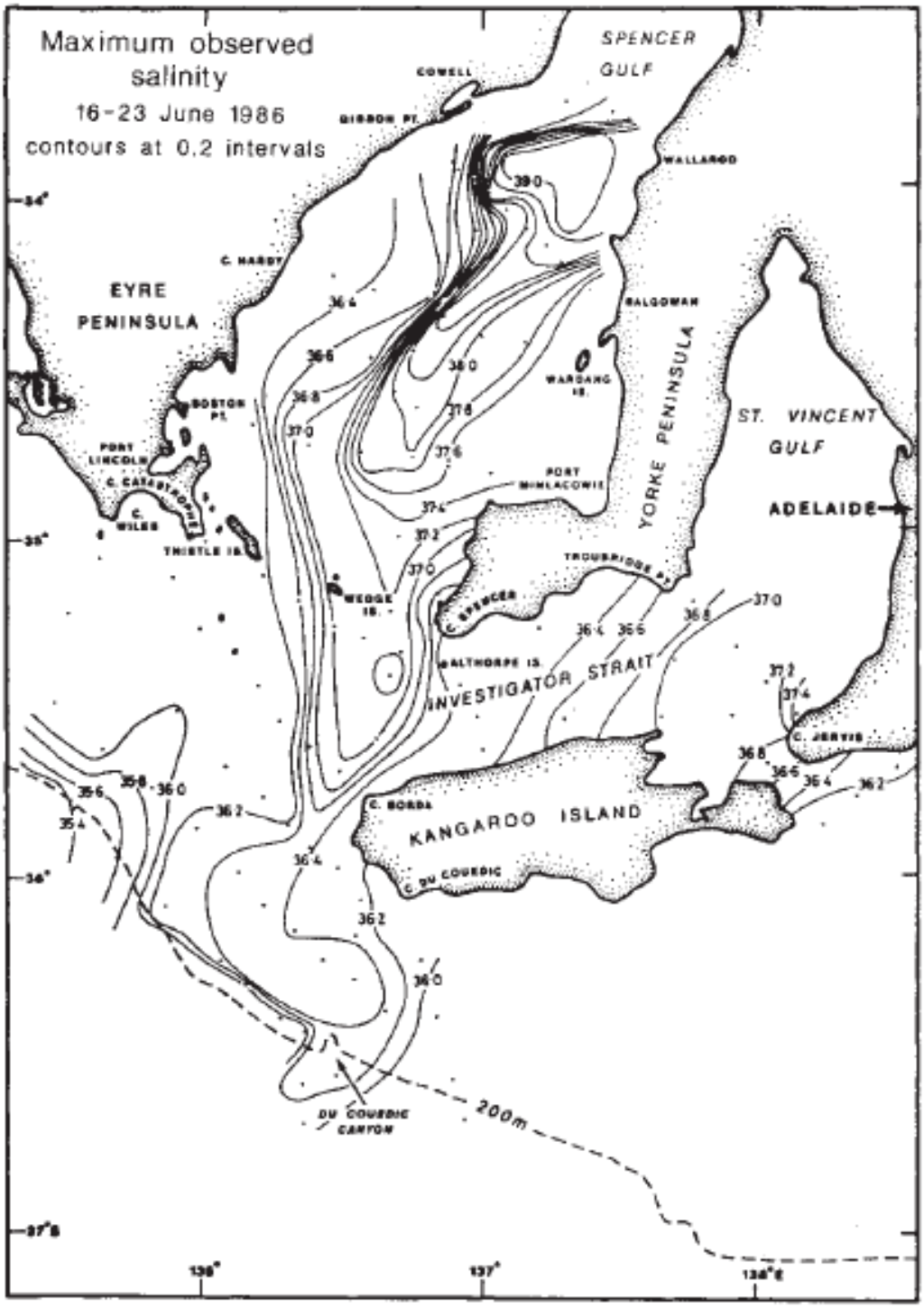

Figure 1.4: A salinity contour map depicting the location of the dense gravity current formed during the Austral winter (Lennon *et al.* , 1987).

summer the evaporation rates in the northern region produce a warm salty watermass that remains isolated from the southern region. During autumn, this water mass cools and trickles down the eastern side of the Gulf and can be seen in many conductivity, temperature and depth (CTD) observations as a cold, salty water mass (Lennon *et al.* , 1987). It is this thermohaline exchange that forces the flushing of northern Spencer Gulf (Kämpf *et al.* , 2009). Monthly averaged temperature-salinity diagrams for various stations in the Gulf clearly display the seasonal flushing signature (Figure 1.5).

The tidal regime of Spencer Gulf is unusual. The tidal elevations are < 2 m in the southern section of the Gulf, leading to it being classified as micro-tidal in nature. The tidal elevation increases towards the head of the Gulf due to tidal resonance. Port Augusta at the head of the Gulf experiences 3-4 m tides and is on the verge of being classified as macro-tidal. Its most unusual feature is that it experiences the 'dodge' tide. This is a phenomena whereby the diurnal and semi diurnal tidal constituents are of the same magnitude and when there is a 180 degree phase difference, the combined effect of the signals cancel each other out and cause little if any tidal movement over the 12 hour cycle. This dodge tide occurs every lunar cycle. The dodge tide can have a profound effect on the biology of the region; due to lack of tidal movement, the dissolved oxygen (DO) drops to near anoxic levels in some regions.

Initial attempts at modelling the hydrodynamic regime of the TFZ are contained in Grzechnik (2000), with more recent high resolution 3-D modelling reported in Herzfeld *et al.* (2009). Typical flushing times for the TFZ are approximately 2 days, whereas in the more sheltered Boston and Proper

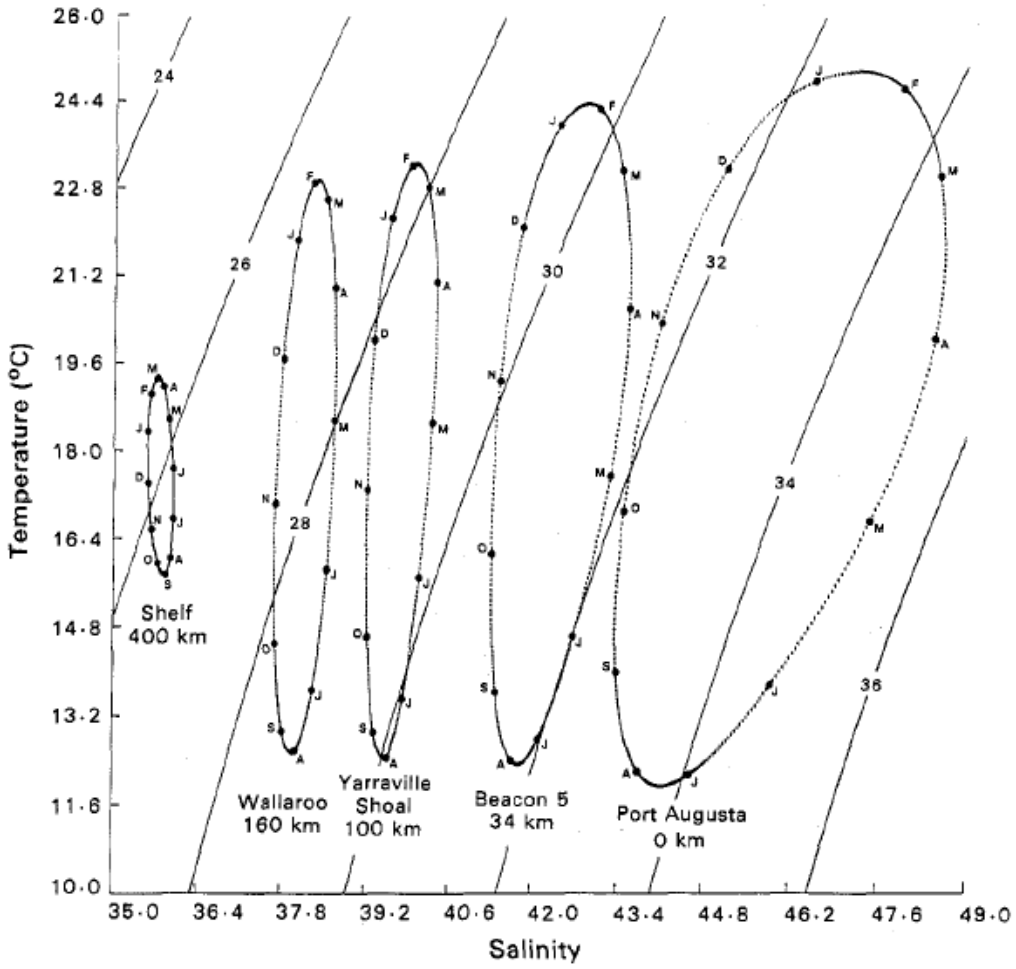

Figure 1.5: The seasonal temperature and salinity cycles at various locations in Spencer Gulf. Due to negligible riverine inflow, changes in salinity are caused by exchange with fresher oceanic water (Nunes & Lennon, 1986).

Bays, the flushing times are longer and are of the order of 8-10 days. The tidal currents in this part of the Gulf are reasonably strong and reach a maximum speed of around 20 cm s^{-1}, which have the ability to generate displacements of particles of up to 8 km in a tidal cycle. In contrast to the tidal currents, the observed and modelled residual circulation is weak, with typical speeds in the order of 1 cm s^{-1}. The combined effect of the tidal and residual flow creates distinct subregions having limited connectivity (Figure 1.6). The exchange between the coastal regions and the TFZ is enhanced during summer in response to local upwelling generated by easterly winds.

Very few studies have investigated the wave regime of the gulfs of South Australia. The swell climate of Spencer Gulf was first mentioned in Noye (1984), who presented results detailing the persistence of oceanic swell along the north-south axis of Spencer Gulf. The first wave-modelling study of this region was conducted by Hemer & Bye (1999), who investigated the attenuation of oceanic swell over the continental shelf and who empirically fitted equations predicting swell height at various coastal locations using the oceanic swell height, period and direction at the shelf break. The first study to investigate the combined effects of swell and wind waves was that of Pattiaratchi *et al.* (2007), which was confined to Gulf St Vincent.

1.1.3 Sediments

Recent 3-D sediment modelling studies of this region are contained in Margvelashvili (2009) and are forced with the output of the wave model from Chapter 2 of this thesis. The findings of Margvelashvili (2009) suggest that fine sedi-

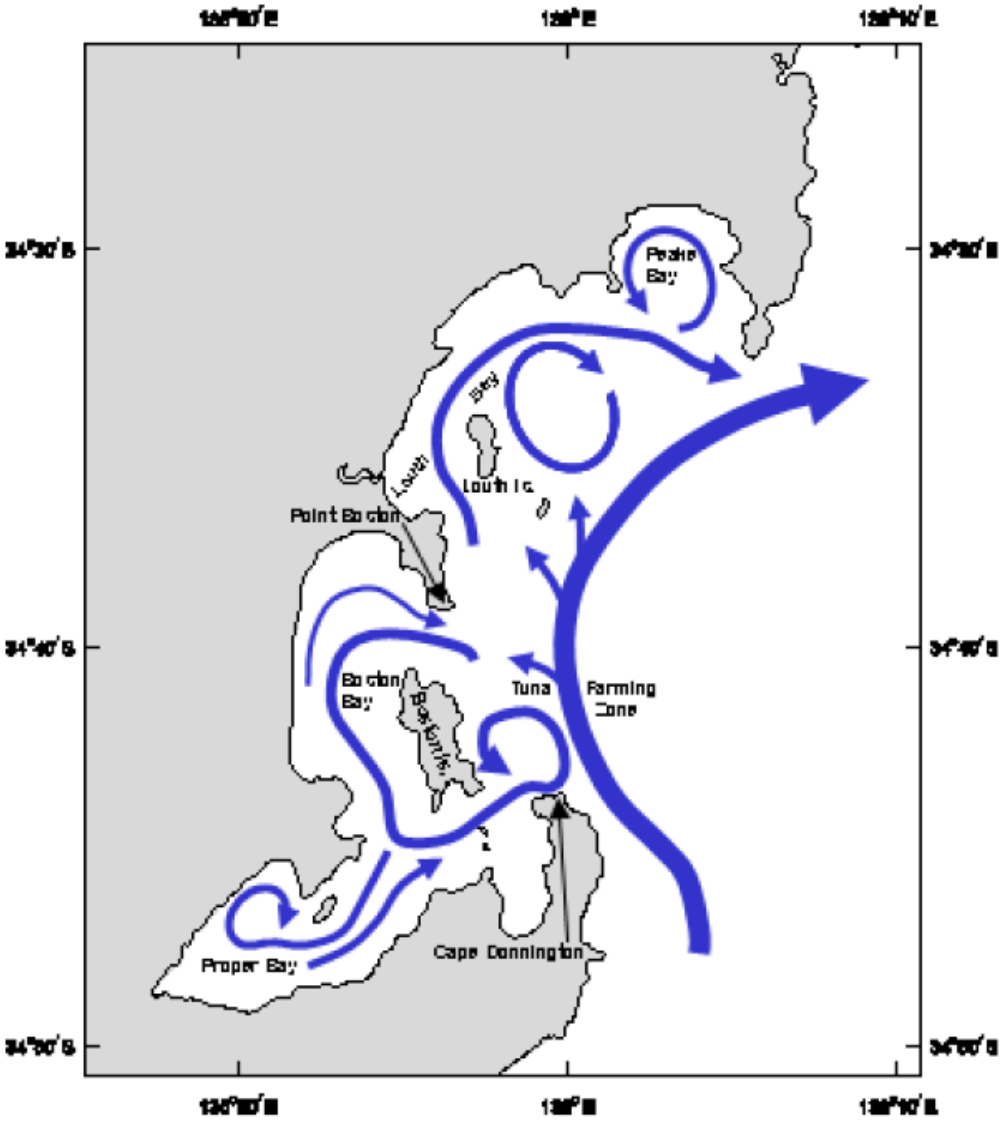

Figure 1.6: The mean depth integrated currents in the TFZ (Herzfeld *et al.* , 2009).

ments are resuspended regularly and are derived from fresh sediment deposits or unconsolidated layers. The probability of sediment resuspension on the western side of Boston Island and in Proper Bay is the lowest in the model domain. The model also suggests the potential for unconsolidated sediments in the central region of the TFZ to be resuspended (Figure 1.7).

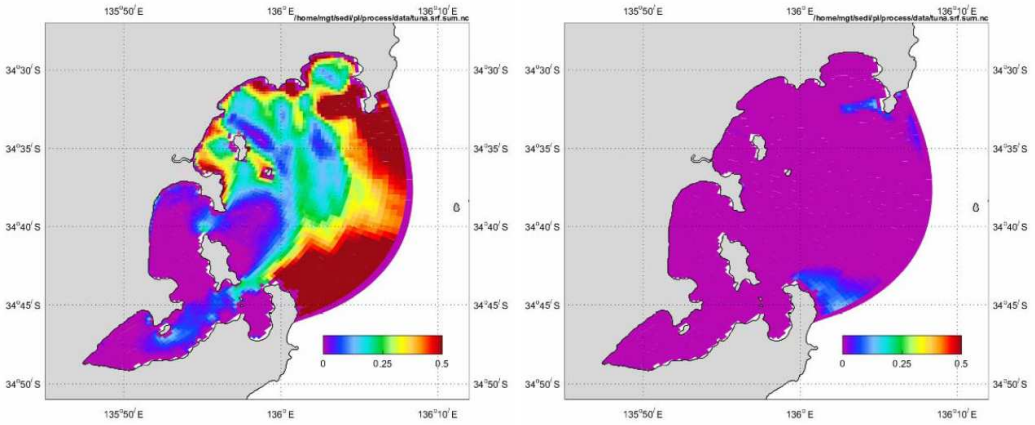

Figure 1.7: The simulated probability of sediments becoming resuspended for a critical friction velocity of 0.014 m s^{-1} (left) and for a critical friction velocity of 0.005 m s^{-1} (right) (Margvelashvili, 2009).

Since the 1996 tuna mortality event, there has been significant interest in defining the regional sediment types in SW Spencer Gulf. The sediments in this region are discussed in Fernandes *et al.* (2006), and are a mixture of sediments found on the shelf and those further north. The sediment type on the adjacent continental shelf is dominated by calcareous sediments from the erosion of carbonate deposits (Harris, 1994). Sediment transport on the shelf is dominated by wave-induced transport as a result of storm activity; this transitions to tidally-induced sediment transport in Spencer Gulf (Porter-Smith *et al.* , 2004). Observations presented in Fernandes *et al.* (2006) suggest that in SW Spencer Gulf a mixture of the two processes causes the

winnowing out of fine sediment fractions at more exposed locations; this is supported by the findings of Margvelashvili (2009).

1.2 Aquaculture

Throughout the world, there has been an ever increasing demand for seafood. As a direct result of this increasing demand and declining wild fish stocks, aquaculture has grown dramatically. Aquaculture practices vary widely depending on the geographic location and demand for various fish species. In North America, Northern Europe, New Zealand and Tasmania salmonid farming using pellet feeds is common. Within these regions the interaction between the aquaculture activities and the environment differs due to regional environmental characteristics. Typically, environmental impacts arise from high organic and nutrient loadings derived from uneaten feed and excreted waste from the farmed species (Wu, 1995). If the inherent hydrodynamics do not disperse the waste, the accumulation of organic matter on the seafloor can lead to changes in benthic communities (Vita & Marin, 2007). In extreme cases, it has been found that the high nutrient loads can lead to eutrophication, similar to that caused by other anthropogenic activities. Such events have resulted in harmful algae blooms causing the mass fatalities of farmed fish (Diego-McGlone *et al.* , 2008). Kalantzi & Karakassis (2006) have reviewed the issues of benthic impacts from marine fish farming and found that depth, distance from pontoon and latitude of aquaculture site, were the best predictors of sediment geochemistry.

Within Australia, there are three major finfish aquaculture regions; the

Huon-D'Entrecastuex Channel and Macquarie Harbour in Tasmania and Spencer Gulf in South Australia. Previous studies in the Huon-D'Entrecasteaux Channel have used a combination of field studies and biogeochemical (BGC) modelling to investigate the interaction between aquaculture and the environment (Wild-Allen *et al.* , 2004). BGC modelling can be used as a tool to simulate various scenarios accounting for variations in environmental forcings or increased/decreased nutrient loads from point sources. These studies have played an important role in informing management authorities on how aquaculture activities should be managed and potential carrying capacities of the aquaculture zones.

Research in the TFZ in SW Spencer Gulf has previously examined the effects of aquaculture on the seafloor (Lauer, 2005), finding that aquaculture activities significantly stimulated benthic metabolism. Nutrient fluxes from the sediments were found to follow a distinct seasonal cycle that coincides with the tuna farming season. A conceptual model of the nitrogen metabolism of SBT found that approximately 7 -18 % of the nitrogen that enters the system from tuna feed is deposited on the seafloor as particulate organic nitrogen (PON) (Figure 1.8)(Fernandes *et al.* , 2007b). Less than half of this PON is stored in the sediments while the remaining fraction diffuses into the water column. It is unclear from previous studies how much nitrogen is removed from the system through the process of denitrification.

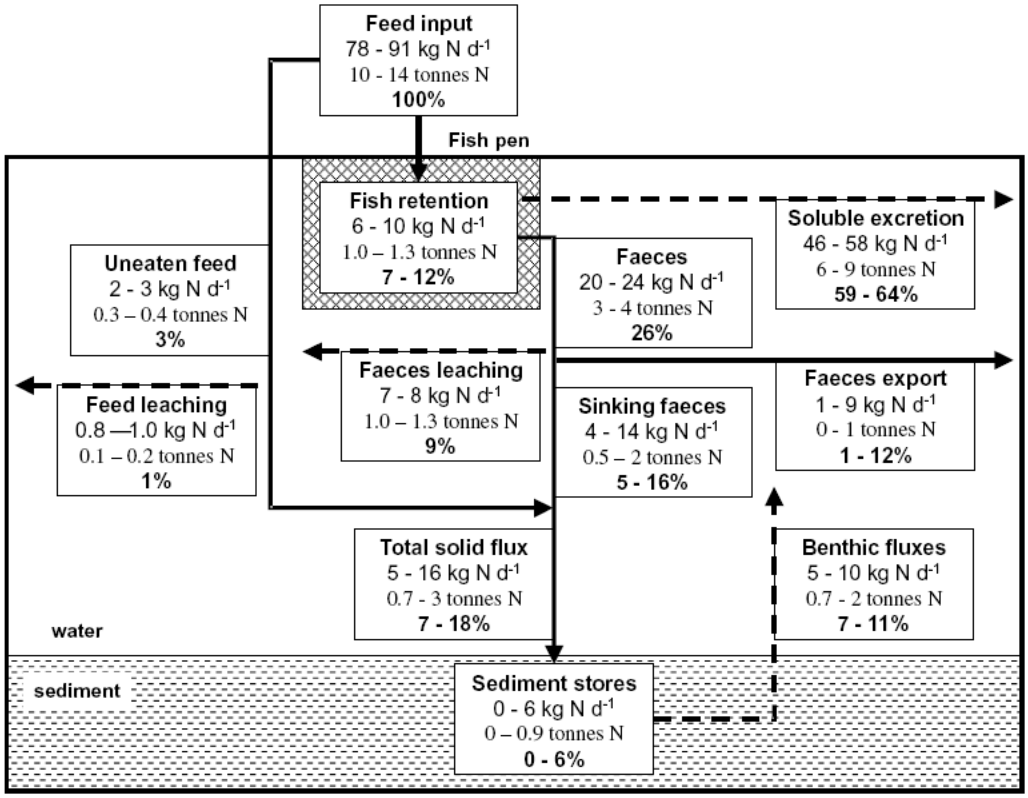

Figure 1.8: A conceptual model of the environmental flow of nitrogen entering a tuna pontoon with tuna feed (Fernandes *et al.* , 2007b).

1.3 Nutrient cycling and benthic metabolism

Nitrogen in the coastal marine ecosystem (Figure 1.9) is often thought of as the major limiting nutrient that controls primary productivity being cycled through a number of different and often complex pathways (Hecky & Kilham, 1988; Herbert, 1999). Nitrogen, in the form of Dissolved Inorganic Nitrogen (DIN), comprising of nitrite (NO_2^-), nitrate (NO_3^-) and ammonia (NH_4^+), are the most readily bioavailable forms of nitrogen. DIN can either be advected into a coastal region or other forms of nitrogen can be transformed into DIN locally. Within coastal marine ecosystems, the advective flux of DIN can be derived from the lateral advection of nutrient rich water through the process of upwelling. Local fluxes can be derived from river input, anthropogenic sources such as effluent discharge, aquaculture activities or through ecosystem transformations such as mineralisation, nitrogen fixation, nitrification to name a few (Figure 1.10). Removal of DIN from coastal ecosystems may occur via similar pathways. Nutrient rich waters can be advected and subjected to downwelling, and there can be losses of DIN through microbial processes.

A major pathway through which DIN is lost from the benthic ecosystem is through the process of sedimentary denitrification. Denitrification transforms nitrate into N_2 gas, at which point nitrogen is no longer considered a biologically available. The process of sedimentary denitrification is tightly linked to the microbial community. In coastal environments most denitrification takes place in the anoxic zone of the sediments. Where regions experience strong tidal flows or oscillatory motion associated with surface gravity waves, there is often substantial spatial variation in microbial communities

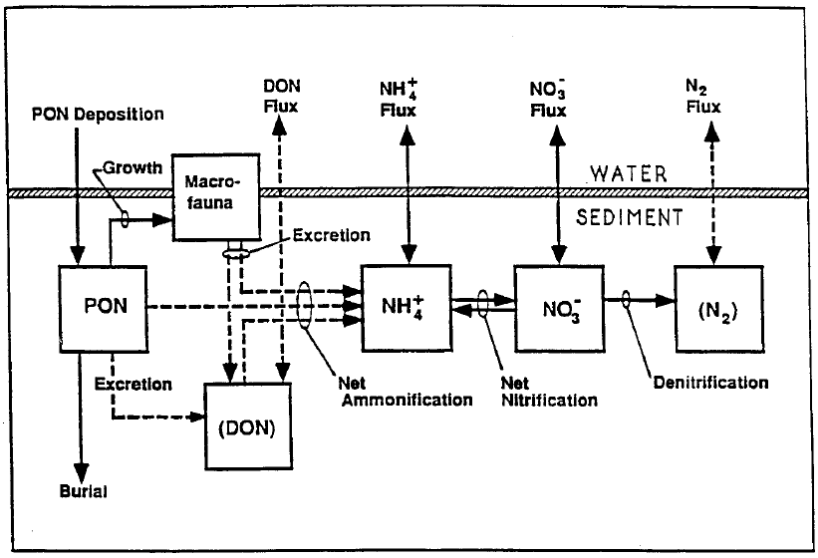

Figure 1.9: The idealised marine nitrogen cycle (Kemp *et al.* , 1990).

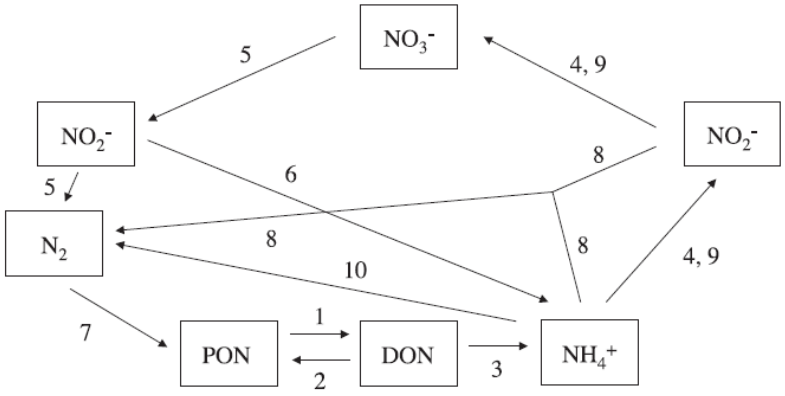

Figure 1.10: A schematic diagram detailing the processes responsible for transformation amongst various species of nitrogen present in the marine environment. Hydrolysis of organic polymers (1), biological incorporation (2), ammonification (3), nitrification (4), denitrification (5), dissimilatory nitrate/nitrite reduction to ammonium (DNRA) (6), nitrogen fixation (7), anaerobic ammonium oxidation by nitrite (Anammox) (8), and anaerobic ammonium oxidation to nitrite and nitrate (9) or N_2 (10) (Hulth *et al.* , 2005).

over very short length scales (Cardenas *et al.* , 2008).

1.4 Aims of this thesis

In this thesis the interaction between the physical environment and the biogeochemistry of the sediments is investigated using a multidisciplinary approach. The goals of this thesis are:

- To determined the combined swell and wind wave regime of south-west Spencer Gulf using a combination of in situ and remotely sensed observations and numerical modelling using SWAN.
- To investigate the interaction between the wave regime of south-west Spencer Gulf and the sediment dynamics, including sediment resuspension the transport of sediments in the TFZ. A combination of modelling, observations and theoretical sediment dynamics are applied.
- Using the wave modelling results and observed sediment distributions, a sea-floor classification is developed and its relationship with aquaculture activities is explored?
- The *in situ* denitrification rates and related spatio-temporal variability is explored using a new, innovative statistical technique, the implications of these findings are then discussed in the context of the regional aquaculture industry.

1.4.1 Structure

The thesis is structured such that each Chapter is a paper or at the very least can be read as a standalone document. Inevitably there will be some repetition in the Introductions to the Chapters, which is unavoidable given the structure. The thesis is divided into two parts:

- Part 1: The physical oceanography of south-west Spencer Gulf,
- Part 2: The sediment biogeochemistry of south-west Spencer Gulf.

Part 1 is divided into two chapters based on field studies and numerical modelling: the first is a detailed investigation into the combined swell and wind wave regime of the area, while the second examines the relationship between waves, sediment resuspension and the textural characteristics of the sediments.

Part 2 contains a further three chapters investigating small and large scale spatial variations in sediment geochemistry and denitrification. These distributions and processes are then related back to the physical conditions and anthropogenic inputs to this area.

This is the first detailed study that has investigated the interactions between the physical forcings, anthropogenic inputs through aquaculture and sediment biogeochemistry within south-west Spencer Gulf and to the best of my knowledge in any temperate oligotrophic region.

Part I

Physical Oceanography

Chapter 2

The wave regime

2.1 Introduction

Coastal areas within the South Australian gulfs are of high economic importance to both the fishing and aquaculture industries. Since 1991, more than 95% of Australia's southern bluefin tuna quota has been farmed in south-west Spencer Gulf near Port Lincoln. In April of 1996 a sediment resuspension event led to mass fatalities of captive tuna, resulting in the loss of millions of dollars to the industry. Since this event, management practices have been modified and the tuna farming zone has been relocated from the relatively sheltered region west of Boston Island, to the more exposed eastern side of Boston Island (Figure 2.1). It is thought that in the more energetic region to the east of Boston Island, detrital matter from aquaculture activities will be dispersed over a wider area, rather than accumulating below the tuna pontoons. However, there have been no reported observational or modelling studies that characterise the wave regime of the current tuna farming zone.

Knowledge gained from these studies is imperative in understanding the interactions between the physical and biogeochemical nature of this region.

Numerical wave models used in coastal locations have undergone a series of progressions during the past two decades. With the increased computational power available, more complex numerical solutions have been implemented and higher resolution grids can be used (Cavaleri *et al.* , 2007). In the current third generation of models the processes of nonlinear wave-wave interactions (triads and quadruplets), refraction, shoaling, effects of bottom friction and white-capping are all included (Booij *et al.* , 1999). Several such models are in the public domain. One of the most common and publicly available models is the Simulating WAves Nearshore (SWAN) model, which is used in this study.

Whitecapping still presents a major challenge within wave modelling. It remains one of the least understood processes (Cavaleri *et al.* , 2007). A variety of methods have been proposed to calculate the dissipation rates that result from whitecapping, and it has been suggested that such dissipation terms are largely 'tuning parameters' for wave models (Babanin & van der Westhuysen, 2008). The pulse-based method of Hasselmann *et al.* (1973) was used in the Komen *et al.* (1984) formulation, which forms the basis of the default (KOMEN) scheme used by the SWAN model, often referred to as the WAM cycle 3 formulation. The KOMEN scheme relies on the spectral mean frequency. A number of studies have investigated this reliance on the spectral mean frequency, and have noted certain applications where this scheme can lead to poor model performance. In particular, when there is a bimodal spectrum, where swell and wind waves are present, this formulation has been

shown to over-predict the total wave energy (Rogers *et al.* , 2003). The second available scheme for use within SWAN is the method using the formulation of Janssen (1991). The JANSSEN scheme still uses the formulations of Komen *et al.* (1984), but the transfer of energy from the wind to the ocean surface is dependent on the wave spectrum. This formulation still suffers from its dependence on the spectral mean frequency. An alternative to the Komen *et al.* (1984) formulation was proposed by Alves & Banner (2003). This is a saturation-based method that is local in frequency space, removing the dependence on whitecapping from the spectral mean frequency. A modified version of this saturation-based method (WESTHUYSEN scheme), has been incorporated into the SWAN model and is presented in van der Westhuysen *et al.* (2007).

In this study, SWAN has been applied to investigate the wave regime in the gulfs of South Australia and also on the adjacent continental shelf (Figure 2.1). The southern coastline of Australia is subject to high amounts of incident wave energy in the form of swell waves propagating towards the coastline from the Southern Ocean. As the incoming swell encounters the progressively shallower waters, it undergoes a number of transformations due to refraction, shoaling, breaking and non-linear wave-wave interactions (Holthuijsen, 2007). The continental shelf width varies from between 30-40 km along the south-eastern South Australian coastline, up to 200-300 km in the central Great Australian Bight. The central coastline of South Australia is characterised by two gulfs that extend inland from the shelf for 300 km. The wave regime in these gulfs is a combination of incoming swell from the Southern Ocean and locally generated wind waves, suggesting that

in a number of coastal locations bimodal (swell and wind wave) spectra will be present.

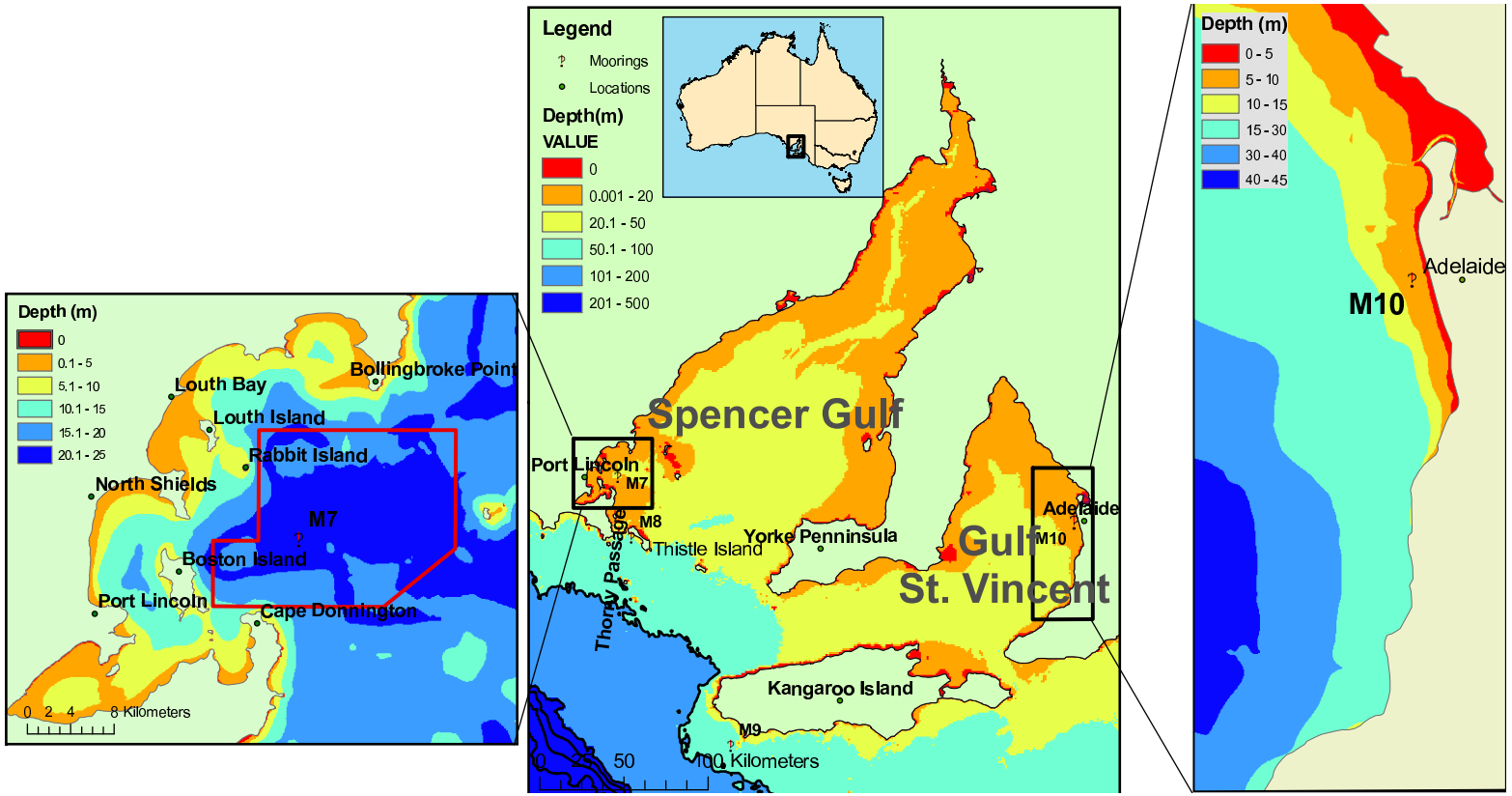

Figure 2.1: In this study, 4 model domains were used; a coarse resolution grid (centre), covering the central South Australia coastline, extending from the continental shelf to the head of Spencer Gulf and Gulf St. Vincent, two finer resolution grids, covering SW Spencer Gulf (left) and the Adelaide metropolitan coastline (right) nested within the coarse resolution grid. A fourth very high resolution grid (not shown) nested within the Adelaide Metropolitan coastline model, was required to adequately resolve the fine scale features present in the near-shore zone. The moorings (M7, M8, M9, and M10) used in the assessment of the wave model are shown as red dots in the figure.

Previous studies into the swell height (H_{swell}) and wave characteristics of Spencer Gulf have found that little or no swell ($H_{swell} < 5$ cm) is present in its upper reaches and waves with a period >6.5 s are present for less than 1% of the time in the central regions of the Gulf (Noye, 1984). Hemer & Bye (1999) present the first wave modelling study on this area, in which only the incident swell is used to force the model. H_{swell} within Spencer Gulf and Gulf St. Vincent is highly sensitive to the approaching incident swell direction to the west of Kangaroo Island. A wave model has been applied to Gulf St. Vincent, in the eastern region of the present study area, as part of the Adelaide Coastal Waters Study (ACWS) (Pattiaratchi *et al.* , 2007). The model used for the ACWS was SWAN, running in default mode (using the KOMEN option) and forced by a homogenous wind field over the entire model domain. The open sea boundary was forced with the significant wave height (H_s), peak period (T_p) and peak period direction (T_d) obtained from the global Wave Watch 3 (WW3) model. When compared with field data it was found to over-predict the significant wave height by up to 50% during periods of low wave height, and to under-predict the wave height during peak events by approximately 20%. However, it is likely that, due to the presence of both swell and wind waves, the default third generation physics scheme within SWAN, based on the formulations of Komen *et al.* (1984), contributed to these errors.

There have been no modelling studies that have investigated the combined swell and wind-wave characteristics in the region of the tuna farming zone or Spencer Gulf. The purpose of this study was to apply the SWAN model to the area and compare the results obtained using the formulations of Komen

et al. (1984), Janssen (1991) and van der Westhuysen *et al.* (2007) to identify the physics scheme that gave the best agreement with observational data. The wave model was then used to study, at a number of locations within the South Australian gulfs, the mean and storm-induced wave heights and also the relative effects of incoming swell and locally generated wind waves. To this end, SWAN was used to study the wind wave evolution and impact of swell over a two year period from September 2005 to September 2007. The output from the calibrated and validated wave model was then used in later chapters to interpret the spatial variability in a number of observed biogeochemical variables. Furthermore, the output from this wave model contributed forcing data to a larger project in which a coupled 3-D hydrodynamic-sediment-biogeochemical model was used to investigate the physical and biological regime of the tuna farming zone (Tanner & Volkman, 2009). Table 2.1 is a list of symbols and abbreviations used in this chapter.

Table 2.1: List of symbols and abbreviations used in Chapter 2.

Symbol	Description	Value	Units
H_{swell}	Swell Height	-	m
H_s	Significant Wave Height	-	m
T_p	Peak Wave Period	-	s
T_m	Mean Wave Period	-	s
T_d	Peak Period Wave Direction	-	°N
c	Wave Phase Speed	-	m s^{-1}
E	Energy Density	-	m^2 Hz^{-1}
Δx	Grid Spacing in the x-direction	-	degrees
Δy	Grid Spacing in the y-direction	-	degrees
$\Delta\theta$	Discrete directional grid	10	degrees
Δf	Discrete frequency grid	-	Hz
Δt	Discrete time step	-	s
C_{wc}	Whitecapping coefficient	1.75 x 10^{-5}	-
g	Gravity	9.8	m s^{-2}
k	Wave number	-	m^{-1}
d	Depth	-	m
ER	Energy Ratio	-	-

2.2 Methods

2.2.1 Wave observations

In situ observations

The wave model used in this study was validated against four *in situ* observational datasets. Wave observations in areas with high amounts of shipping activity are a trade-off between the accuracy gained by using a Waverider buoy and the safety of using a bottom mounted Acoustic Doppler Current Profiler (ADCP). In this study, shipping activity mandated the use of an ADCP; a 300 kHz RDI Workhorse Sentinel Wave Gauge employing a Janus configuration for the transducer heads (Figure 2.2). Traditionally the high frequency Pressure, U and V orbital velocity (PUV) method is used to derive the wave spectrum. However, when using a four head broadband ADCP, the along-beam radial velocities or acoustic surface tracking can instead be used. The PUV method suffers from the attenuation of the dynamic pressure signal with depth leading to a cutoff frequency of approximately 0.2 Hz when deployed in 20 m of water. By using a combination of along-beam radial velocities and surface tracking, the device used in this study increases this cutoff frequency to 0.4 Hz, leading to a more reliable estimate of the wave spectrum. Three deployments were successfully undertaken at different locations; details of the deployments can be found in Table 2.2 and Figure 2.1.

Figure 2.2: An example of the ADCP mooring used at M7, M8 and M10.

Table 2.2: The location of the moorings used in the assessment of the wave model.

	M7	M8	M9	M10
Latitude (S)	34.67	35.1	36.02	34.9
Longitude (E)	136.04	136.08	136.62	138.42
Depth (m)	22	43	70	7
Instrument	ADCP	ADCP	1-D Waverider	ADCP
Deployed	12/7/07	4/10/07	2002	19/1/07
Recovered	19/7/07	27/11/07	Ongoing	19/2/07

Remotely sensed observations

A temporal and spatial assessment of the coarse resolution wave model was performed using remotely sensed data. The remotely sensed data used in this study was obtained from the altimeter onboard the ENVIronmental SATellite (ENVISAT) operated by the European Space Agency (ESA). Altimeters are subject to a number of errors that need to be considered when using them in the coastal ocean. When the altimeter has any land within the footprint, this will result in erroneous wave heights. Similarly, when the satellite transitions from land to water there is a time-lag for the altimeter to adjust. To account for these known characteristics, all data points that fell within 20 km of land and points that were marked with 'bad data' flags were rejected. The remaining data points were then used in the spatial assessment of the coarse resolution domain (Figure 2.3). Over a two year period there were $>$ 3200 points used in the assessment. A far more detailed description of satellite-based wave measurements can be found in Hauser *et al.* (2005) and Holthuijsen (2007).

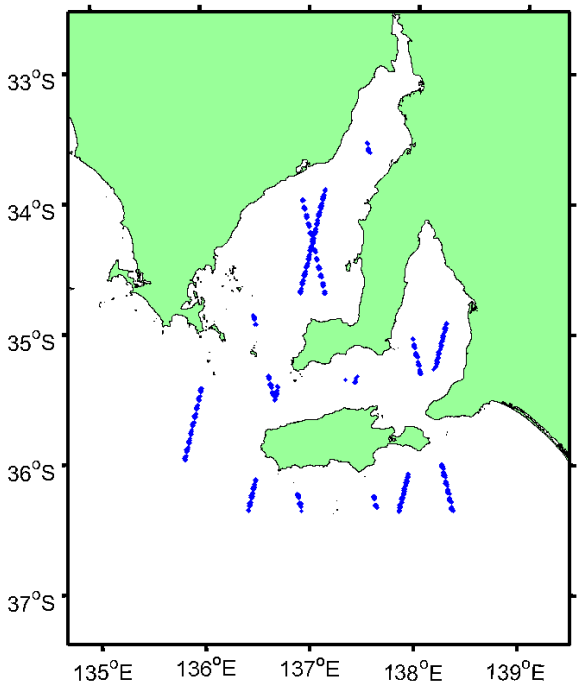

Figure 2.3: A map with the locations of the ENVISAT altimeter measurements used in the spatial assessment of the wave model.

2.2.2 Model description

Governing equations

The temporal and spatial dynamics of the wave field were investigated using the freely available SWAN model. A description of the SWAN model is contained in Booij *et al.* (1999), Ris *et al.* (1999) and Holthuijsen (2007). Waves can be characterised by their frequency and the direction from which they propagate; the so called the directional wave spectrum (Hauser *et al.* , 2005). The energy (E) contained at a particular frequency and direction is called the energy density. SWAN is a third generation spectral wave model that solves the spectral energy balance Equation whereby the wave spectrum is characterised by a number of discreet frequencies (Δf) and directions ($\Delta\theta$) (Holthuijsen, 2007). SWAN uses an implicit numerical scheme to allow for shallow water depths and give greater numerical stability. The spectral energy balance equation is:

$$\frac{\partial}{\partial t}E + \frac{\partial}{\partial x}c_x E + \frac{\partial}{\partial y}c_y E + \frac{\partial}{\partial \theta}c_\theta E = S \tag{2.1}$$

where $E(f, \theta; x, y, t)$ is the energy density as a function of frequency f and direction θ, referenced to the coordinate system whereby x is orthogonal to y, and t is time. The first term of the equation represents the local rate of change of the energy density in time. The second and third terms relate to the propagation of the energy density in space with propagation velocities given by c_x and c_y; where c is defined as:

$$c = \sqrt{\frac{g}{k} tanh(kd)} \tag{2.2}$$

where g is the acceleration due to gravity (9.8 ms^{-2}), k is the wave number and d is the water depth. The fourth term of the equation represents the effects of depth-induced refraction. There has been no attempt to incorporate the effect of time varying water depths (tides) or currents (tidal and wind driven). It is possible that in shallow near-shore regions and Thorny Passage (Figure 2.1), such tidal effects may cause significant errors within the model, but throughout the majority of the model domain, these tidal effects will be negligible. In equation 2.1, S represents the source terms that account for generation (wind), dissipation (white capping, bottom-friction and depth-induced breaking) and non-linear wave-wave interactions (triads and quadruplets).

The bulk wave parameters are denoted and defined:

$$H_s = 4\sqrt{\int_0^\infty E(f)df} \tag{2.3}$$

$$H_{swell} = 4\sqrt{\int_0^{0.1} E(f)df} \tag{2.4}$$

Computational grids and configurations

Four grids using spherical coordinates were used in this study (Figure 2.1). A coarse resolution grid, referred to as the South Australian Regional Wave Model (SARWM), spans the central South Australian coastline and includes Spencer Gulf, Gulf St. Vincent and Kangaroo Island within its domain. This

coarse resolution grid cannot adequately resolve south-west Spencer Gulf due to the complex coastlines and variable bathymetry. The nesting capability in SWAN has been utilised and within the coarse resolution model, two finer grids are nested. The first is a fine-resolution grid covering the Tuna Farming Zone, referred to as the Tuna Wave Model (TunaWM). A second fine-resolution grid covering the Adelaide metropolitan coastline (MetroWM) was also incorporated into the coarse resolution grid, which was required to adequately resolve the bathymetry in the vicinity of M10. A very high resolution grid, referred to as HRWM, is nested within the MetroMW grid. The HRWM grid has been included to provide insight into the fine-scale wave induced orbital velocities in the near-shore region of the Adelaide metropolitan coastline (not shown). Specific details of the grids used in this study are outlined in Table 2.3.

Table 2.3: The computational grids used in the wave model.

Configuration	SARWM	TunaWM	MetroWM	HRWM
Latitude (S)	32.16-36.38	34.46-34.84	35.17-35.67	34.80-35.04
Longitude (E)	135.54-138.70	135.79-136.21	138.25-138.57	138.44-138.52
Coordinate Sys.	Spherical	Spherical	Spherical	Spherical
$\Delta x = \Delta y$ (degrees)	0.02	0.0036	0.0055	0.00090
$\Delta\theta$	10	10	10	10

Boundary conditions

Bathymetry

The bathymetry used in this study was derived from a number of datasets. The bathymetry used in the SARWM grid is a subset from the Geoscience Australia (GA) Bathytopo 0.01° product. The bathymetry for the TunaWM

and MetroWM domains again originate from GA but this time using the 250 m resolution product. The HRWM bathymetry was extracted from a very high resolution swath mapped dataset recently acquired by the Coast Protection Branch of the South Australia Department for Environment and Heritage. This product was used to include the effects of nearshore fine-scale features on the wave regime.

Coastlines

At all land boundaries, it is assumed that all the wave energy is dissipated in near-shore processes such as depth-induced breaking. SWAN allows for reflective boundary conditions, but there has been no attempt to incorporate such processes in this application. Observational data from the southern side of Thistle Island (M8) showed no swell reflection in the directional spectra.

Open Sea Boundaries

The southern and western open-sea boundary of the SARWM domain was forced by the Meso-WAM output obtained from the Australian Bureau of Meteorology (BOM). The two dimensional (frequency and direction) wave spectrum obtained from Meso-WAM at Cape du Couedic was used to force both the southern and western open-sea boundaries. The modelled directional spectrum was read into the model every three hours. The open-sea boundaries of the fine resolution grids were forced with output obtained from SARWM.

Surface Forcing

Wind forcing data were taken from a high resolution version of the Limited Area Prediction System(LAPS), which is often referred to as Meso-LAPS, also obtained from BOM. Meso-LAPS gives a spatially varying wind

field with a 12.5 km resolution. The wind field is tri-linearly interpolated in space and time onto the model grid. Meso-LAPS wind fields have a temporal resolution of 1 hour.

2.3 Results

2.3.1 Model assessment

Several datasets were used to asses the performance of the SARWM, TunaWM, MetroWM and HRWM model configurations. A heuristic sensitivity analysis of the wave model was performed with respect to the choice of physics scheme used. The bulk wave statistic of H_s was then assessed using a combination of *in situ* and satellite-derived data. The non-directional wave spectra was assessed using the *in situ* data from M7, M8 and M10. Finally, a coherence analysis between the observed *in situ* and modelled H_s provided insight into how well the model captured events on time scales ranging from hourly through to synoptic periods.

Sensitivity analysis

Model runs, using the different physics schemes, were performed to compare the modelled wave spectra with the observed wave spectra at M7 in the tuna farming zone (Figures 2.4 and 2.5). The KOMEN and JANSSEN schemes significantly over-predicted the amount of wave energy in the wind-wave band of the 1-D energy density spectrum by approximately 25% and 20% respectively. The WESTHUYSEN scheme, with a whitecapping coefficient, $C_{wc} = 1.75 \times 10^{-5}$, gave the best estimate of the wave energy, and was therefore the physics scheme of choice for this study.

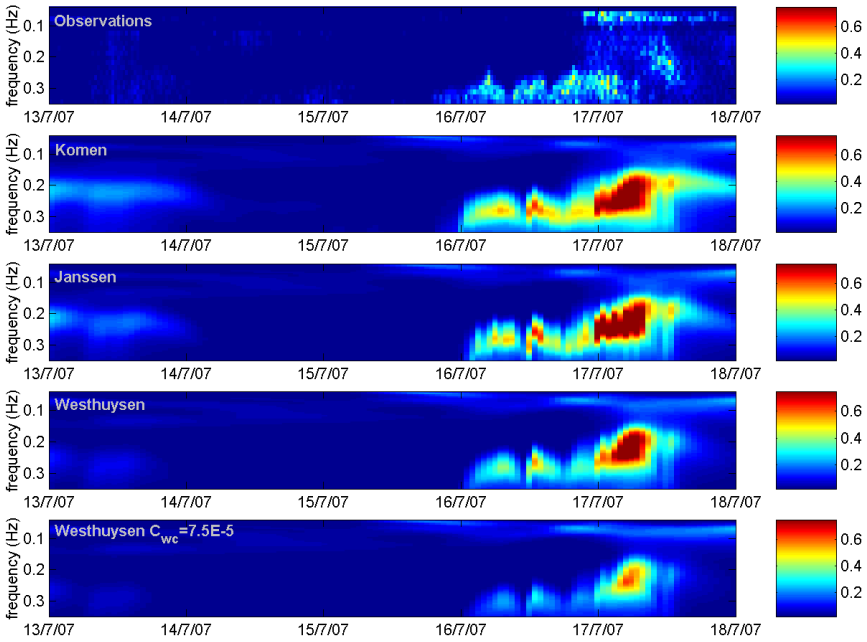

Figure 2.4: A time series plot of the 1-D spectrum at M7. The top panel contains the observational data from M7, the subsequent panels are the modelled spectra from TunaWM using different physics schemes. The bottom panel contains the spectrum from the tuned model where the whitecapping dissipation coefficient, $C_{wc} = 1.75 \times 10^{-5}$. The colour scale denotes the amount of energy E (m^2/Hz) contained at the relevant frequency at a point in time.

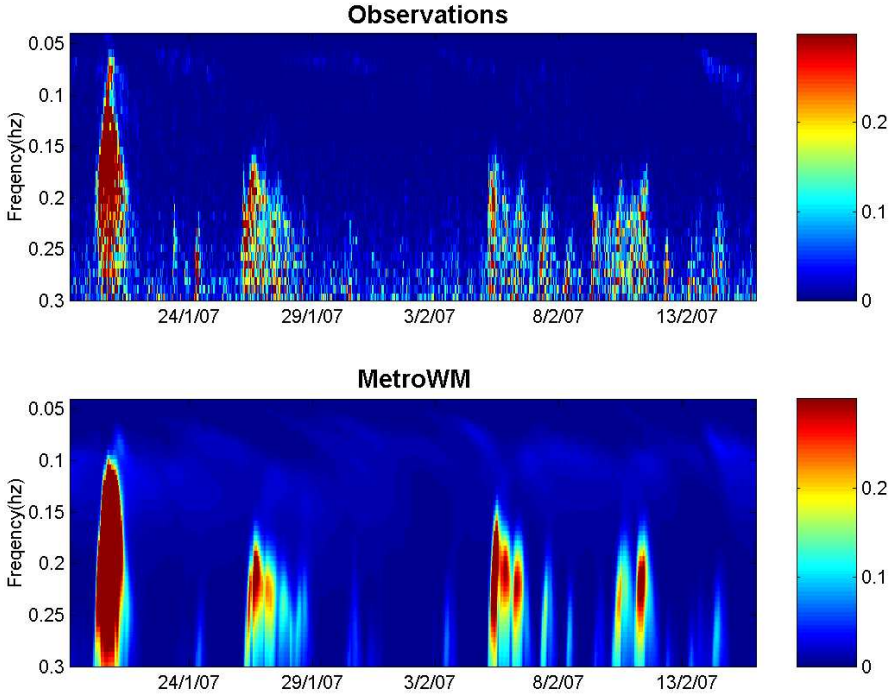

Figure 2.5: A comparison between the observed (top) and modelled (lower) energy density spectra using the WESTHUYSEN scheme at mooring M10 located 2 km offshore of Grange Jetty in Adelaide metropolitan waters. The colour scale denotes the amount of energy E (m^2/Hz) contained at the relevant frequency at a point in time.

In situ assessment

A comparison between modelled and *in situ* observed H_s time-series (Figures 2.6 and 2.7) show good agreement at all observational locations throughout the domain. Our discussion of the model performance begins at M9, the most exposed site and moves into the more sheltered gulf sites.

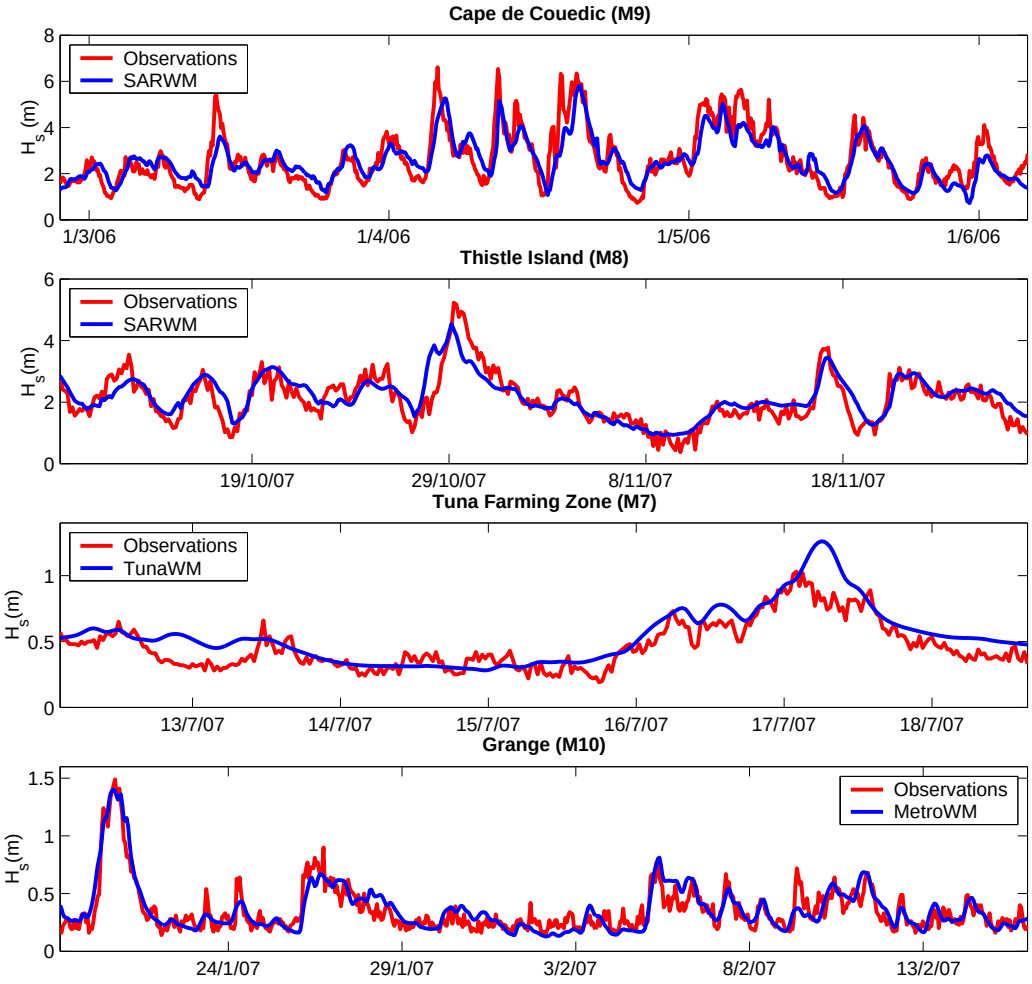

Figure 2.6: A time series comparison between the observed (red) and modelled (blue) H_s at location: M9, M8, M7 and M10.

At M9 there is a slight bias in the model to under-predict the significant

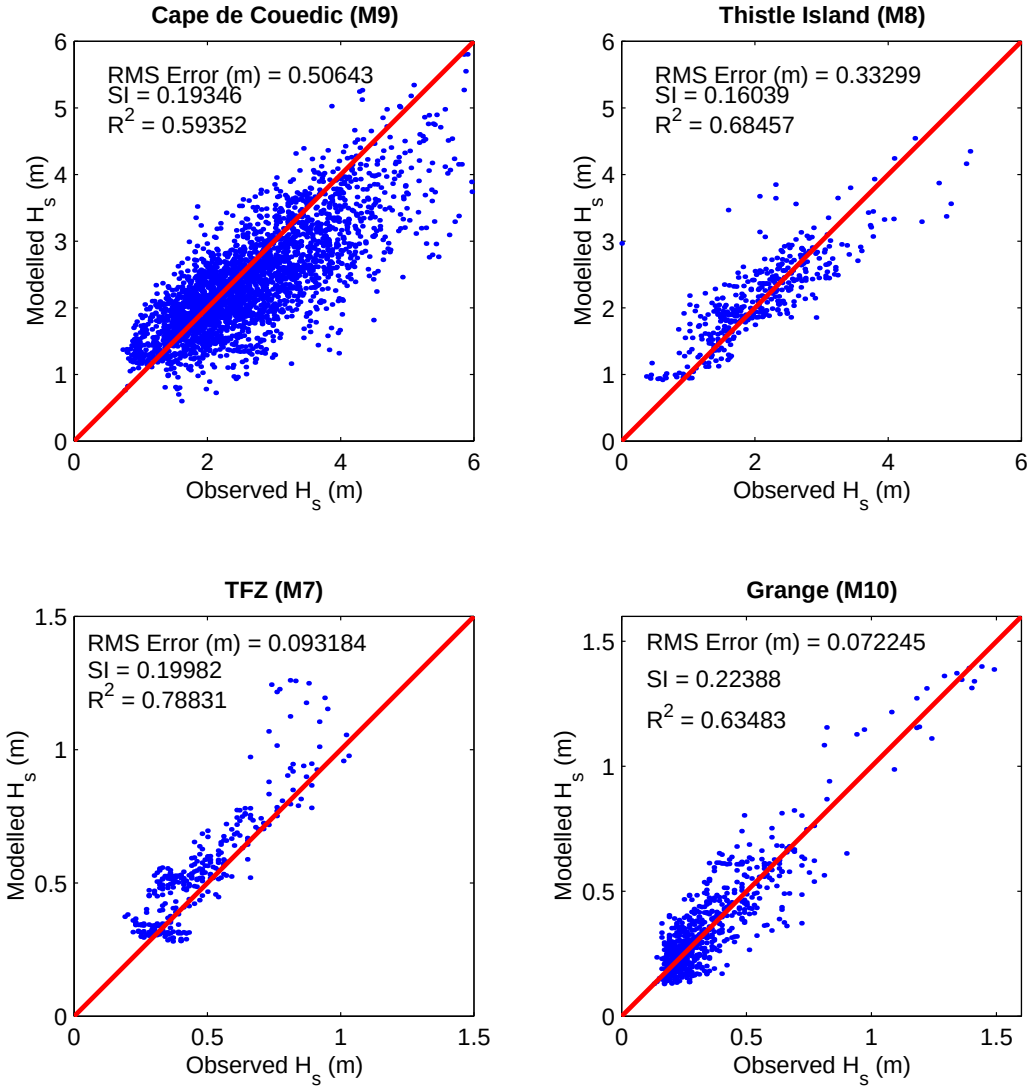

Figure 2.7: A scatter plot between the observed and modelled H_s at location: M9, M8, M7 and M10. The root mean square (RMS) error, Scatter Index (SI) and correlation coefficient (R^2) give an indication of model performance at that location.

wave height by up to 15% during high energy events. During times of low wave heights, the model has a tendency to over-predict H_s by up to 20%. This slight disparity between the model and observations influenced the model performance in areas dominated by oceanic swell conditions.

A comparison of the modelled and observed H_s from M8 near Thistle Island (Figure 2.6), also shows good agreement. On some occasions, during peak events such as on 29/10/07, the model under-predicted H_s by approximately 10% and there was a slight phase difference between the time of the peak event predicted by the model and observations. Such an occurrence is likely to be attributed to MesoWAM incorrectly predicting the arrival of this swell event. The underestimation of the maximum H_s was due to the bias in the MesoWAM forcing data. The high frequency variations seen in the observed H_s were not reproduced by the model (see below).

When mooring M7 was deployed, it was hoped that it would record a storm event. While not capturing a severe storm event, a moderately energetic event did occur on 17/07/2007 (Figure 2.6). Once again, although the model did not reproduce the higher frequency variability seen in the observations, it did capture most of the observed signal. When the modelled wave heights were compared to the observed wave heights, there was very good agreement, except during the peak of the storm, where the modelled wave heights were over-predicted by 20%. Nonetheless, overall there was a good agreement between the observed and modelled wave heights.

A comparison between the observed wave spectrum and modelled wave spectrum (Figure 2.4) clearly shows the reason for the over estimation of H_s during the peak wave event on the 17/7/07. The observed spectrum is

dominated by wind waves during the start of this event, beginning early on the 16/7/07. There appeared to be episodic generation of higher frequency wind waves. Late on the 16/7/07, swell began to appear. Until this stage, TunaWM was performing well and captured the main features displayed by the observational record. Early on the 17/7/07, the observational record showed a decrease in the energy between the ranges 0.15 and 0.3 Hz for a period of 3-4 h, at which point lower-frequency waves (0.1-0.25 Hz) appeared. It was this that TunaWM did not capture; instead it predicted a peak in mid-frequency energy, which resulting in the peak in H_s shown in Figure 2.6. The predicted peak in mid-frequency energy is likely to be due to inconsistencies in the modelled wind field. Slight directional differences between the modelled winds and the actual wind field by only a few degrees can radically alter the fetch from 10 km to over 200 km.

The observational data obtained from M10, sited in 7 m of water offshore from Adelaide gave a high quality dataset in an area spatially removed from M7. There was excellent agreement between the observed and modelled H_s at this location. The peak events were captured well by the model in both magnitude and timing. The excellent performance of the model at this site, far removed from the other *in situ* observations, provides extra confidence in the model results.

Satellite assessment

A spatial assessment of SARWM was undertaken using data obtained from the altimeter sensor onboard the ENVISAT satellite from the European Space Agency. When the modelled H_s was compared with the satellite-derived H_s.

The negative bias associated with the MesoWAM forcing data can be seen particularly as the observed wave heights increased, and was associated with the observations to the south and west of Kangaroo Island (Figure 2.8).

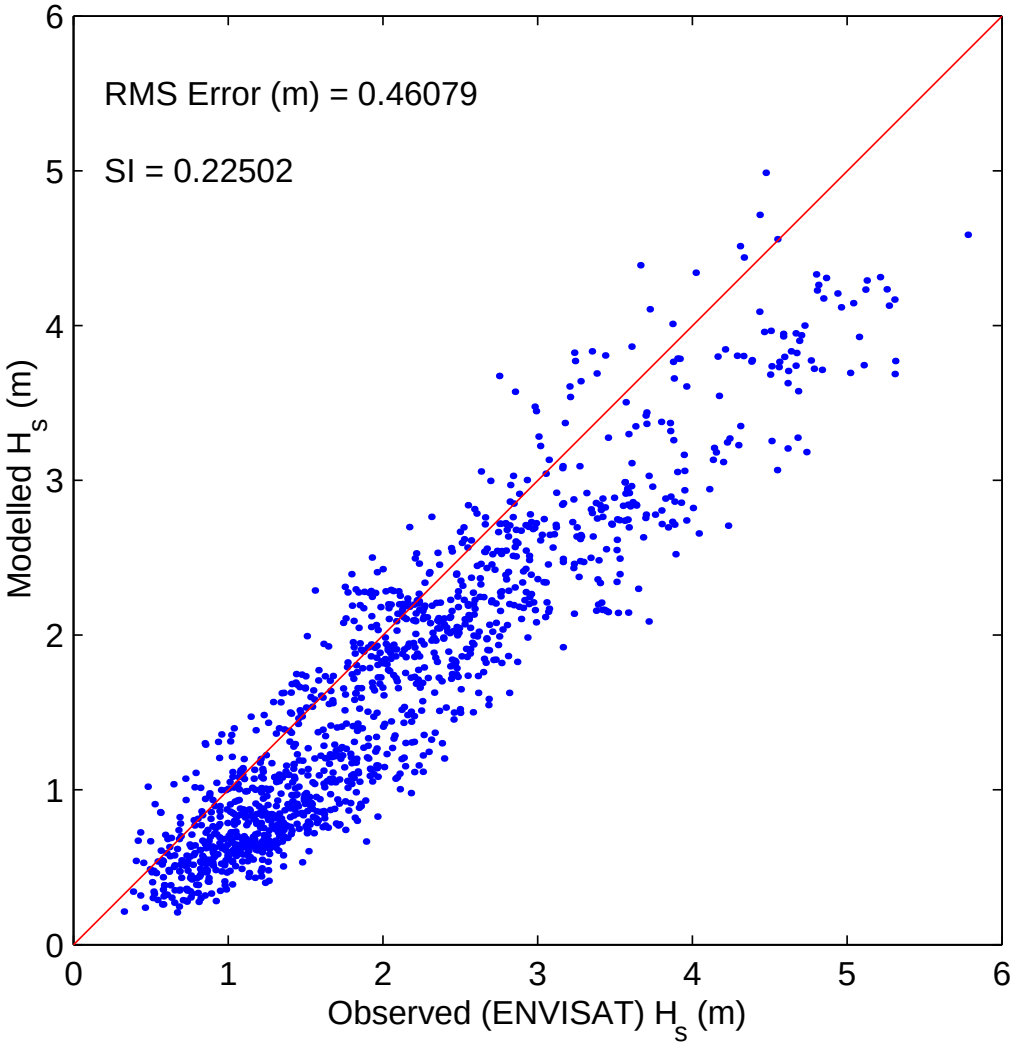

Figure 2.8: A scatter plot of observed and modelled H_s from the ENVISAT altimeter.

Coherence analysis

The results from the coherence analysis yields insight into the magnitude and phase difference between two signals in frequency space. The coherence between the the modelled and observed *in situ* H_s displayed good agreement in both magnitude (Figure 2.9a) and phase (Figure 2.9b) at periods greater than 0.5 days. This indicates that the energy associated with synoptic scale events is propagated into the model. However, the higher frequency events that may be due to any local effects, such as sea-breezes, are not captured by the forcing data.

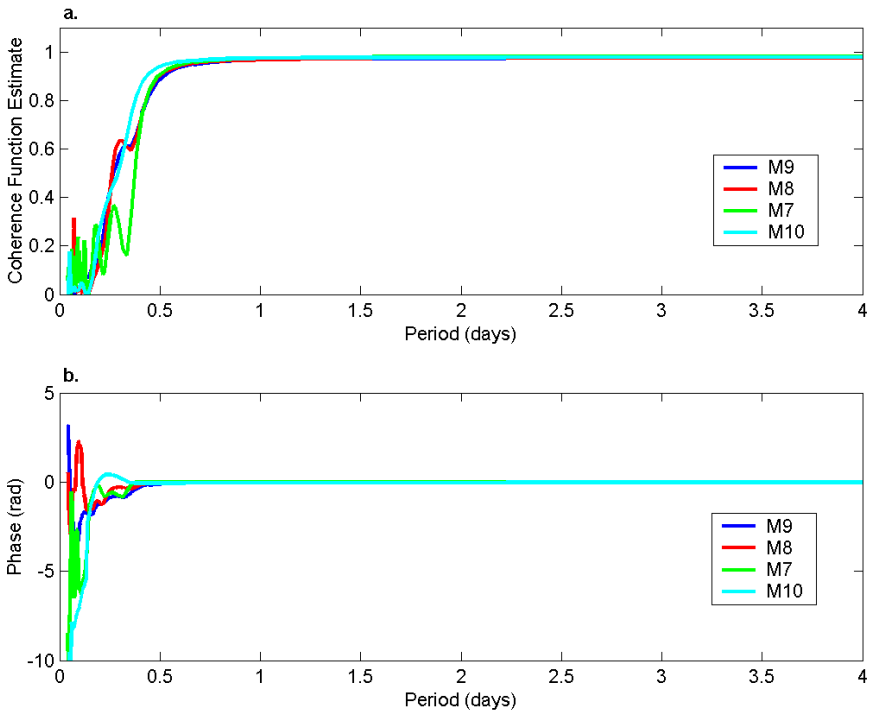

Figure 2.9: Results of the coherence analysis between the observed and modelled H_s at the mooring location M7, M8, M9 and M10. The coherence function gives (a) an estimate of the magnitude squared correlation between the observed and modelled H_s signals and (b) the phase difference between the observed and modelled H_s signal.

2.3.2 Model hindcasts

During the recorded high energy event of 17/7/07, the observed H_s at M7 in the middle of the tuna farming zone peaked at 1.0 m and the modelled wave height reached 1.28 m (Figure 2.6c). This event is representative of many of the energetic events that occur on a synoptic timescale throughout the year. Using the wave model to hindcast a two year period between the 1/9/05 and the 1/9/07, it was possible to find the maximum wave heights achieved during this period (Figure 2.10).

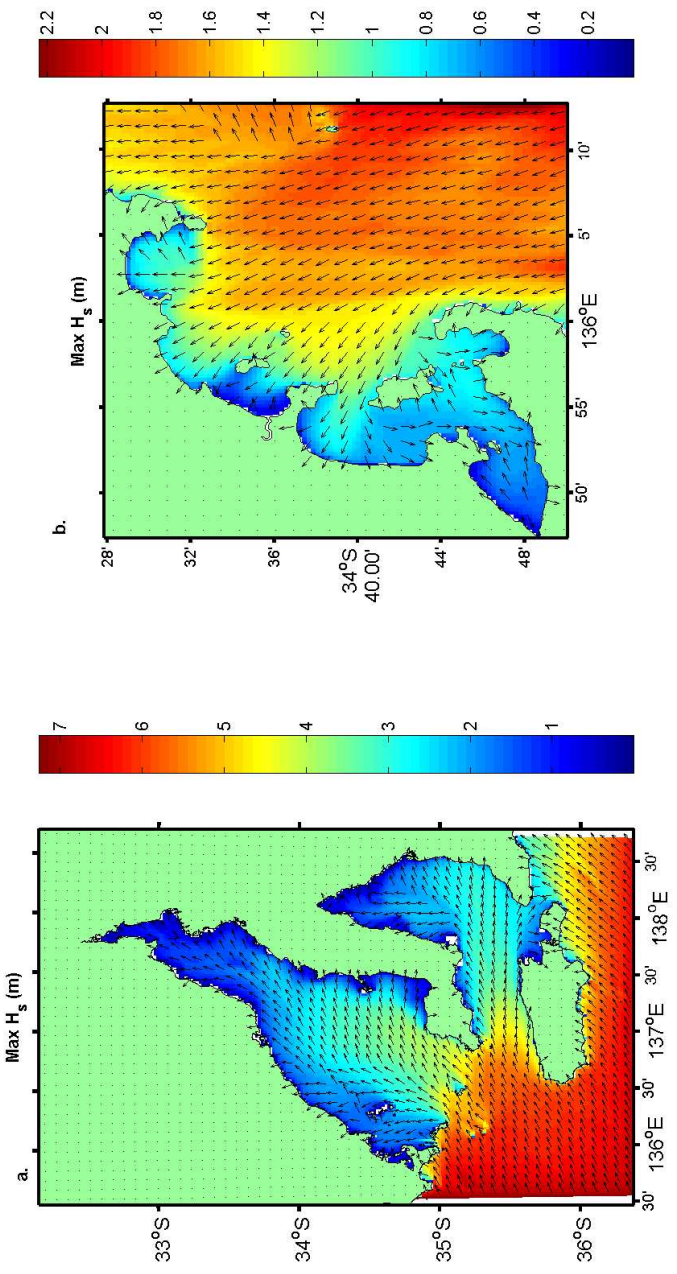

Figure 2.10: Modelled maximum H_s (m) and direction (°N) for (a) SARWM and (b) TunaWM domains, for the two year period between the 1/9/05 and the 1/9/07. The arrows indicate the direction in which the waves are travelling.

The wave heights within Spencer Gulf ranged from 2 m in the north, through to over 4 m in the more exposed southern section of the Gulf (Figure 2.10a). Although, Gulf St. Vincent is more sheltered, the lower western region was still subject to a H_s of between 3 and 4 m. In the region of the tuna farming zone, the spatial variation in the modelled maximum wave height fields (Figure 2.10b) show that the sheltered areas west and south of Boston Island had a maximum H_s of up to 0.8 m, whereas the exposed areas to the east of Cape Donnington ranged between 1.5 and 2 m. The offshore wave direction was from the south, but in areas protected from the incident swell, the waves were closely aligned with the wind direction. The central tuna farming zone, in the vicinity of M7, had a maximum H_s of between 1.5 and 1.7 m, which is 50% higher than the recorded event of the 17/7/07.

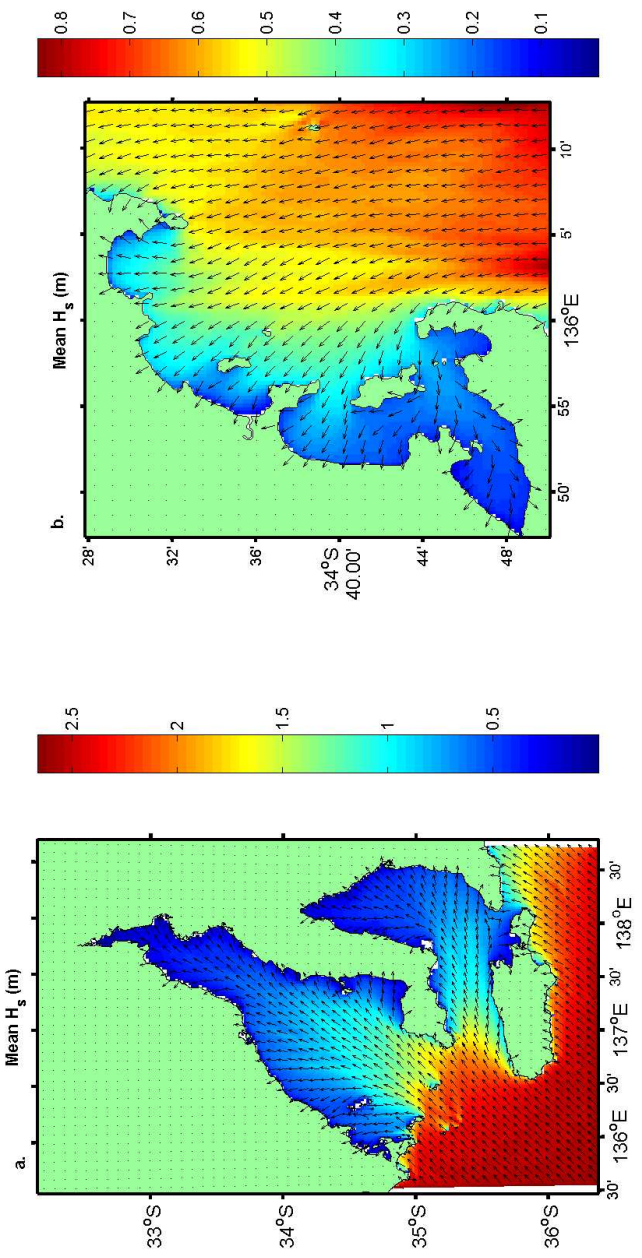

Figure 2.11: The modelled 2 year mean H_s (m) and wave direction (°N) for (a) SARWM and (b) TunaWM domains for the period between the 1/9/05 and the 1/9/07.

The annual mean H_s in the region, varied from 0.1 m in the sheltered coastal embayments, to 2.5 m in the more exposed offshore regions (Figure 2.11). The incoming wave direction was generally from the south, refracted by the bottom topography into the more sheltered regions. The wave height diminished rapidly as the depth decreased, due to the interaction of the waves with the bottom resulting in dissipation of wave energy. The mean wave heights in Spencer Gulf were greater than those of the shallower and more protected Gulf St. Vincent. This can be explained by the attenuation of low frequency waves by bottom friction. In the tuna farming zone (Figure 2.11b) the region to the east of Cape Donnington is the most energetic, with an annual mean H_s of 0.8 m near-shore. For most of the tuna farming zone the annual mean H_s is between 0.3 and 0.6 m.

The main source of wave energy, apparent in the annual mean, is the propagation of waves into the tuna farming zone from the south. This is supported by the mean wave direction coming from the south (see Figure 2.11). The incident wave energy is a combination of swell energy that propagates through Thorny Passage and swell that is refracted by the bottom topography into the tuna farming zone from between Thistle Island and Yorke Peninsula. The source of this wave energy is dependent upon the period of the waves. For waves with a period greater than 6-7 seconds (swell and longer period wind waves) the Southern Ocean is the dominant source, as these longer period waves cannot be generated within Spencer Gulf. However, waves with periods of less than 6 seconds are generated by the local wind field within the model domain. There appears to be a concentration of wave energy near the shoreline to the west of Bollingbroke Point (Figure

2.11.b and 2.11.b). Once again it is likely that this is due to the refraction effects caused by the bathymetry.

2.4 Discussion

The prevalent wave conditions within the tuna farming zone are a combination of locally generated wind waves and incoming swell from the Southern Ocean. The effects of locally generated wind waves are often masked by the influence of the incoming swell from the Southern Ocean, except in the sheltered areas to the west of Boston Island. To investigate the role of wind waves, an idealised experiment using only homogeneous wind forcing across the model domain was used to identify the wind direction capable of generating the greatest H_s at the mooring location M7 (Figure 2.12). A idealised experiment was also undertaken to investigate the swell direction that is capable of producing the greatest swell height in the tuna farming zone (Figure 2.13).

Within the tuna farming zone, the wave height associated with wind waves is highly sensitive to the wind direction and strength. Winds from the north through east to the south generate the greatest wave heights. This is directly related to the fetch available for these wind directions. There is a linear response to an increase in wind speed between 7 ms^{-1} and 15 ms^{-1}, but as previously stated, the wind direction does cause significant variation at higher wind speeds. Winds from the east through to south cause the greatest wind wave heights in the middle of the tuna farming zone at M7.

As oceanic swells encounter the progressively shallower waters of the continental shelf, bottom friction dissipates the energy. Accordingly, the swell height at M7, in the tuna farming zone, is very sensitive to the angle at which the oceanic swell approaches the shelf. Swell propagating into the re-

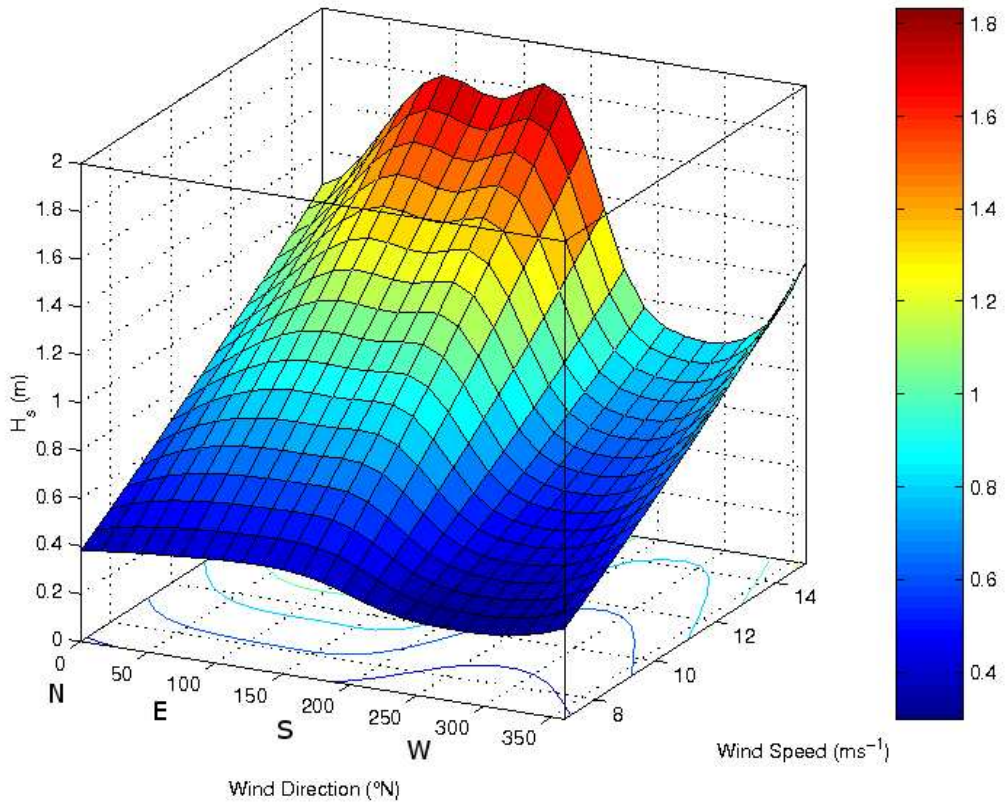

Figure 2.12: The results of an idealised wind experiment investigating the H_s at M7 using a homogeneous wind field and varying the wind speed and direction. The 3-D surface plot highlights the relationship between the wind speed, wind direction and H_s.

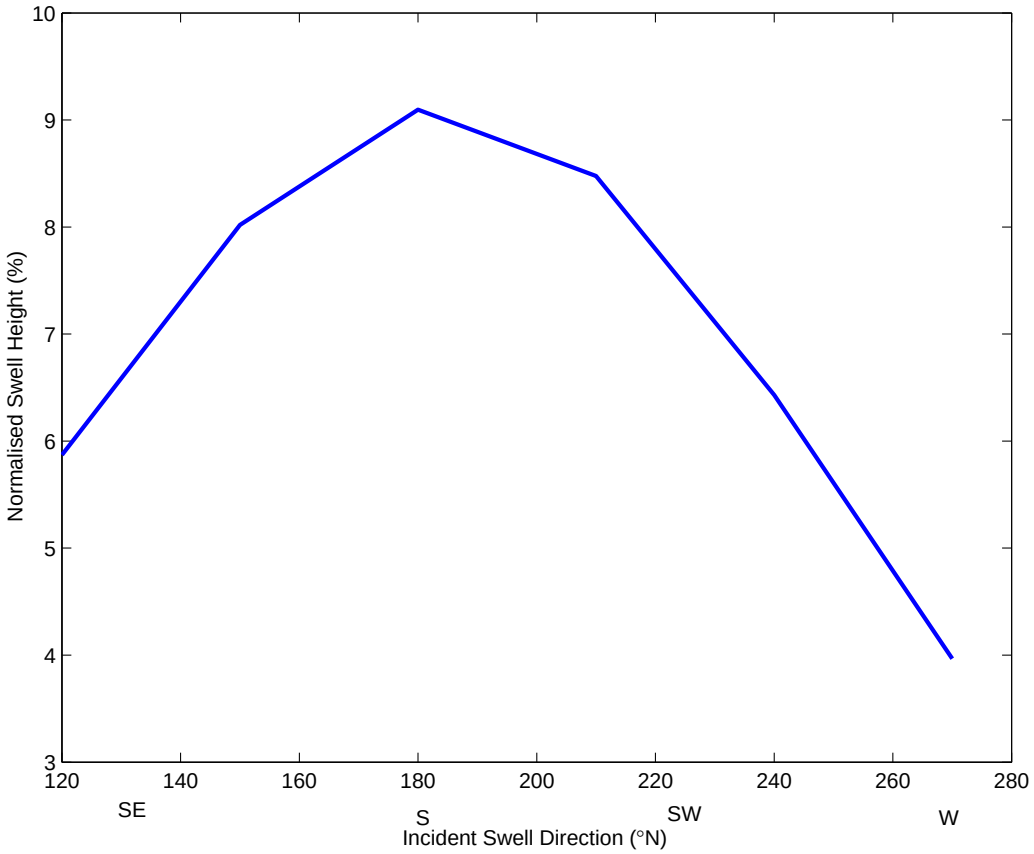

Figure 2.13: The results of a idealised swell experiment investigating the relationship between the incident swell direction at the southern boundary of the SARWM domain and swell height at M7 in the tuna farming zone.

gion from directly south (180 $^{\circ}N$) requires the least refraction and results in swell heights of approximately 9% of the value at Cape de Couedic, on the south-western tip of Kangaroo Island. Swell entering the region from $>$ 180 $^{\circ}N$ progressively decreases in height as little energy is able to be refracted in the tuna farming zone. Swell entering the region from $<$ 180 $^{\circ}N$ is blocked by Kangaroo Island and only small amount of refracted energy enters the tuna farming zone. To investigate the main source of wave energy within the tuna farming zone, the energy ratio (ER) between the swell height (H_{swell}) and the significant wave height (H_s) was used (eq. 2.5)

$$ER = \frac{H_{swell}}{H_s} \tag{2.5}$$

The ER at M7 was calculated for the period 1/9/05 - 1/9/07 and the mean value was 0.37 with a standard deviation of 0.16. This mean ER value indicates that 37% of the wave energy present in the tuna farming zone is contained within the swell band of the wave spectrum. Swell waves propagate into the tuna farming zone from the Southern Ocean and cannot be generated within the model domain by any wind forcing. This result shows that the wave energy derived from wind forcing is slightly larger than the energy propagating into the region from the Southern Ocean.

The ER was then calculated for each grid point in both the SARWM and TunaWM domains (Figure 2.14). The southern regions of Spencer Gulf and south-western Gulf St. Vincent are largely dominated by swell, with values for the ER ranging from 0.6-0.8. This result is to be expected due to the influence of the Southern Ocean. The ER progressively decreases until in

the upper regions of Spencer Gulf it drops below a value of 0.05. The tuna farming zone experiences a mixed range of ER values. There are numerous sheltered coastal embayments where the mean ER is less than 0.05. However, in the central region of the tuna farming zone, there is evidence that swell energy is of similar level to that of the local wind forcing. This area, which extends all the way up to the west of Point Bollingbroke and through to Louth Bay, has exhibited significant amounts of coastal erosion in recent years (Depart of Environment and Heritage, personal communication). This suggests that longer period waves are present and pose an increased risk of swell-induced sediment resuspension.

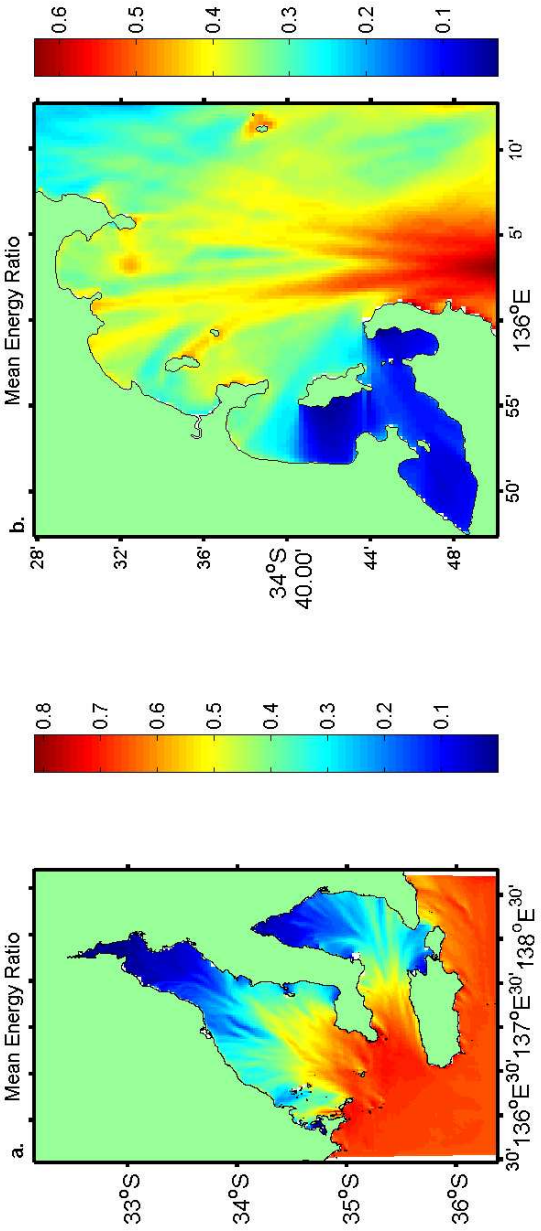

Figure 2.14: Mean Energy Ratio (ER) for (a) SARWM and (b) TunaWM domains for the period between the 1/9/05 and the 1/9/07.

The mean directional energy spectrum at M7, in the tuna farming zone, and M9, west of Kangaroo Island, was calculated for the two year period of the model run (Figure 2.15). At the more exposed site of M9 the mean period of the swell is 12 seconds and it propagates from a bearing of 225° N. This contrasts with the results at M7 in the more sheltered tuna farming zone where the effects of refraction are pronounced; the peak in the swell band of the spectrum now propagates from 175° N. In addition, swell energy entering the region from this direction needs to pass through Thorny Passage. However, effects of diffraction have not been accounted for in the present study, which if included may reduce the magnitude of this peak. Of particular interest is a second smaller peak that occurs at the same frequency, but propagating from 140°-150° N. This peak is due to swell being refracted into the tuna farming zone from the southern entrance of Spencer Gulf, between Thistle Island and Yorke Peninsula. The higher frequency waves, which are locally generated, are closely aligned to the wind direction associated with various synoptic weather conditions which dominate this area. The most obvious are the wind waves that propagate from a south-easterly direction. This synoptic condition is a typical summer time phenomena and is responsible for the observed upwelling that occurs on the adjacent continental shelf (McClatchie *et al.* , 2006; Middleton & Platov, 2003).

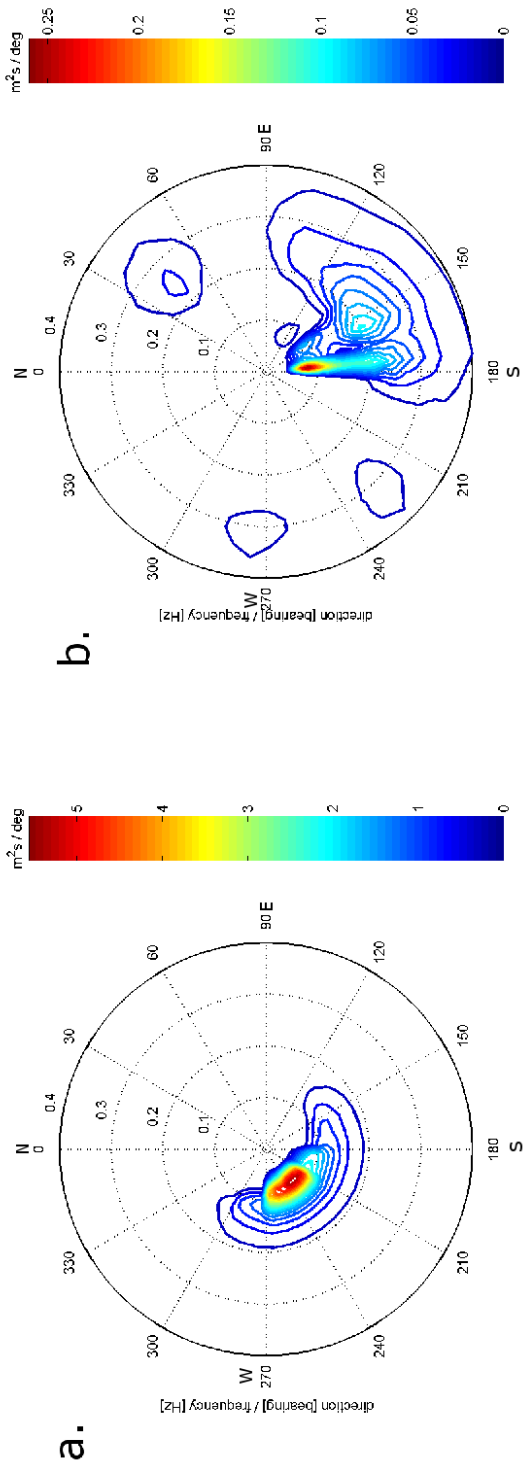

Figure 2.15: The mean directional wave spectrum for (a) M9, Cape du Couedic and (b) M7, tuna farming zone, between 1/9/2005 and the 1/9/2007.

The output from this wave model has been used along with a hydrodynamic model for the forcing of a coupled sediment-biogeochemical model used to study the nutrient cycling in tuna farming zone (Tanner & Volkman, 2009). Furthermore, we have tuned this model to accept readily available Bureau of Meteorology forecast products that could be used as boundary conditions to turn this model into an high resolution operational wave forecasting model, the application of which could be used to predict sediment resuspension events in an area of high economic importance.

A more rigorous examination of model error could be obtained through generating an ensemble of model runs, forced with ensemble winds taken from the new experimental Australian Community Climate and Earth-Systems Simulator (ACCESS), and open-ocean boundary conditions extracted from the developmental Australian Wavewatch 3 (WW3) model. These two forcing streams (ACCESS and WW3) are currently not available as operational products, however as they enter the public domain, it will be possible to quantitatively evaluate the model error in SARWM and TunaWM, that arises from the forcing data.

2.5 Conclusions

In this study the SWAN wave model has been applied using the WEST-HUYSEN saturation-based whitecapping scheme. A comparison with field data highlights the superior performance of this scheme when compared to the other available schemes, which further supports its use in other coastal applications. The modelling of wave heights and directions in the tuna farming zone is an important tool for predicting physical conditions prevalent in this area, and is crucial for a better understanding of the parameters driving sediment resuspension, water quality and interactions with the sediment biogeochemistry. The wave modelling can be summarised as follows:

- The three wave-model grids used in this study have been assessed against four *in situ* and one remotely sensed dataset spanning all the model domains. There is good agreement between observed and modelled wave characteristics throughout the region of Spencer Gulf and Gulf St. Vincent. The normalised RMSE error was less than 10% at all mooring locations.

- Due to the presence of swell and wind-sea, the newly available saturation based whitecapping scheme gives far better model performance in this study region. This is due to the whitecapping dissipation term no longer being proportional to the mean spectral steepness.

- There are sheltered regions to the north and west of Louth Island and in the embayments of Boston Bay and Proper Bay. These areas are largely affected by locally generated wind waves, with an annual mean

H_s of less than 0.3 m. The regions to the south of Bollingbroke Point and east of Cape Donnington are far more exposed, with an annual mean H_s of 0.5-0.8 m.

- Winds coming from the north-east through to south-east generate the most wind-wave energy in the tuna farming zone.

- Swell propagating into the region from directly south causes the greatest swell heights within the tuna farming zone.

- From the results of the wave modelling study, the relative influence of energy propagating into SW Spencer Gulf is comparable to that of the wind forcing, except in sheltered coastal embayments. Of the mean wave energy present at M7, 80% originates from 175°N, 15% from SE (120°N to 170°N) wind seas and 5% from other directions.

The wave model presented in this Chapter when combined with readily available forecasts from the Bureau of Meteorology, can be used to predict wave conditions in the tuna farming zone and throughout the central South Australian coastline. The ability to forecast severe wave events has direct economic applications to many coastal and offshore industries.

Chapter 3

Wave-sediment interactions

3.1 Introduction

The SW corner of Spencer Gulf in South Australia supports a large aquaculture industry deriving most of its value from the farming of southern bluefin tuna. Approximately 5,000 tonnes of this species are fattened over autumn and winter in the 172 km^2 of the tuna farming zone (TFZ). The Gulf has the shape of an inverted 'V' with a length of approximately 300 km and a width of 110 km at its southern end (Figure 3.1). It behaves as an inverse estuary (Nunes & Lennon, 1986), with flushing by shelf waters restricted to the austral winter, and a seasonal density front forming during summer, limiting gulf-shelf exchange (Petrusevics, 1993).

Before the TFZ was relocated to its current position, a sediment resuspension event in 1996 severely impacted upon the regional aquaculture industry by causing up to 75% mortality in some tuna pens. High concentrations of fine sediments were found in the gills of the tuna fatalities, suggesting that

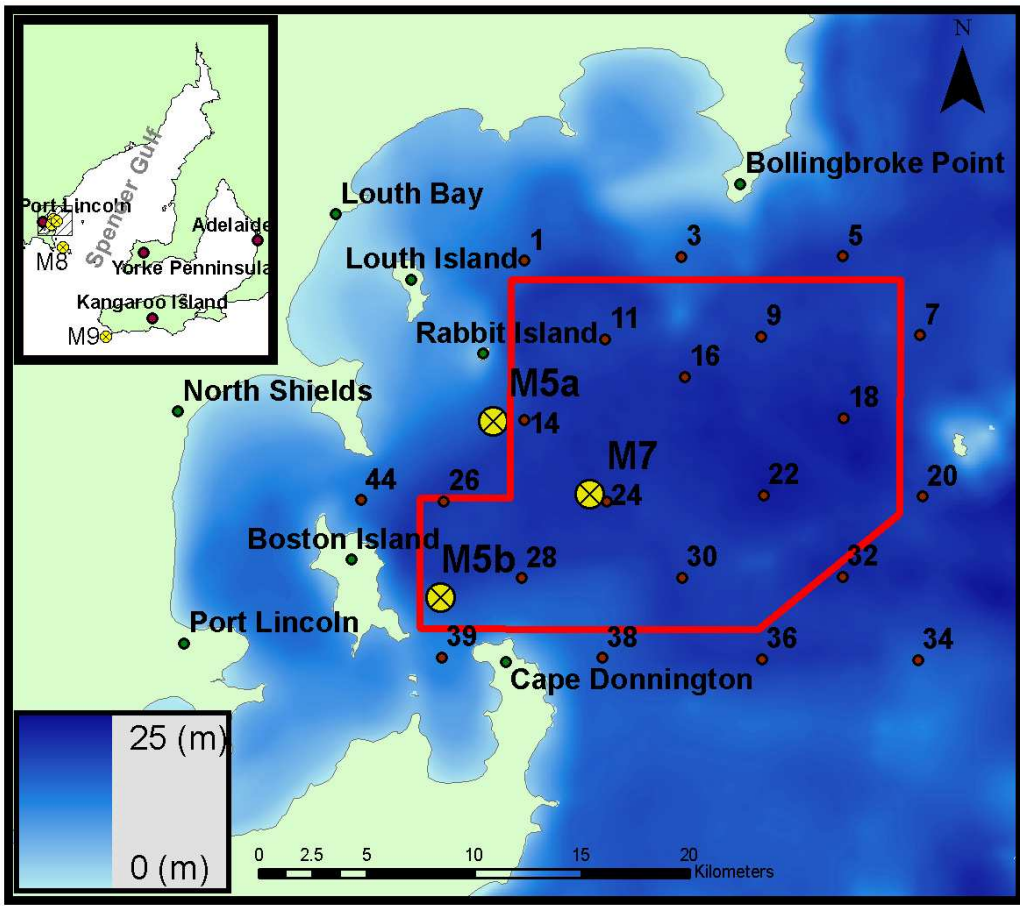

Figure 3.1: Map of study region showing sampling locations (red points) and mooring locations (yellow points), water depth (m) and the extent of the fine-scale model domain (main) and the coarse-resolution model domain (inset). The Tuna Farming Zone (TFZ) is indicated by the red boundary.

the resuspension of fine sediments played a key role in this mortality event (Clarke, 1996). Resuspension events have also been shown to increase the concentration of nutrients in the water column (Lawrence *et al.* , 2004). Under commercial tuna pens, the concentrations of ammonium and phosphate in sediment porewaters are significantly higher than values at control sites located at least 1 km from any tuna lease (Lauer, 2005). When resuspended, these sediments are likely to add nutrients to the water column, potentially fuelling phytoplankton blooms, and/or toxic responses in the fish.

As southern Spencer Gulf is a micro-tidal system (< 2 m range) (Harris, 1994), near-bottom currents in the region of the TFZ rarely exceed 0.1 m s^{-1} (Herzfeld *et al.* , 2009). However, tidal currents across the mouth of the gulf are relatively strong, often reaching 0.5 m s^{-1}. Previous studies using coarse resolution tidal and wave models suggest that sand transport in Spencer Gulf is dominated by tidal currents rather than storm induced transport, with the latter dominating the adjacent shelf region (Porter-Smith *et al.* , 2004).

The physical mechanisms behind wave and current induced sediment resuspension and transport are associated with an increase in the bed-shear stress in the bottom boundary layer (Guillen *et al.* , 2002). Previous studies into the swell and wave characteristics of Spencer Gulf have found that little or no swell is present in the upper (wave heights typically < 5 cm) and central regions of the Gulf (wave periods typically < 6.5 s) (Noye, 1984). In the southern section of Spencer Gulf, the wave field is a combination of locally generated wind waves and incoming swell from the Southern Ocean (Chapter 2). In a previous wave modeling study of this area, Hemer & Bye (1999) only used the incident swell to force their model, limiting their analy-

sis to the transformation of oceanic swell across the shelf into coastal zones. Another wave model applied to Gulf St. Vincent, to the east of our study area, indicated that fine (¡ 0.063 mm) and medium-grained (0.063 mm - 0.25 mm) sands in the near-shore region are mobilised by wave-induced currents for between 50% and 90% of the time (Pattiaratchi *et al.* , 2007). When tidal currents were included, this increased to 70-90% of the time.

The most common parameter used to assess sediment resuspension in the field is Suspended Particulate Matter (SPM) concentration, measured either directly or indirectly. Direct methods involve the collection of water samples whereby SPM is measured gravimetrically after filtration. Indirect methods use a turbidity sensor calibrated against direct SPM measurements. Although the indirect method has the advantage of producing a continuous datastream, it requires validation from field measurements. Indirect measurements of SPM usually rely on Optical Backscatter Sensors (OBS), light transmissometers or Echo Intensity (EI) acoustic measurements.

OBS instruments emit light at a particular wave length and a sensors then measures the intensity of the reflected light from SPM, which is then converted into a turbidity measurement (Hamblin *et al.* , 2000). During long deployments in the photic zone, OBS measurements are highly susceptible to marine fouling unless a cleaning mechanism is installed on the sensor (You, 2005). Many studies have used OBS measurements to investigate the link between tidal currents, wave action, or a combination of both, to the SPM concentration in the water column (Paphitis & Collins, 2005; Tragou *et al.* , 2005).

The use of acoustic devices such as Acoustic Doppler Current Profilers

(ADCP's) provides information on EI throughout the entire profile of the water column. As the concentration of particles in the water column increases so too does the EI. To quantitatively measure SPM using EI, a calibration dataset of direct measurements must be taken. If direct measurements of SPM are not available to calibrate the EI, the technique can still be used to qualitatively identify periods of elevated SPM (Klein, 2003). Acoustic measurements assume that particles in the water column are moving at the same rate as the ambient current. However, if there are small particles in the water column (such as zooplankton) that move independently of the ambient current, then the velocity measurements can be biased (Smyth *et al.* , 2006), as can measurements of the SPM.

In this study, the grainsize characteristics of the sediments were investigated together with the wave regime leading to resuspension episodes, in the region east of Boston Island, encompassing the TFZ, in lower SW Spencer Gulf. The primary objectives were to determine:

- the spatial distribution of sediment types, expanding on the previous work of Fernandes *et al.* (2006), to include a much larger area with a higher density of sampling stations,
- the relationship between the modelled wave regime and the observed distribution of sediment characteristics and
- the shear stresses generated by surface gravity waves and the critical shear stress thresholds necessary for sediment resuspension.

3.2 Methods

Symbols and abbreviations used in this Chapter are shown in Table 3.1.

Table 3.1: List of symbols and abbreviations used in Chapter 3.

Symbol	Description	Value	Units
OBS	Optical Backscatter Sensors	-	-
SPM	Suspended Particulate Matter	-	g m^{-3}
EI	Echo Intensity	-	dB
H_{swell}	Swell Height	-	m
H_s	Significant Wave Height	-	m
T_p	Peak Wave Period	-	s
T_m	Mean Wave Period	-	s
T_d	Peak Period Wave Direction	-	$^\circ N$
c	Wave Phase Speed	-	m s^{-1}
E	Energy Density	-	m^2 Hz^{-1})
τ_w	Wave Induced Shear Stress	-	N m^{-2}
τ_c	Critical Shear Stress	-	N m^{-2}
ρ	Density of sea water	1024	kg m^{-3}
f_w	Wave Friction Factor	-	-
U_b	Bottom Orbital Velocity	-	m s^{-1}
U_{sig}	Significant Orbital Velocity	-	m s^{-1}
S^*	Sediment-Fluid Parameter	-	-
ν	Kinematic viscosity	1.6x10^{-6}	m^2 s^{-1}
ψ_c	Critical Shields Parameter	-	-
k	Wave number	-	m^{-1}
d	Depth	-	m
g	Gravity	9.8	m s^{-2}
p_d	Sediment Particle Diameter	-	μm
s	Sediment Particle Density	2.65	g cm^{-3}

3.2.1 Mooring data

Three moorings were deployed in four locations in SW Spencer Gulf and on the adjacent shelf (Figure 3.1; Table 3.2). The moorings were equipped with an ADCP capable of measuring currents and waves (Figures 3.2 and 3.3).

Moorings M5 and M7 also collected salinity and turbidity data.

Figure 3.2: Moorings used for the collection of temperature, salinity, pressure, turbidity and currents at locations M5a and M5b (Source: CSIRO).

3.2.2 Wave model description

The temporal and spatial dynamics of the wave field were investigated using the freely available SWAN model. SWAN is a third generation spectral wave model that characterises wave spectra by a number of discreet frequencies and directions (Booij *et al.* , 1999; Ris *et al.* , 1999). Two grids were used in this study. A fine grid (TunaWM) with a resolution of 0.4 km covering the TFZ is nested within a coarser grid (SARWM) with a resolution of 2 km

Figure 3.3: The mooring frame used to mount the RDI Workhorse (300kHz) ADCP in deployments M7 and M8.

Table 3.2: The location of the moorings used in the study.

	M5a	M5b	M7	M8
Latitude (S)	-34.635	-34.708	-34.666	-34.992
Longitude (E)	135.988	135.967	136.033	136.099
Depth (m)	21	19	22	44

covering the Gulfs of South Australia (Figure 3.1). The open-sea boundary of SARWM was forced with the output from the regional MesoWAM wave model obtained from the Bureau of Meteorology (BOM). The surface wind fields were forced with BOM MesoLAPS wind fields. The open boundary of the fine-scale model was forced with data obtained from the coarse-scale model. The comparison of modelled significant wave height and observed significant wave height at five locations showed good agreement. A detailed discussion of the wave model is presented in Chapter 2 of this thesis.

3.2.3 Wave analysis

Wave-induced orbital velocities generate a shear force that the sediments experience. This study exclusively focused on the wave-induced bed-shear stress, τ_w, which is related to the maximum orbital velocity, U_b, according to:

$$\tau_w = 0.5\rho f_w U_b^2 \tag{3.1}$$

where ρ is the density and f_w is the wave friction factor (Fredsoe & Deigaard, 1992; Nielsen, 1992b). Linear wave theory relates significant wave height (H_s) and mean wave period (T_m) to U_b according to:

$$U_b = \frac{\pi H_s}{T_m \sinh(kd)} \tag{3.2}$$

where d is the water depth and k is the wave number. k is approximated using the method of Fenton & McKee (1990):

$$k \approx \frac{4\pi^2}{gT_m^2}\left(\coth\left(\frac{2\pi}{T_m}\sqrt{\frac{d}{g}}\right)^{\frac{3}{2}}\right)^{\frac{2}{3}} \tag{3.3}$$

where g is the acceleration due to gravity.

The values of U_b were obtained from the output of SWAN in 1 h intervals for the austral winter (June - August 2006) at each of the stations used in the sediment survey of mineral grain size (see Figure 3.1 and Section 3.2.4). Winter was chosen for the simulation period as this is the time of year when strong SW swells are generated (see Chapter 2). The mean of the highest third of U_b at each station was used to calculate a parameter called the 'significant orbital speed', which is analogous to the concept of significant wave height (e.g. the average height of the highest third of waves within a record) (Holthuijsen, 2007):

The significant orbital speed is denoted and defined:

$$U_{sig} = \frac{3}{N}\sum_{j=1}^{\frac{N}{3}} U_b^{(j)} \tag{3.4}$$

Where U_b has been resequenced in monotonically descending order so that $U_b^{(1)}$ is the highest speed, $U_b^{(2)}$ the next highest and so on.

A hierarchical-cluster analysis using the Euclidean distance between points, was used to identify areas with significantly different wave characteristics. The parameter U_{sig}^2 was used in the cluster analysis, as τ_w is proportional to U_b^2. A Kruskal-Wallace non-parametric one-way ANOVA (Hollander, 1973), was performed to test whether there was a statistically significant difference between the sediment characteristics found in the wave groups identified in

the cluster analysis.

3.2.4 Sediments

Core collection

Sediment cores were collected at each of the 21 stations for mineral grain size analysis (Figure 3.1). Two replicate cores were collected using a ship-deployed HAPS Corer (KC Denmark). Cores were 6.7 cm in diameter and 10-15 cm in length. Upon retrieval, the overlying water in the tube was carefully discarded to minimise surface disturbance and the sediment extruded onto a clean stainless steel table. The top 1 cm was then transferred into pre-combusted alfoil trays, and stored on ice before transfer to the laboratory and long-term storage at -20°C.

Grainsize analysis

The analysis method is detailed in Fernandes *et al.* (2006), whereby clay was analysed with a hydrometer and larger grainsizes were separated using a series of stacked sieves of 2000, 1000, 500, 250, 125 and 63 μm mesh sizes. Silt was calculated as the difference between the total weight of sediment, and the sum of the clay and sand fractions. Each grainsize was then presented as a percentage of the total weight. The statistics of particle size distributions (mean grain size, sorting, skewness and kurtosis) were calculated using the Folk and Ward method within the GRADISTAT software developed by Blott & Pye (2001). This method was chosen to analyse the data as it is relatively insensitive to large variations in the tails of the sediment distribution.

3.2.5 Theoretical approach to calculating the initiation of sediment movement

Sediment mobility under the combined effects of waves and currents has long been of interest in engineering problems. Many theories have developed dimensionless measures to identify when the initiation of sediment motion takes place. One of the most commonly used parameters is the Shields parameter, in which the balance between disturbing and stabilising forces is taken into account (Nielsen, 1992b). The critical Shields parameter (ψ_c) used in this study was estimated from empirical data, using the sediment-fluid parameter S^* (Nielsen, 1992b):

$$S^* = \frac{p_d}{4\nu}\sqrt{(s-1)gp_d} \tag{3.5}$$

Where $s = 2.65$ for sand, g is the acceleration due to gravity, p_d is particle diameter, and ν is the kinematic viscosity ($1.6 \times 10^{-6}\mathrm{m}^2 s^{-1}$). ψ_c is then related to S^* using the following relationship:

$$\psi_c = \begin{cases} 0.1{S^*}^{\frac{2}{7}} & : \quad S^* < 0.8 \\ 0.06 & : \quad S^* > 300 \end{cases} \tag{3.6}$$

For $0.8 > S^* > 300$, ψ_c can be found using the modified Shields diagram (Figure 3.4). In this work, typical values for ψ_c ranged between 0.050 and 0.055. The critical Shields parameter is related to the critical shear stress (τ_c) by the following equation:

$$\tau_c = \rho(s-1)gp_d\psi_c \tag{3.7}$$

Where ρ is the density of the fluid, $s = 2.65$ for sand, g is the acceleration due to gravity, and p_d is the particle diameter. In this study, we only consider the shear stress due to waves in the bottom boundary layer and make no attempt to include the effect of ambient currents.

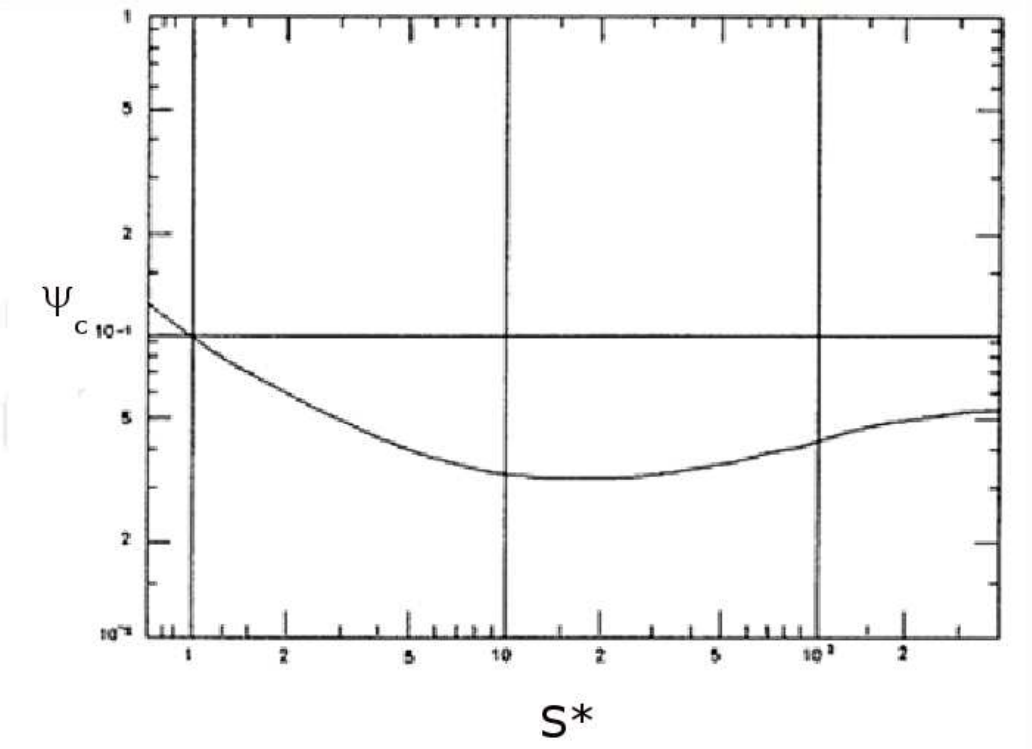

Figure 3.4: Modified Shields Diagram (adapted from Nielsen (1992b))

3.3 Results

3.3.1 Spatial variation in observed sediment characteristics

The sediments within SW Spencer Gulf can be classified as a mixture of very fine to fine sands (mean diameter 50-250 μm). The silt:clay ratio is approximately 2 or greater for the majority of the region. Regions of fine sediments are located to the north of Cape Donnington and east of Boston Island, which join a band of fine sediments from east of Louth Island extending in a south-easterly direction for 35 km (Figure 3.5). There are regions of coarse-grained sediments south of Louth Island and to the SW of Rabbit Island, to the east of Cape Donnington and also south of Bollingbroke Point.

3.3.2 Wave-sediment grain size interactions

The modelled values of U_{sig} range from 0.01 m s^{-1} at the sheltered station 39 to 0.11 m s^{-1} at the more exposed station 36 (Figure 3.6). During storm events U_b can reach up to twice U_{sig}, peaking between 0.20 m s^{-1} and 0.22 m s^{-1} at exposed locations. A comparison between the modelled U_{sig} and the bathymetry shows a vague relationship between depth and U_{sig}, with areas of shallow water depth experiencing high values of U_{sig}. Besides depth, other parameters such as exposure to fetch, shoaling, and wave refraction will combine to create a complex set of non-linear interactions responsible for the spatial distribution of the U_{sig} observed.

The results of a cluster analysis based only on U_{sig} identified two major

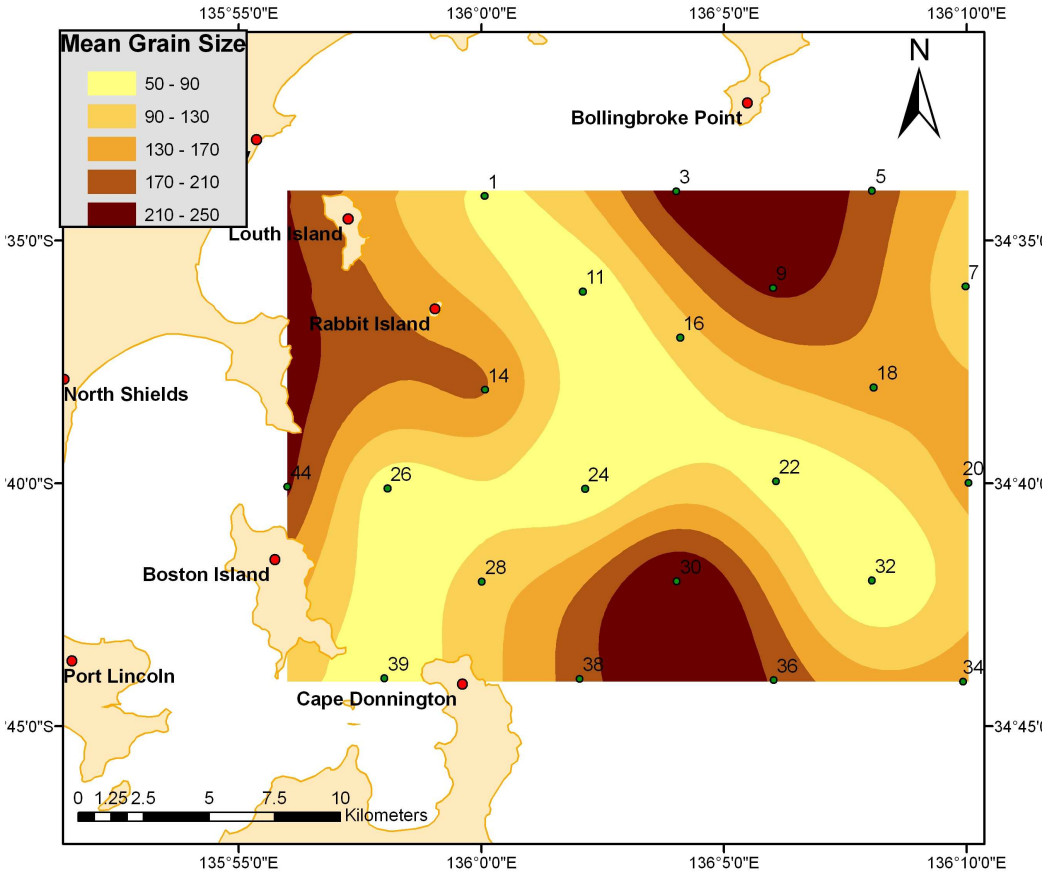

Figure 3.5: Spatial distribution of sediment mean grain size (in μm).

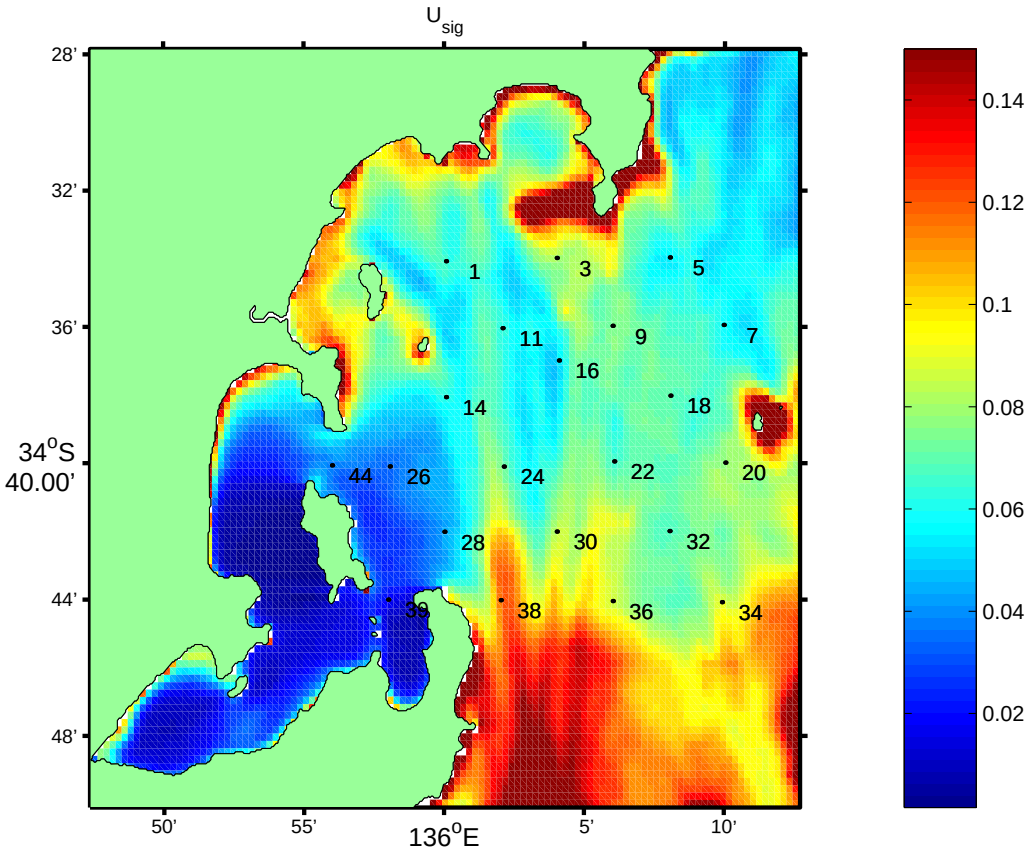

Figure 3.6: A map of U_{sig} (in m s^{-1}) for the period 1/9/05 - 1/9/07.

groupings (Figures 3.7 and 3.8). Stations forming Wave Group 1 were less energetic with $U_{sig} < 0.070$ m s^{-1}, whereas those from Wave Group 2 had $U_{sig} > 0.074$ m s^{-1} (Figure 3.9). To test the relationship between U_{sig} and the observed sediment characteristics, a Kruskal-Wallis test was performed to identify any significant differences between the 2 wave groups (Table 3.3). The test was performed using the values at the actual stations not from the interpolated data.

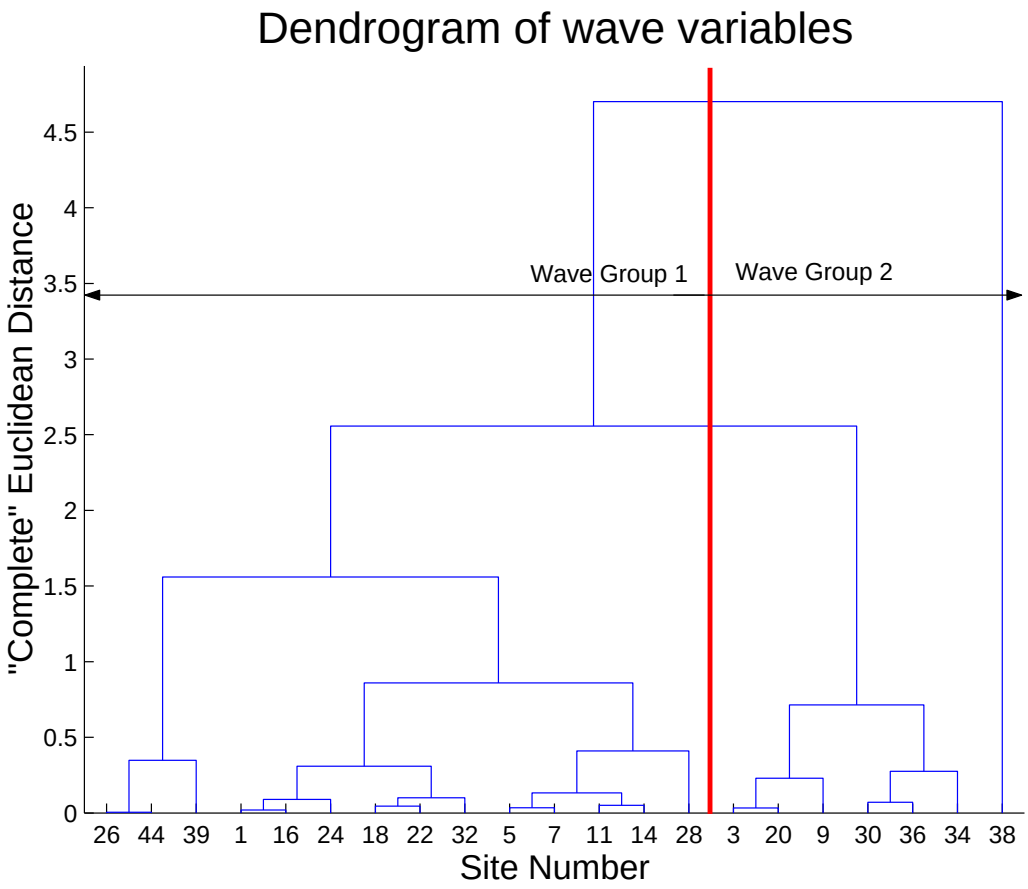

Figure 3.7: The results of a hierarchical cluster analysis of U_{sig}. Linkages show the 'Complete' Euclidean distance between the sites used in the sediment survey.

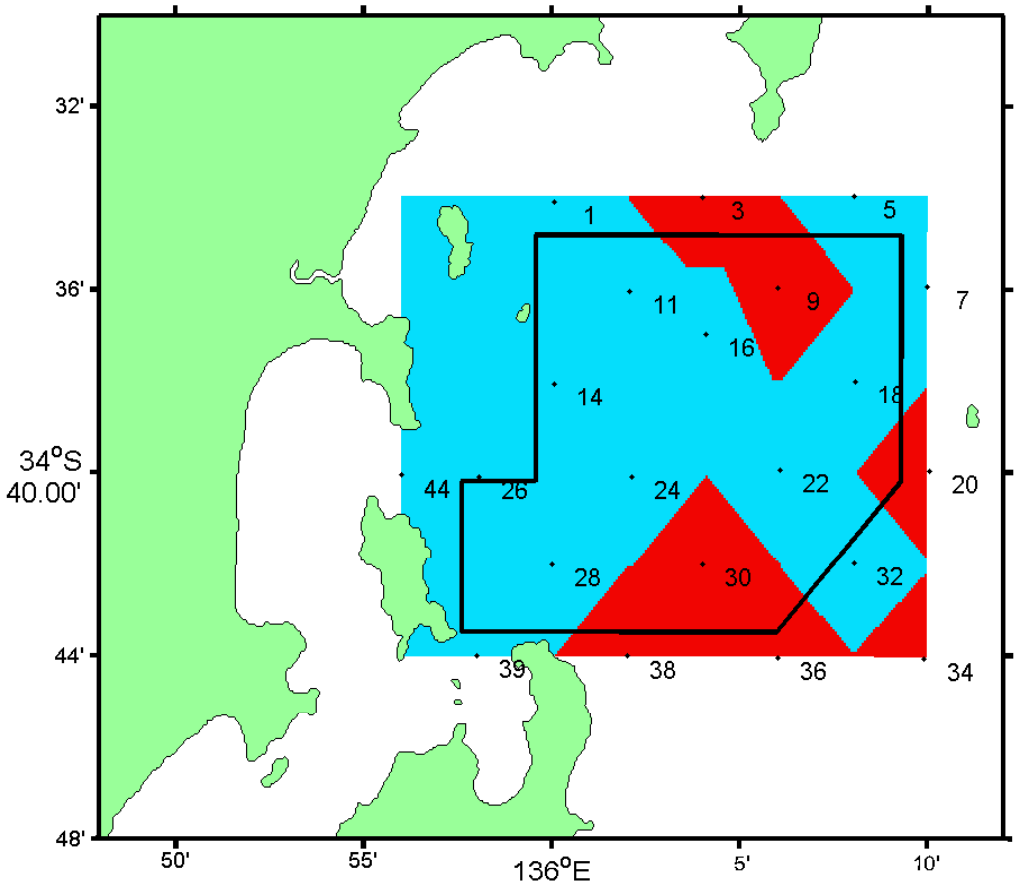

Figure 3.8: Results of cluster analysis colour coded by (cyan) Wave Group 1 and (red) Wave Group 2. The black boundary delineates the approximate position of the tuna farming zone.

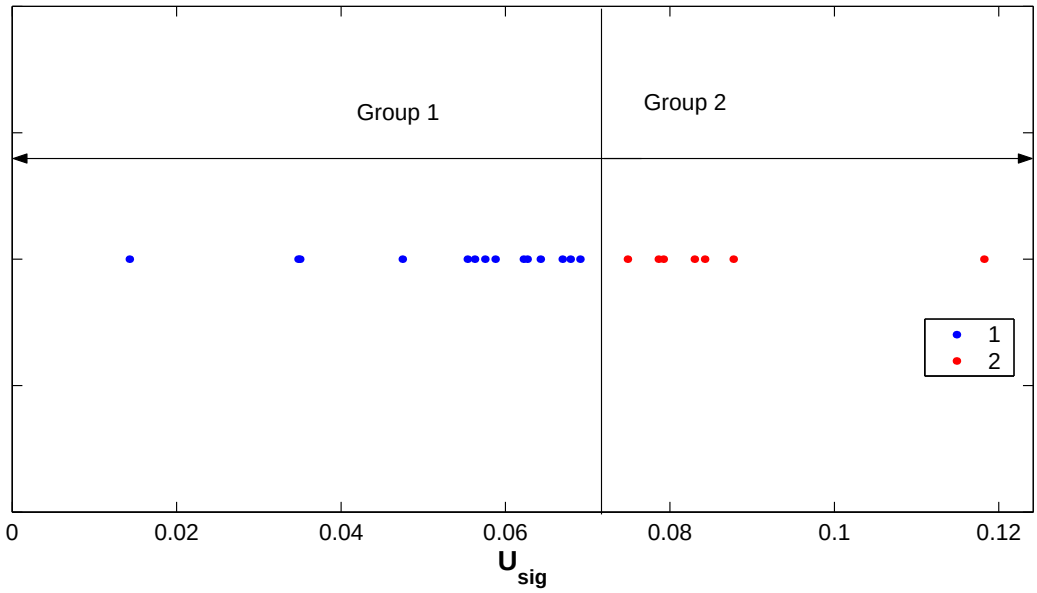

Figure 3.9: A one dimension plot of U_{sig} highlighting the delineation between Wave Group 1 (blue) and wave group 2 (red).

With the exception of station 44, the mean grainsize in Wave Group 1 was less than 200 μm. Station 44 lies within the channel at the northern entrance of Boston Bay, which is subject to significant tidal flows (Grzechnik, 2000), therefore fine sediments may be eroded due to high current speeds as opposed to wave action. In Wave Group 1 areas, sediments consisted of 43% fine material (63 - 125 μm), in contrast to Wave Group 2 areas, which contained $<$ 18% of this size fraction. This suggests that the finer-grained sediments are winnowed-out where U_{sig} exceeds 0.074 m s^{-1}. With the exception of station 36, the mean grain size in Wave Group 2 stations was greater than 240 μm.

Table 3.3: The results of a Kruskal-Wallis non-parametric analysis of the main wave groups (WG) identified by the cluster analysis of U_{sig}. Variables with a statistically significant difference between the groups are highlighted in bold.

	WG 1(n=14)	WG 2(n=7)	p-value
Wave Variables			
U_{sig}(m s^{-1})	0.054	0.084	**0.0005**
Grain Size Variables			
Mean Grain Size (μm)	138.6	259.4	**0.0112**
Clay($<$ 5 μm)(%)	5.5	5.7	0.4118
Silt(5-63 μm)(%)	17.6	9.7	0.0734
V. F. Sand(63-125 μm)(%)	19.7	11.2	**0.0013**
F. Sand(125-250 μm)(%)	25.8	26.6	0.2963
M. Sand(250-500 μm)(%)	18.4	21.0	0.6015
C. Sand(500-1000 μm)(%)	8.1	10.3	0.2326
V. C. Sand (1000-2000 μm)(%)	2.8	6.0	**0.0036**
Granule (>2000 μm)(%)	1.9	9.3	**0.0090**

3.3.3 Observed sediment resuspension

Sediment resuspension in coastal waters can be difficult to measure. Traditional optical sensors are highly susceptible to marine fouling. In this study a number of these sensors were mounted on various moorings (M5, M7), but the signal recorded showed significant amounts of contamination due to bio-fouling. An alternative to optical sensors is the use of echo intensity (EI) obtained from acoustic instruments. Moorings M5, M7 and M8 were all equipped with an ADCP capable of measuring EI, and was used as a qualitative tool for signalling an increase of SPM concentrations in the water column.

The mooring M5a was located in a relatively sheltered environment to the south of Rabbit Island where $U_{sig} < 0.070$ m s^{-1} (Figure 3.6). The EI time series extracted from M5a describes a complex signal (Figure 3.10).

Periods when high EI extends throughout the water column coincide with the hours of darkness and are likely to be migrating zooplankton that feed at night. This signal is especially evident between the 1/9/05 and the 10/9/05. However, wave events occurring on the 2/9/05, 11/9/05 and the 8/10/05, led to the wave-induced shear stress (τ_w) peaking at over 0.1 N m^{-2}, and were also accompanied by an increase in the EI throughout the water column, particularly evident in the lower 5 - 10 m of the water column.

To investigate the signal close to the seafloor at 18.5 m, we removed the effects of the diel vertical migrators by calculating the 24 hour moving average of EI (Figure 3.10b). More sophisticated low-pass and band-pass filters were trialled (not shown) in an attempt to remove the biological signal, however the 24 hr moving average gave the most consistent result. This approach removed the signal associated with the zooplankton, so that any increase in signal intensity was not likely to be biological in nature. Figure 3.10b clearly indicates that wave events generating a $\tau_w > 0.1$ N m^{-2}, always led to sediment resuspension in the region of M5a. The resuspension appears to be largely confined to the bottom 10 m of the water column (Figure 3.10a). However, Figure 3.10b also suggests that the EI signal is not always explained by τ_w alone. It is likely that the elevated EI signal during late September - early October is a result of a phytoplankton and/or zooplankton bloom. Unfortunately there is no field data to corroborate this. Mooring M5a sampled for waves every 8 h. This resolution is too coarse for a detailed insight into the physical conditions that may generate a resuspension event.

Mooring M7 was set to continuously sample at 2 Hz for almost a week, resulting in a more detailed picture of a resuspension event than mooring M5.

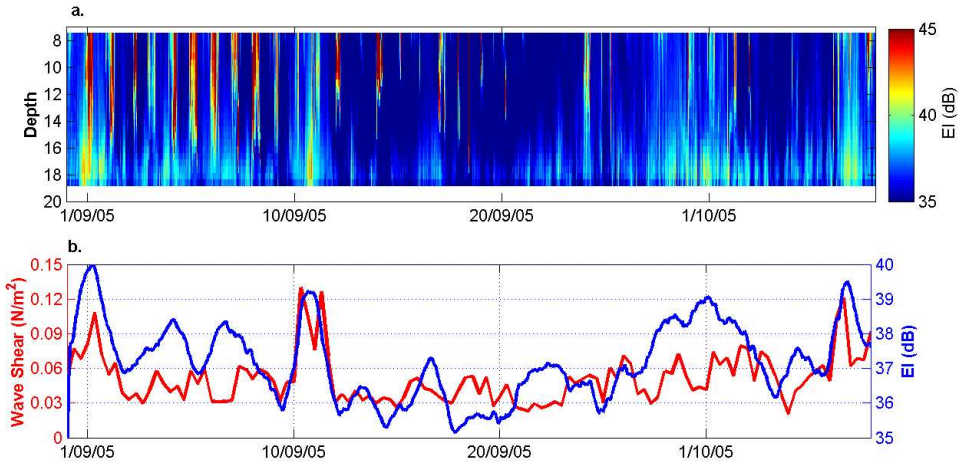

Figure 3.10: Data from mooring M5a displaying (a) the distribution of EI throughout the water column and (b) the τ_w (red) and 24 hr moving average of EI (blue) at 18.5 m.

Data obtained from mooring M7 again showed the diel vertical migration of zooplankton, with a strong signal at night (Figure 3.11a). To filter this biological signal, a 24 h moving average was applied to the EI signal close to the seafloor at 17 m (Figure 3.11b). With the onset of a wave event generating a $\tau_w > 0.1$ N m^{-2}, the EI close to the seafloor increased by 3.5 dB, reaching a maximum value of 66.5 dB. This time series is depicted in Figure 3.12, with the EI abruptly increasing over a period of 8 h, and remaining high for up to two days even though the τ_w began to decrease. Sediments at M7 are fine-grained, with a mean diameter of approximately 70 μm, and will remain in suspension as τ_w decreases due to their low settling velocities and residual turbulence. The increase in EI as τ_w exceeded 0.1 N m^{-2} suggests that this is approximately the critical shear (τ_c) required for the initiation of sediment resuspension in this area.

Mooring M8 used the same instrument as mooring M7, configured to

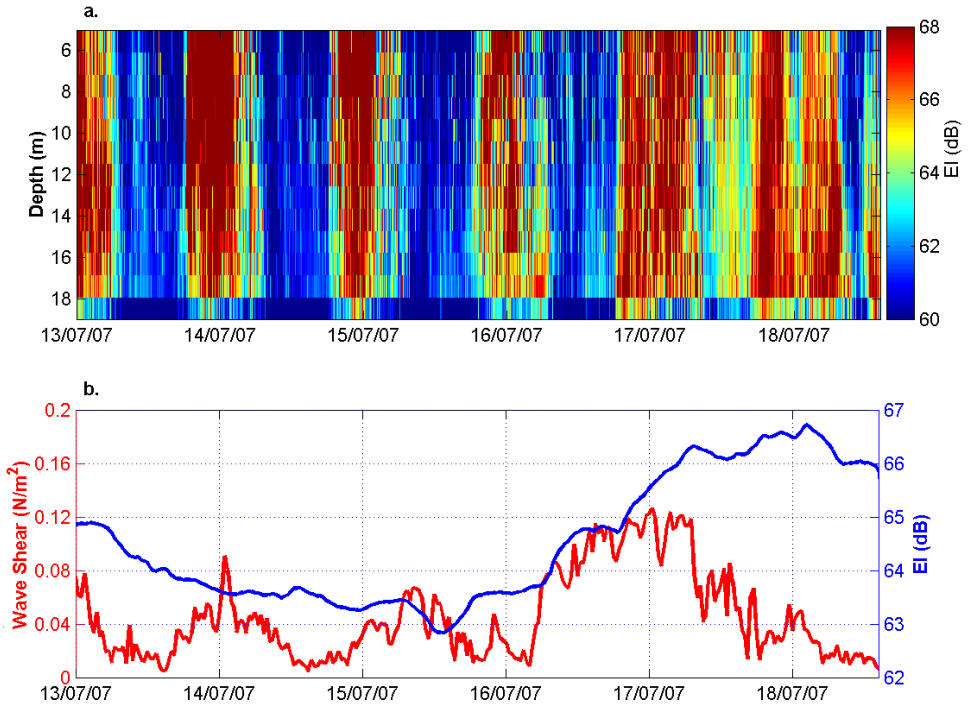

Figure 3.11: Data from mooring M7 showing (a) the distribution of EI throughout the water column and (b) the τ_w (red) and the 24 hr moving average of EI (blue) at 17 m.

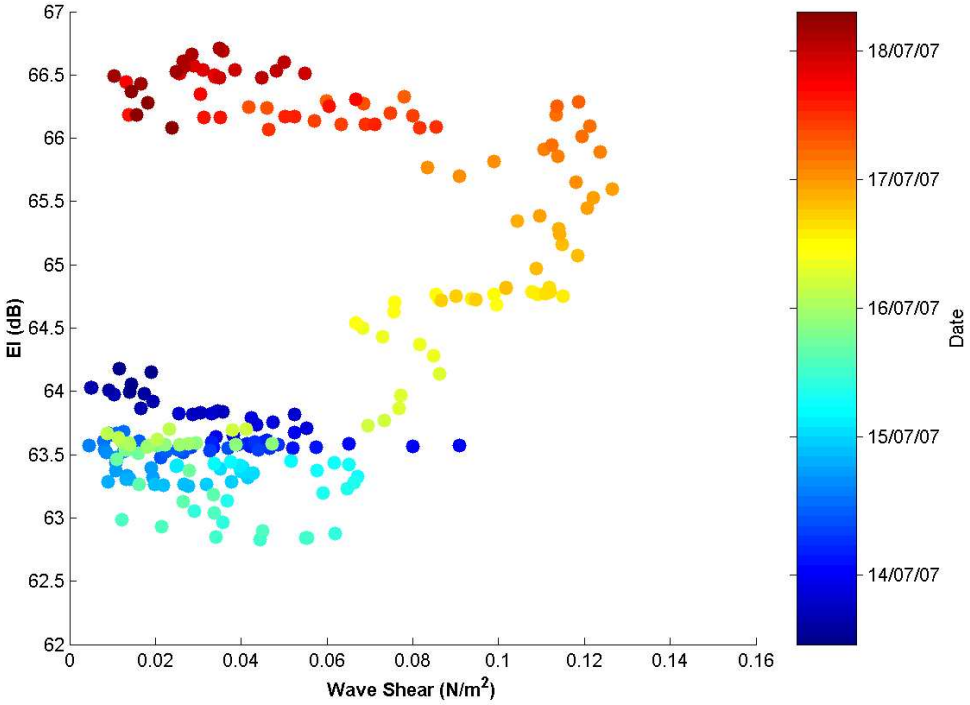

Figure 3.12: A colour-coded time series plot of wave-induced shear vs EI at M7.

burst sample at 2 Hz for 15 min every 2 h. M8 was moored outside the TFZ near the southern entrance to Thorny Passage, in the vicinity of Thistle Island (Figure 3.1). At this site, there was only a weak signal from vertical diel migrators (Figure 3.13a), perhaps a consequence of the energetic nature of the area, characterised by strong tidal flows (>0.5 m s^{-1}) and a τ_w rarely below 0.15 N m^{-2}. At this location there was a strong correlation between EI and τ_w, with EI increasing throughout the water column in response to increased τ_w (Figure 3.13b).

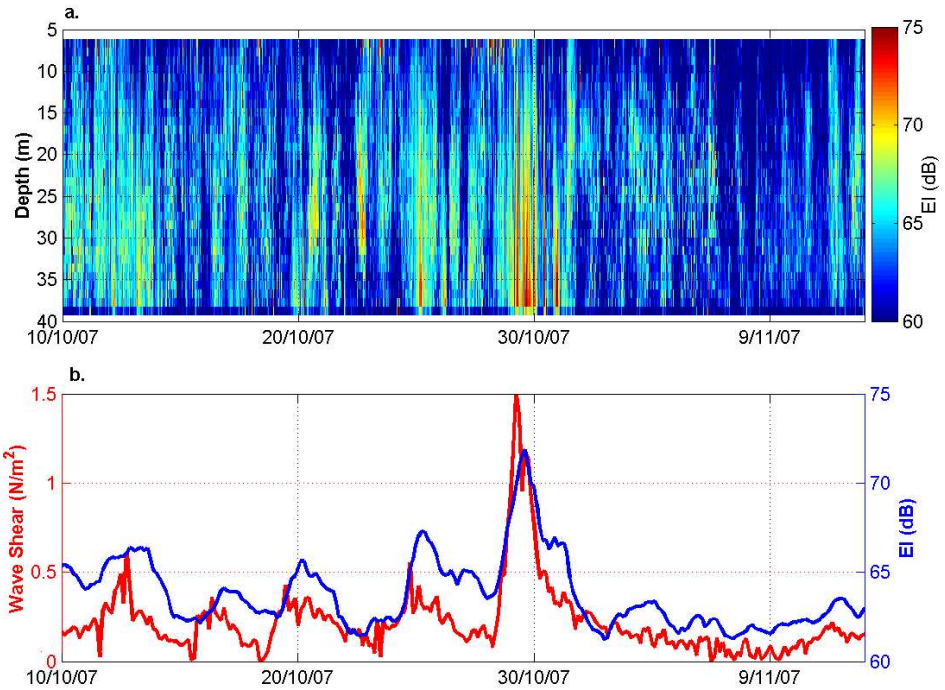

Figure 3.13: Data from mooring M8 showing (a) the distribution of EI throughout the water column, and (b) the τ_w (red) and the EI (blue) at 3.2 m above the sea floor in a water depth of 45 m.

3.4 Discussion

Sediments subjected to a $U_{sig} < 0.070$ m s^{-1} were finer, indicating that these areas are depositional in nature, whereas those subject to $U_{sig} > 0.074$ m s^{-1} were coarser and erosional in nature. By extending this principle, with intermediate values assigned to a transportational regime, a map covering the entire TFZ was developed (Figure 3.14). This seafloor classification reflects the effects of depth, exposure to fetch, shoaling, and wave refraction, which combine to create a complex set of non-linear interactions.

The mapping of U_{sig} suggests that depositional areas exist in the sheltered embayments of Proper and Boston Bay to the west of Boston Island. The region directly east of Boston Island was also classified as depositional. The region to the east of Cape Donnington was classified as erosional with U_{sig} peaking at over 0.2 m s^{-1}. This area is subject to significant amounts of bottom dissipation due to the shoaling of incoming swell as the water depth decreases from 60 m to 30 m. Of particular interest are the erosional zones in the northern embayments of Louth Bay and south of Bollingbroke Point. These regions are generally quite shallow (<15 m) and it is in these zones that shorter period wind waves will dissipate most of their energy.

The risk of resuspension in the TFZ, an area classified mostly as depositional, can be estimated from the modelled H_s and T_m. Using linear wave theory (equations 3.2 and 3.3), it is possible to derive relationships between H_s, T_m and total water depth, to find the required combination to exceed a certain critical threshold of U_b, which based on the results of the cluster analysis is 0.07 m s^{-1} in depositional zones (Figure 3.15). A detailed description

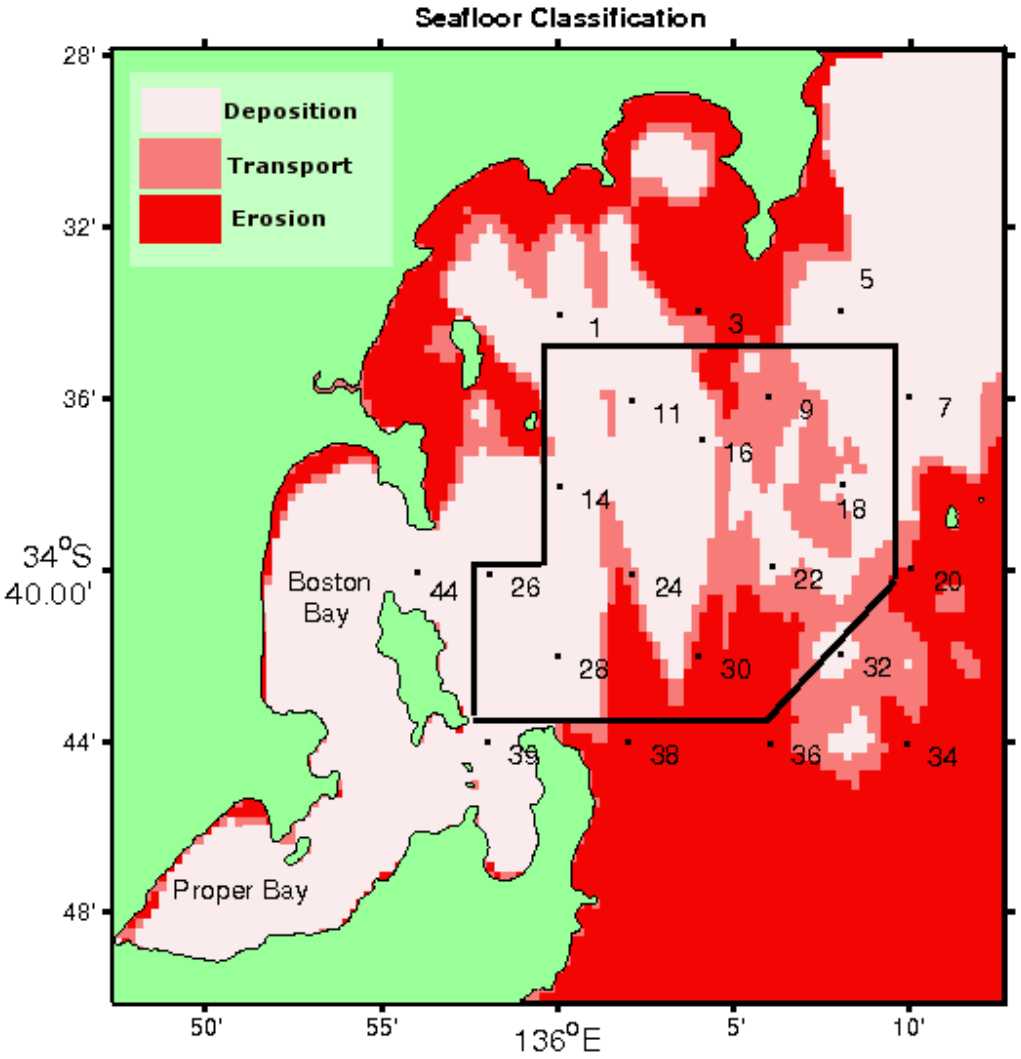

Figure 3.14: Seafloor classification based on U_{sig} for the entire model domain.

of the wave regime of the TFZ is presented in Chapter 2. Normal conditions for the TFZ (Figure 3.15; green shading), have T_m ranging from 2 to 4 s, with a typical H_s of <0.5 m. These conditions are not energetic enough to generate sediment resuspension in water deeper than 5-8 m. Therefore, under normal conditions there is little possibility of sediment resuspension in the current TFZ. Typical wave conditions during storm events (Figure 3.15; red shading), generate T_m's between 4 and 6 s with H_s reaching 0.8-1.2 m. During storm events, if waves with a period of 5-6 s and height of 1 m propagate into the TFZ, orbital velocities can exceed 0.07 m s^{-1} in regions shallower than 20-22 m deep, in which case sediment resuspension may occur.

The swell height in the TFZ typically ranges between 1% and 10% of the value at Cape de Couedic (see Chapter 2). The swell height in the TFZ is sensitive to the incident direction, with swell entering from between 180 °N and 200°N generating the greatest heights. Figure 3.15 (blue shading) suggests that swell has the greatest potential to cause sediment resuspension, as it requires a wave height of >0.45 m to generate U_b in excess of 0.07 m s^{-1}. Such conditions are most likely to occur if swell enters the region from S-SSW with an oceanic height of > 5 m. To assess the wave conditions that pose the greatest risk to aquaculture activities, a 2-D histogram of H_s and T_m is produced from a two year model run (Figure 3.16). Two contours (dashed lines) are overlaid on the histogram displaying the required combination of H_s and T_m to exceed the threshold value of 0.07 m s^{-1} in the depositional zone. The 0.1 m s^{-1} contour is breached less than 0.1 days per year. This histogram clearly demonstrates that swell entering the TFZ represented the greater risk to aquaculture activities.

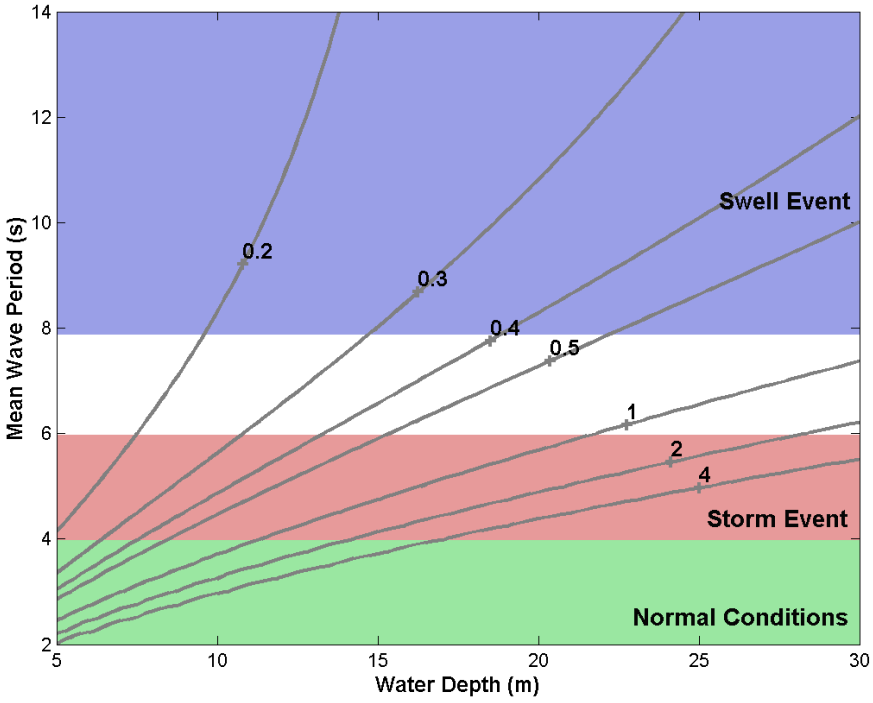

Figure 3.15: The contours in this figure show the required wave height (H_s in m) as a function of water depth and mean wave period (T_m) to exceed the orbital velocity of 0.07 m s^{-1}. Shading indicates the typical values of T_m for various conditions.

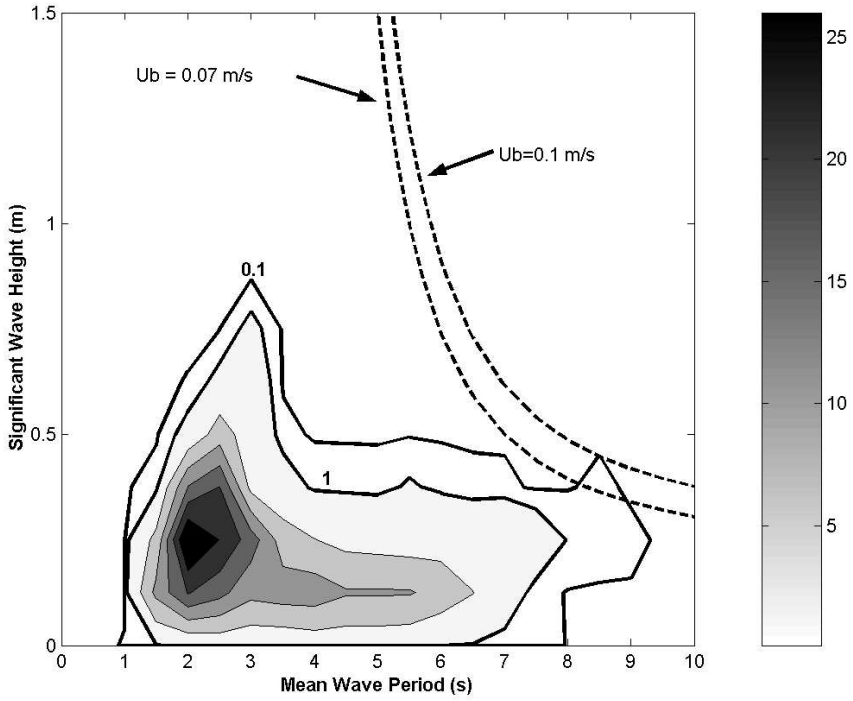

Figure 3.16: A 2-D histogram of the number of days that a unique combination of significant wave height and mean wave period occur at M7 in 22 m of water. The bins have a width of 0.5 s for the period and a height of 0.125 m for the significant wave height. The dashed contours indicate the required combination of significant wave height and mean wave period to achieve the indicated speeds. The bottom orbital velocity of 0.07 m s^{-1} indicates the speed at which τ_c is exceeded, the second contour of 0.1 m s^{-1} is included for perspective.

Observations of EI, both in the TFZ (M5 and M7) and from the far more energetic Thistle Island (M8), show a distinct relationship between the wave-induced bed-shear and resuspension events. The relationship between EI and τ_w is more complex in the TFZ, potentially a consequence of differing sediment types between the two locations. The linear relationship at M8 suggests that as τ_w increases, the sediment is rapidly resuspended. There appears to be no lag between the decrease in τ_w and a decrease in EI. This suggests that the sediments in this area have a much larger grain size and therefore the suspended sediment rapidly settles after τ_w decreases. The relationship between EI and τ_w at M7 suggests that once τ_c is exceeded in the TFZ, sediments are resuspended and remain in suspension for some time after the event due to the low settling velocities of the finer grained particles inherent to this location. It is unclear exactly how long they remain in suspension, but the EI at M7 remained high for at least 2 days after the event. The observed value of τ_c for the TFZ is 0.1 N m^{-2}, based on EI data.

The theoretical τ_w thresholds, calculated from the Shields parameter (S^*) (Nielsen, 1992b), for the initiation of sediment motion (Table 3.4) for the major groups identified by the cluster analysis of U_{sig} is $>$ 0.20 N m^{-2} in erosional zones, and 0.08-0.18 N m^{-2} in depositional areas largely made up of silts and fine sands. These theoretical resuspension thresholds agree remarkably well with the observed sediment resuspension thresholds of 0.1 N m^{-2}.

In the areas classified as depositional, fine material originating from aquaculture activities, is able to settle out of suspension. Along with this fine material, organic matter is also deposited, and it is within these depositional

Table 3.4: The theoretical shear stress required to initiate sediment movement within erosional and depositional zones within the TFZ.

	Depositional	Erosional
Mean Grain Size (μm)	<180	>250
s	2.43	2.8
ψ_c	0.06	0.05
τ_c	0.08-0.18	>0.2

zones that sediment resuspension events pose the greatest risk to aquaculture activities. If sediments containing high concentrations of porewater nutrients are resuspended, water column primary productivity may be stimulated resulting in the potential for harmful algal blooms. A thorough investigation of the geochemical nature of the sediments is presented in Part II of this thesis, and the potential risk to the aquaculture industry is explored in greater detail.

3.5 Conclusion

Field observations show that there are weak sediment resuspension events occurring within the current TFZ. The measured events do not persist for longer than 1-3 days and are typically confined to the lower 10 m of the water column. Tuna pens typically have a wall depth of 10 m, so that the fish are unlikely to be affected by these events. However, the wave events recorded in this study would not be considered highly-energetic storm events that may occur with a frequency of 1 every 5-10 years, but rather typical wave events associated with the passage of synoptic scale weather events that occur 5 - 10 times per year depending on the location.

During resuspension events, fine sediments such as silts and fine-sands can become resuspended. It is these size fractions that were found in abundance in the mucus contained in the gills of the tuna during the 1996 mortality event. Once these fine sediments come into suspension, the turbulence associated with such storm/swell events will keep them in suspension for many days. Ambient currents are then able to transport the resuspended sediments over large areas, moving them from the regions where the resuspension was initiated.

The implications of the seafloor classification and sediment resuspension derived in this work for the tuna industry are dependent upon the locations of individual operators. Lease sites located within depositional areas may be subject to decreases in water quality during high-energy storm or swell events. When T_m exceeds 8 s during swell events, there is the potential for sediment resuspension at a 20 m water depth typical of tuna pens if the swell

height is over 0.45 m. In the case of a storm event, when T_m = 4-6 s, if the significant wave height exceeds 1-2 m, there is an increased risk of sediment resuspension. During storm events the wave height rarely exceeds 1 m in the central TFZ (see Chapter 2), therefore swell events pose the greatest risk for sediment resuspension.

Part II

Sediment Biogeochemistry

Chapter 4

Sediment geochemistry

4.1 Introduction

The current aquaculture practices for Southern Bluefin Tuna (SBT) in South Australia are a legacy of the reduction in the wild caught quota from 14500 tonnes in 1988/1989 to the present level of 5265 tonnes per annum. The reduction in the quota led to the current system of value-adding through aquaculture. In 1991, less than 0.5% of the wild quota was used in the value-adding process, but it now accounts for more than 95% of the total wild quota (Clarke, 1996). In 1996 a particularly energetic storm event led to a sediment resuspension episode within Boston Bay (Figure 4.1) that caused the mortality of approximately 75% of the farmed tuna. Since 1997 the SBT farms have been relocated from the protected waters of Boston Bay to the outside of Boston Island in south-western Spencer Gulf. It is thought that the present location is less prone to such events as the higher current speeds of the area are likely to disperse any aquaculture waste material over a wider

area.

Sediments found in lower Spencer Gulf share properties of those found both in northern Spencer Gulf and those of the adjacent shelf (Fuller *et al.* , 1994). Within this region the continental shelf forms one of the largest cool-water carbonate facies in the world. A discussion of the sediments and geochemistry of SW Spencer Gulf can be found in Fernandes *et al.* (2006), who's findings compliment those of Porter-Smith *et al.* (2004) and suggest that sediments within this region are mobilised by wind waves and swell as well as tidal currents. Evidence suggests that waves in the region of the tuna farming zone (TFZ) interact with the bottom, winnowing-out the fine-grained sediments in the more exposed locations (see Chapter 3).

Spatial variation in marine sediment geochemistry is a reflection of the combined effect of physical and biological processes inherent to the region (Chester, 2003). In coastal environments, human activities can also influence the sediment geochemistry through increased nutrient loads and sedimentation. Over the last few decades, there has been a substantial increase in aquaculture activities in the coastal zone, which has generated an increased research interest in examining the environmental impacts ranging from shell fish production (for example mussels and oysters) (Christensen *et al.* , 2003), through to the intensive farming of marine finfish (Fernandes *et al.* , 2007b). Aquaculture activities act as point sources for nutrients, which in oligotrophic regions, can artificially stimulate the marine ecosystem (Hecky & Kilham, 1988; Herbert, 1999). The findings of Lauer (2005) clearly show an enhancement of benthic metabolism adjacent to SBT pens, driven by the flux of organic matter to the seabed. The ability of the sedimentary

ecosystem to assimilate this organic load is dependent upon the physical, chemical and biological processes inherent to the area.

Physical processes such as surface gravity wave (hereon called wave) induced oscillatory flows and tidal currents, impact upon the morphological (such as ripple formation) and textural characteristics (grain size and sorting) of the sediments. Waves act as a sediment sorting mechanism, whereby fine grained sediments are winnowed out and then transported by the tidal or residual currents to less energetic areas where they can be deposited (Nielsen, 1992b). In regions of high wave energy, the sediments are often dominated by coarser fractions resulting in higher mean grain sizes. Due to the permeable nature of coarse sands, this winnowing effect, which combined with ripple formation, has implications for the porewater concentrations and oxygen profiles in the sediments (Precht & Huettel, 2003). Waves and tidal currents cause flushing of the porewater spaces, leading to well oxygenated regions in the upper layers of the sediments, which in turn affect the biology of the sediments (Huettel *et al.* , 2003). This advective flushing of the porewater nutrients has been found to exceed molecular diffusion by up to 2 orders of magnitude (Jahnke *et al.* , 2005).

In this study, the work of Fernandes *et al.* (2006) is extended through sampling sediments in the TFZ at a higher spatial resolution on the grid in Figure 4.1. The following variables were measured:

- Mineral grainsize
- Carbonate content
- Porewater nutrients (NH_4^+ and PO_4^{3-})

- Organic carbon (OC), total phosphorus (TP) and total nitrogen (TN)
- Stable isotopes of carbon and nitrogen

A variety of geostatistical techniques were then applied to investigate the spatial distribution of these variables. Furthermore, regions containing similar geochemical characteristics were identified. The goal of this study was to qualitatively assess the interaction between aquaculture inputs and physical processes on the geochemistry of the sediments in south-west Spencer Gulf.

4.2 Methods

4.2.1 Sampling

Sediment cores were collected at each of 21 stations (Figure 4.1) for mineral grain size analysis, the determination of porewater ammonium ($NH_4^+ + NH_3$) and phosphate PO_4^{3-}, and sediment carbonate, organic carbon, total nitrogen, total phosphorus and the isotopic composition of carbon and nitrogen. The cores were collected using a ship-deployed HAPS Corer (KC Denmark) (Figure 4.2). Cores were 6.7 cm in diameter and 10-15 cm in length. Upon retrieval, the overlying water in the tube was carefully discarded to minimise surface disturbance and the sediment extruded onto a clean stainless steel table. The sediment cores were analysed for porewater nutrients, geochemical composition and textural characteristics.

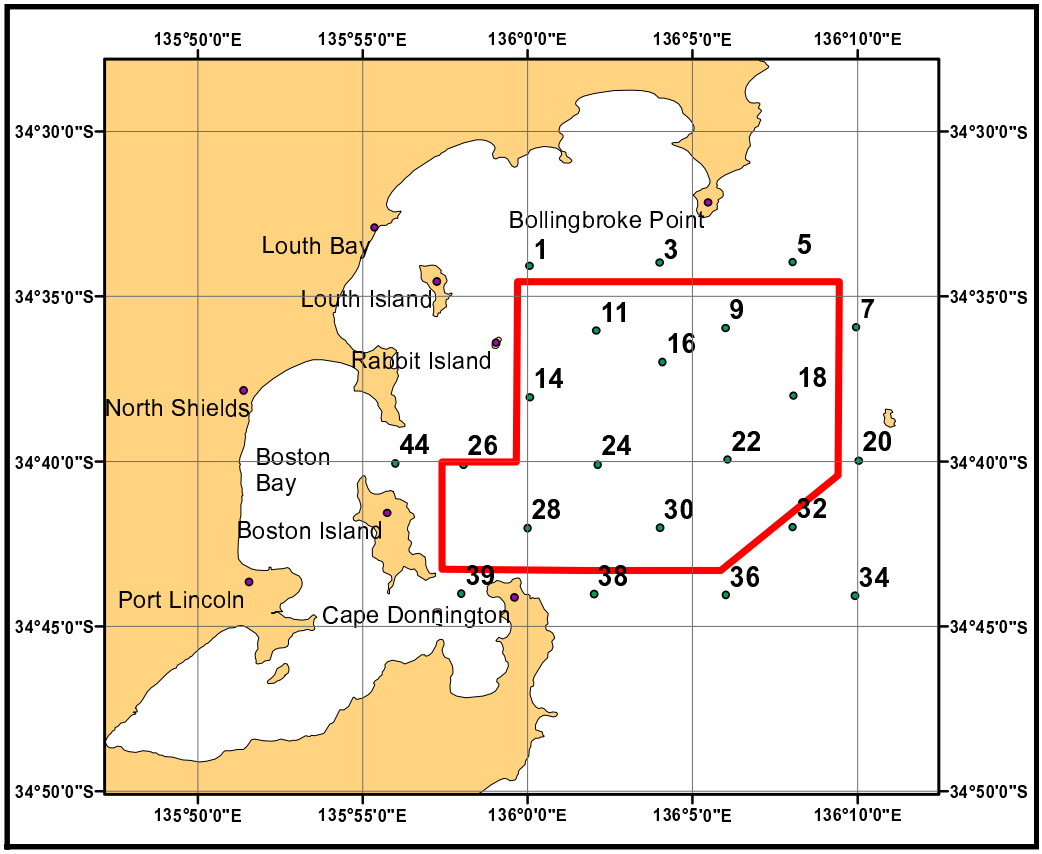

Figure 4.1: Sampling sites where sediment samples for geochemical analysis were taken. The red border corresponds to the approximate location of the tuna farming zone boundary.

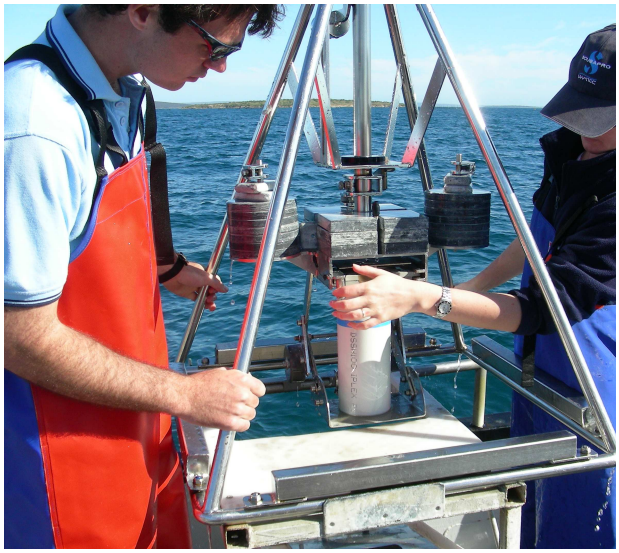

Figure 4.2: The HAPS corer used to collect sediment samples for geochemical analysis.

Porewater analysis

Two replicate cores were collected for porewater analysis, the top 2 cm transferred into 50 ml centrifuge tubes, and stored on ice before transfer to the laboratory. Samples were centrifuged at 1400 g for 10 min. The overlying water was filtered through a 0.45 μm filter and stored at -20°C. Ammonium and phosphate were determined by the Water Studies Centre (Monash University, Melbourne, VIC) using a QuickChem 8000 Automated Ion Analyser (APHA-AWWA-WPCF, 1998a; APHA-AWWA-WPCF, 1998b).

Geochemical analysis

Geochemical analysis was performed on two replicate sediment cores. The top 1 cm transferred into pre-combusted glass jars, and stored on ice before transfer to the laboratory and long-term storage at -20°C. Samples were

freeze-dried, sieved through a 500 μm sieve to remove large shell fragments and homogenised with a mortar and pestle.

Carbonate content was determined by the commercial laboratory, CSBP (Perth, WA), with a pressure transducer (RS Components, part 348-8065, Iso-Tech voltameter IDM 91) by measuring the increase in pressure generated by the CO_2 released after acidification of aliquots with 5.5 M HCl at room temperature.

Organic carbon and total nitrogen contents, and their isotopic signatures, were analysed by the Isotope Analysis Service at CSIRO Land and Water (Adelaide, SA) using a Europa Scientific ANCA-SL elemental analyser coupled to a Geo 20-20 Mass Spectrometer. Aliquots for organic carbon analysis were pre-treated with 1 M hydrochloric acid to remove carbonates, rinsed with MilliQ water to remove hygroscopic salts and oven-dried at 40°C using a method modified from Hedges & Stern (1984). Organic carbon concentrations were corrected for the loss of carbonate during pre-treatment.

Natural isotopic abundances for organic carbon and nitrogen are reported as δ^{13}C and δ^{15}N, which correspond to the deviation (in ‰) of the isotopic composition of a sample from an internationally accepted standard (std) (Pee Dee Belemnite limestone for δ^{13}C and nitrogen in air for δ^{15}N):

$$\delta^{13}C, \delta^{15}N = \left(\frac{R_{sample}}{R_{std}} - 1 \right) \times 10^3 \tag{4.1}$$

where

$$R = \frac{^{13}C}{^{12}C}, \frac{^{15}N}{^{14}N} \tag{4.2}$$

Total phosphorus content was determined by the Marine and Freshwater Research Laboratory (Murdoch University, Perth, WA) using a Varian Vista Axial Inductively Coupled Plasma-Atomic Emission Spectrometer (ICP-AES) after digestion with nitric acid, hydrogen peroxide, and hydrochloric acid (US Environmental Protection Agency, 1991).

Grainsize analysis

Grainsize analysis was undertaken on the top one cm of two replicate cores. The samples were transferred into pre-combusted alfoil trays, and stored on ice before transfer to the laboratory and long-term storage at $-20°$C. The analysis method is detailed in Fernandes *et al.* (2006), whereby clay was analysed with a hydrometer and larger grainsizes were separated using a series of stacked sieves of 2000, 1000, 500, 250, 125 and 63 μm mesh sizes. Silt was calculated as the difference between the total weight of sediment, and the sum of the clay and sand fractions. Each grainsize was then presented as a percentage of the total weight. The statistics of particle size distributions (mean grain size, sorting, skewness and kurtosis) were calculated using the GRADISTAT software developed by Blott & Pye (2001). The Folk and Ward method (see Blott & Pye (2001)) was used to analyse the data due to it being relatively insensitive to large variations in the tails of the sediment distribution.

4.2.2 Statistical analysis

The objective of the statistical analysis of the geochemical data was to identify relationships between the variables and locations. Two different questions were addressed; 'Which variables follow a similar spatial pattern?', and, 'Which locations have a similar combination of geochemical variables?'. Initial scatter plots and histograms were produced to examine any obvious relationships and the distribution of the data. A log-transform was then applied to help normalise the data. The data was further standardised by dividing the observations of each variable by the standard deviation of the variable.

Due to the multivariate nature of the data, three techniques were used. A hierarchical cluster analysis (HCA) using the complete Euclidean distance between the sediment nutrient contents of organic carbon, total phosphorus, total nitrogen, and porewater nutrient concentrations (ammonium and phosphate) was used to identify the major geochemical groupings within the study region. To verify the clusters found in the HCA, two other independent techniques were also applied. The first was a K-means cluster analysis which assumes that the variables form a vector space in n dimensions, where n is the number of variables considered in the HCA. The K-means cluster analysis then attempts to find k clusters within the n dimensional vector space. The K-means algorithm attempts to minimise the total intra-cluster variance about the mean point in each cluster. An alternative was the use of a Principal Component Analysis (PCA) with the same variables used in the HCA. Finally, a multi-variate analysis of variance (MANOVA) with the

variables previously mentioned was used to test whether there were significant differences in the means between the two groups identified in the cluster analysis. Univariate tests using a Kruskal-Wallis non-parametric one-way ANOVA, were then conducted to investigate the differences in individual variables between the geochemical groups.

4.2.3 Spatial interpolation

The 21 cores were collected in a grid pattern to allow for spatial interpolation. Replicate samples were collected at each station. For the spatial analysis, results from each replicate were averaged. An assumption that underlies many interpolation techniques is that the measured data originate from a normal distribution. To verify this assumption, all the observed variables were plotted in Quantile-Quantile (QQ) plots to test for data normality. If the observed data originate from a normal distribution, then the QQ plot should approximate a straight line, especially in the central region of the plot. Where significant deviations from normality was apparent, a log or arc-sin transform was applied. Generally the transform corrects for the non-normality in the data, but in extreme cases, where there were obvious outliers at lower and upper ends of the QQ plot, the individual data points were flagged and examined in more detail. If the extreme value was due to an individual replicate introducing a severe bias, the offending replicate was discarded. If there was agreement between the two replicates, the station was then flagged as an outlier and considered later during the interpolation routine.

The goal of spatial interpolation is to define a geostatistical model (f) that will predict a variable of interest at a location (x^*) from observations of f at the observed locations $x_1 \ldots x_n$. $f(x^*)$ is then a prediction at the location x^*. Various interpolation techniques can be applied, in the simplest form, x^* could be given the value from its closest neighbour, usually called nearest neighbour interpolation. In this form a surface of polygons are formed and all the values within each polygon are uniform in value, the resulting surface is called a Voroni map. The creation of a Voroni map is a good starting point to explore the possible spatial trends in the data.

A slightly more complex method to estimate the prediction surface is to use an Inverse Distance Weighting (IDW) scheme. Such a scheme takes into account the values from surrounding observations and weights closer observations more highly then those further away. This is a deterministic scheme that does not give an error prediction map. Inverse distance weighting fits a surface that passes through all the observed values. This can result in a surface that appears to have a number of concentric peaks, in areas where the measures are significantly different to the other surrounding measurements. A more advanced prediction technique is required if the effects of outliers and small scale variability are to be taken into account.

A far more robust method in estimating the prediction surface and associated error map is to use Kriging. Kriging is a linear least squares estimation algorithm. The Kriging estimator ($f(x^*)$) is given by a linear combination of:

$$f(x^*) = \sum_{n=1}^{N} w_i(x^*) f(x_i) \tag{4.3}$$

with observed values ($f_i = f(x_i)$) with weights ($w_i(x^*)$) chosen such that Kriging error ($\epsilon(x)$):

$$\epsilon(x) = f(x) - \sum_{n=1}^{N} w_i(x^*) f(x_i) \tag{4.4}$$

is minimised (Cressie, 1993).

To investigate the spatial distributions of various sediment characteristics, ArcMAP GIS software was used. Two interpolation schemes were implemented. For all geochemical variables a Voroni Map was initially produced to give a quick indication of any spatial trends present in the data. Kriging was then used for the spatial interpolation of the data. Kriging allows for the output of two maps; the trend surface $f(x^*)$, and a standard error map associated with that trend surface.

4.3 Results

4.3.1 Exploratory analysis

All of the observed variables from each of the 21 sites were collated and the raw data plotted in a matrix plot (Figure 4.3). Each column and row represents a variable. On the principal diagonal, the histogram of that particular variable is given. A cursory examination of this plot reveals very few

clear relationships. The carbonate histogram does not follow a normal distribution and there appears to be no relationship between carbonate and the other variables. Organic carbon (OC) again shows little normality and some weak positive linear relationships with sedimentary total nitrogen (TN) and also δ^{13}C. Sedimentary total phosphorous (TP) potentially follows a normal distribution but for two outliers, which skew the distribution to the right. TP shows little linear relationship to the other variables. The distribution of TN forms a similar distribution to that of TP. Once again there are two outliers which skew the distribution to the right. TN appears to show weak positive linear relationships with OC, porewater NH_4^+ (PWNH4) and δ^{13}C. The porewater nutrients of PWNH4 and PO_4^{3-} (PWPO4) are positively correlated and both variables share a weak positive relationship with TN. The sedimentary isotope ratios of δ^{13}C and δ^{15}N again appear to have a weak linear relationship with each other. δ^{13}C and OC, TN, PWNH4 and PWPO4 all show signs of weak positive relationships. δ^{15}N shows no obvious relationship with any other sediment variable with the exception of δ^{13}C.

Before any other statistical test was performed, three transforms (inverse, log and arctan) were applied to the data to try and normalise the distributions. To visually inspect the variables distributions, QQ plots of the non-transformed and transformed data were produced. If the data were from a normal distribution, the QQ plot would be linear. The inverse and arctan transforms correct for overdispersed data, whereas the log-transform can correct skewed data. A matrix of QQ plots is contained in Figure 4.4. Most of the non-transformed variables appear to be normally distributed with the exception of a couple of outliers in the OC, TN, TP, PWNH4 and PWPO4.

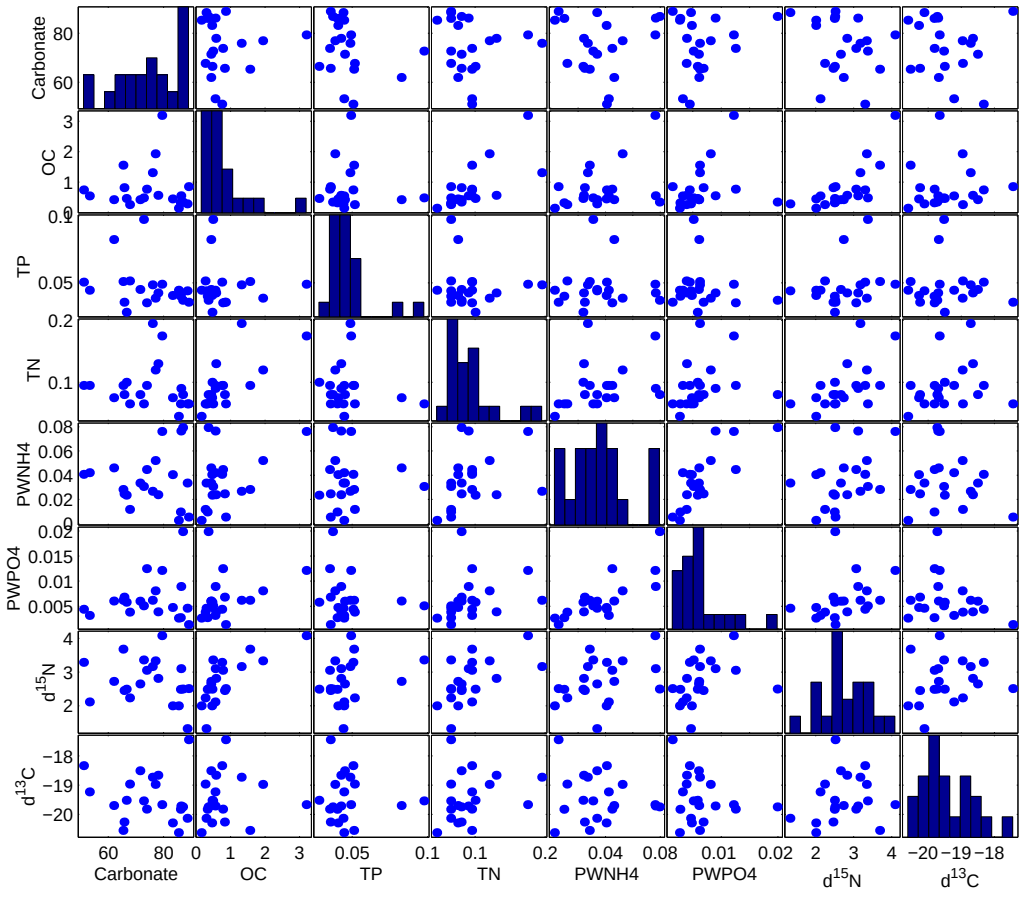

Figure 4.3: A matrix plot of the raw data for the variables of carbonate, organic carbon (OC), total phosphorous (TP), total nitrogen (TN), porewater NH_4^+ concentration (PWNH4), porewater PO_4^{3-} concentration (PWPO4) and the isotopic ratios of $\delta^{13}C$ ($d^{13}C$) and $\delta^{15}N$ ($d^{15}N$). The diagonal contains the histogram of each variable.

These outliers occur at the higher end of the data, which indicates that the data is skewed to the right. This observation supports the findings from the histograms in Figure 4.3. When an inverse transform in applied, the tails of the resulting QQ plots deviate from the straight line. The log transformed data follow a straight line far better than either the inverse or arctan transforms. However the log transformed data do not perform substantially better than the untransformed data.

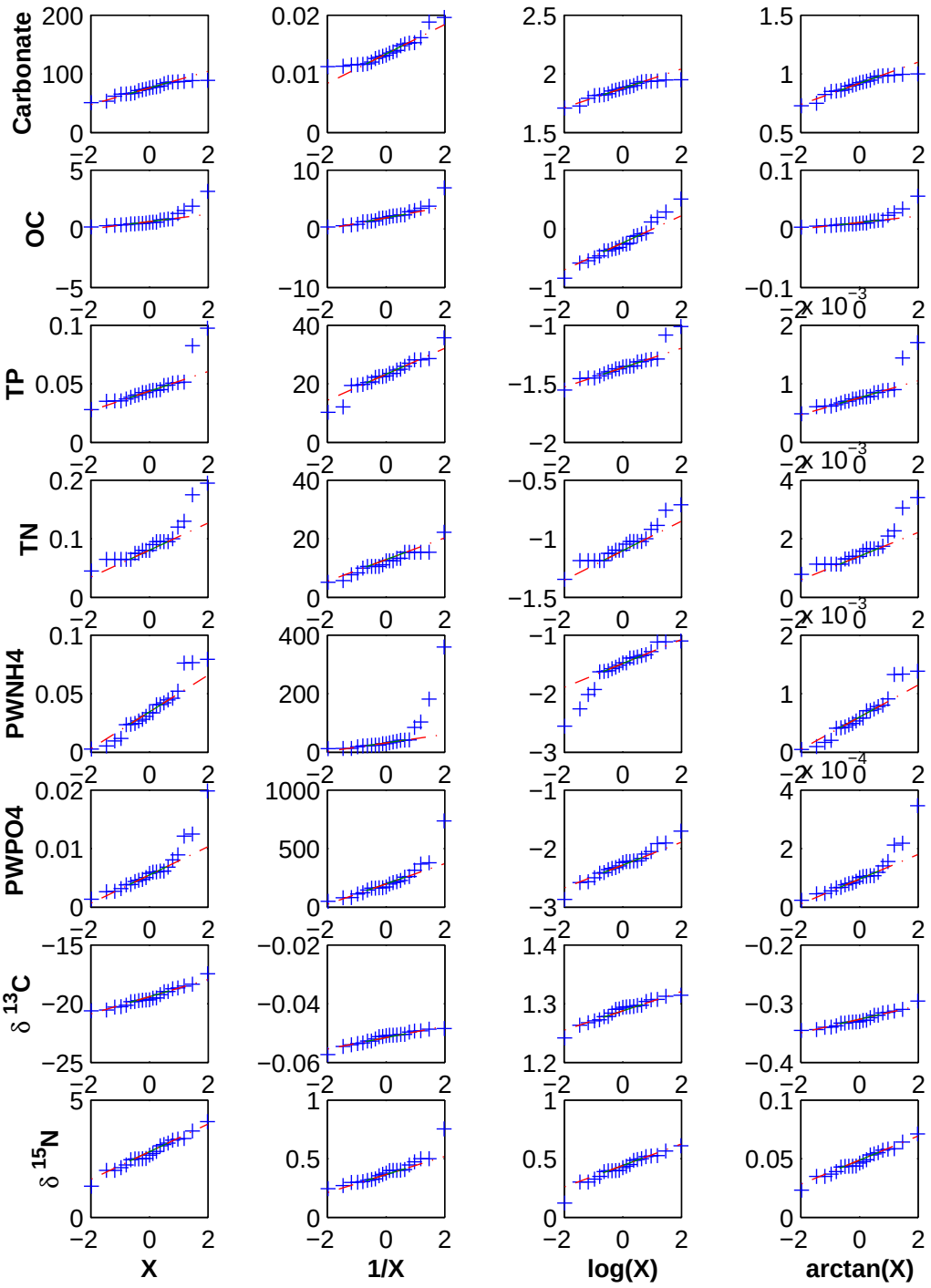

Figure 4.4: A matrix plot with the resulting QQ plots for the raw data (X), inverse transform (1/X), $\log_{10}$ transform (log(X)) and the arctan transform (arctan(X)).

4.3.2 Cluster analysis

Hierarchical cluster analysis

A hierarchical cluster analysis (HCA) using the sediment nutrient variables of OC, TN, TP, PWNH4 and PWPO4, was used to identify the major geochemical provinces in the study area. The data were standardised by dividing each of the variables by their respective standard deviations. Euclidean distances were then calculated and used to form a dendrogram (Figure 4.5). Two major sediment groups were found. To verify the major groups were not just an artifact of the clustering scheme used, a K-means analysis and principal component analysis (PCA) were also performed.

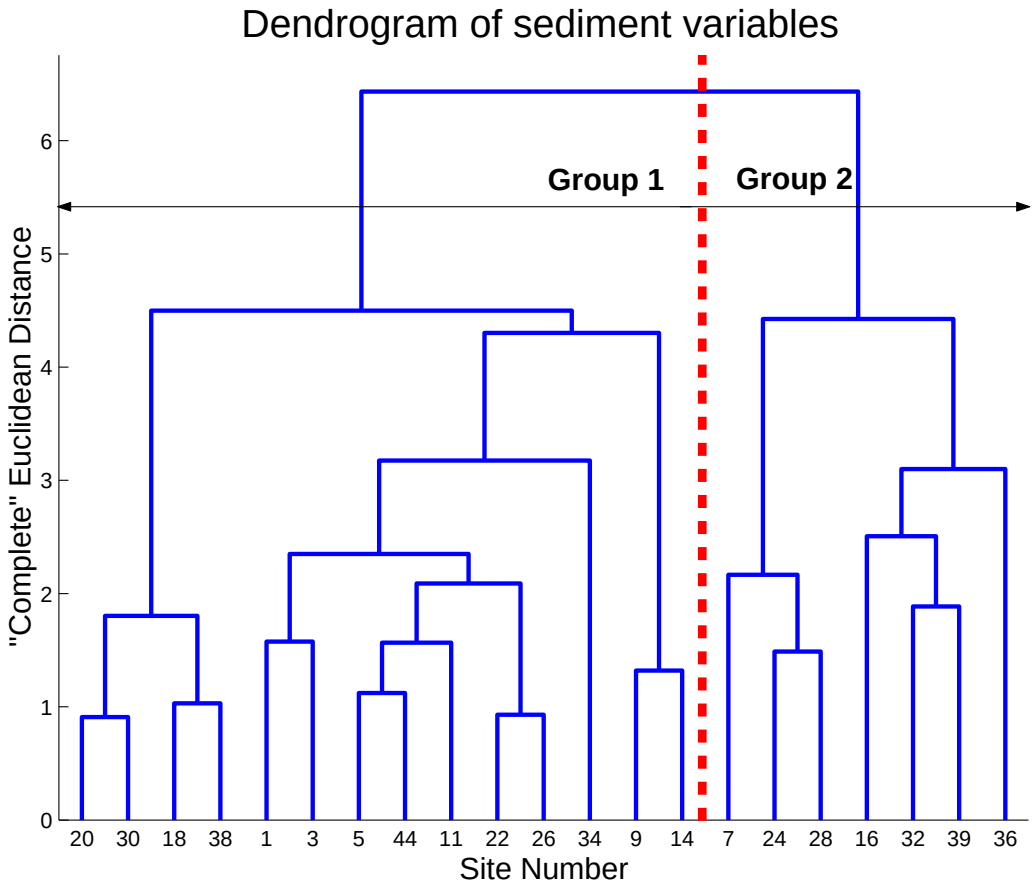

Figure 4.5: A dendrogram using the complete Euclidean distances between standardised sediment nutrient variables.

K-means cluster analysis

The results from the K-means cluster analysis agree well with those from the HCA. The spatial distribution of the HCA and K-mean groups are compared in Figure 4.6. Group 1 sediments form the largest group and cover much of the study region. The sediments forming Group 2 fall on an axis oriented in the SW to NE direction running through the central tuna farming zone.

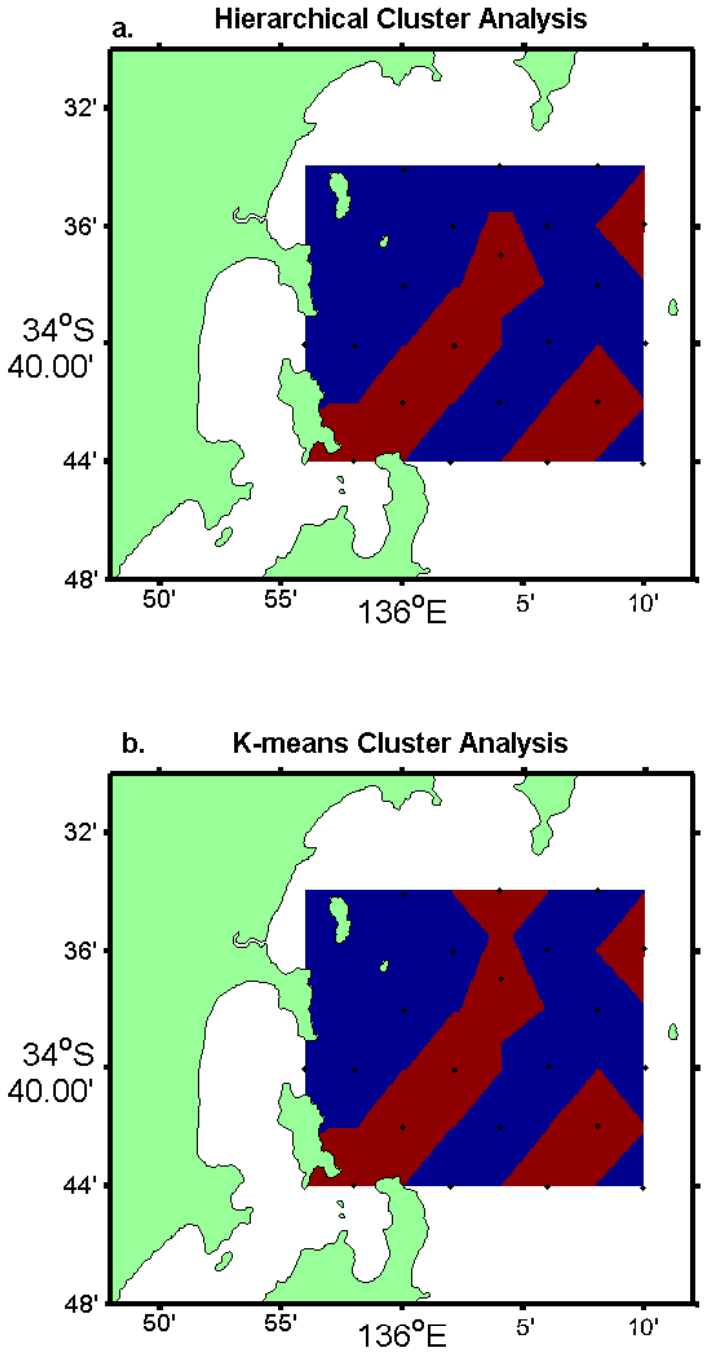

Figure 4.6: The results of a Hierarchical Cluster Analysis (a) and a K-means Cluster Analysis (b).

Principal component analysis

A third method applied to the data uses Principal Component Analysis (PCA). The groups identified in the HCA and K-means analysis are separated only by the first principal component (Figure 4.7), which accounts for approximately 37% of the observed variability (Figure 4.8). The variables that drive the difference between the two groups in the first principal component are organic carbon, total nitrogen and both porewater nutrients. These variables are all negatively correlated with the first principal component with correlation coefficients < -0.65. Finally a MANOVA confirms that sediments from the two groups have significantly different means (p-value = 0.0027).

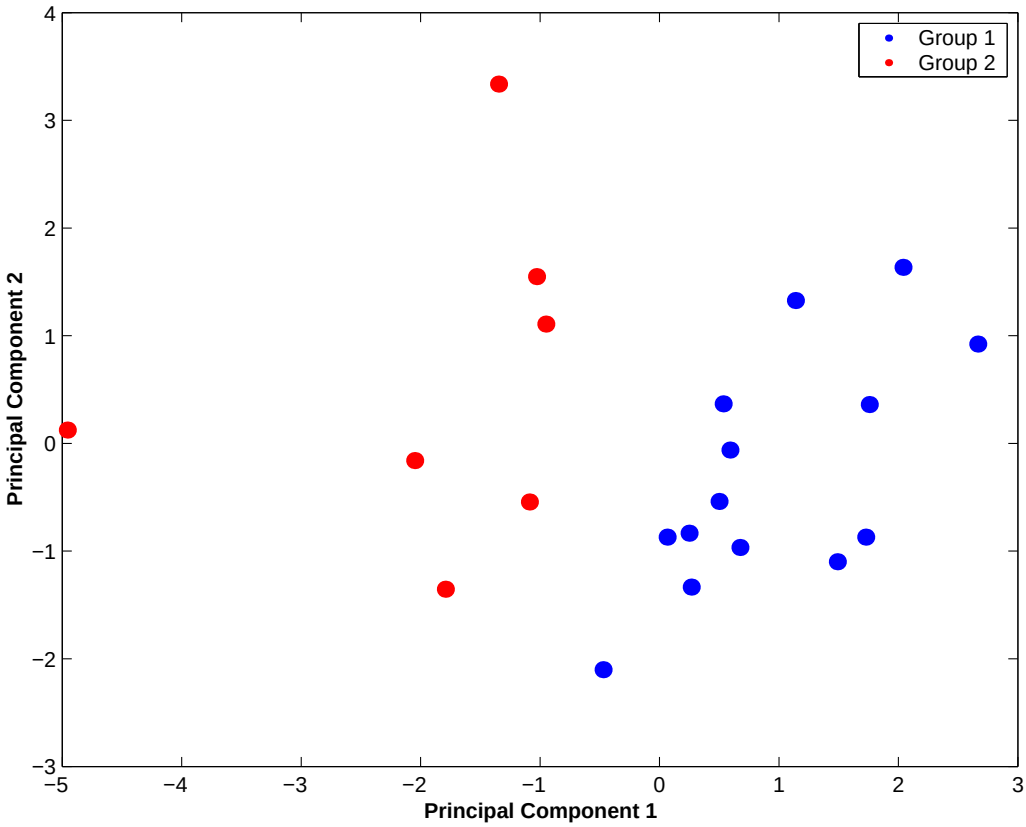

Figure 4.7: A scatter plot of the first principal component plotted against the second principal component based on the standardised sediment nutrient variables.

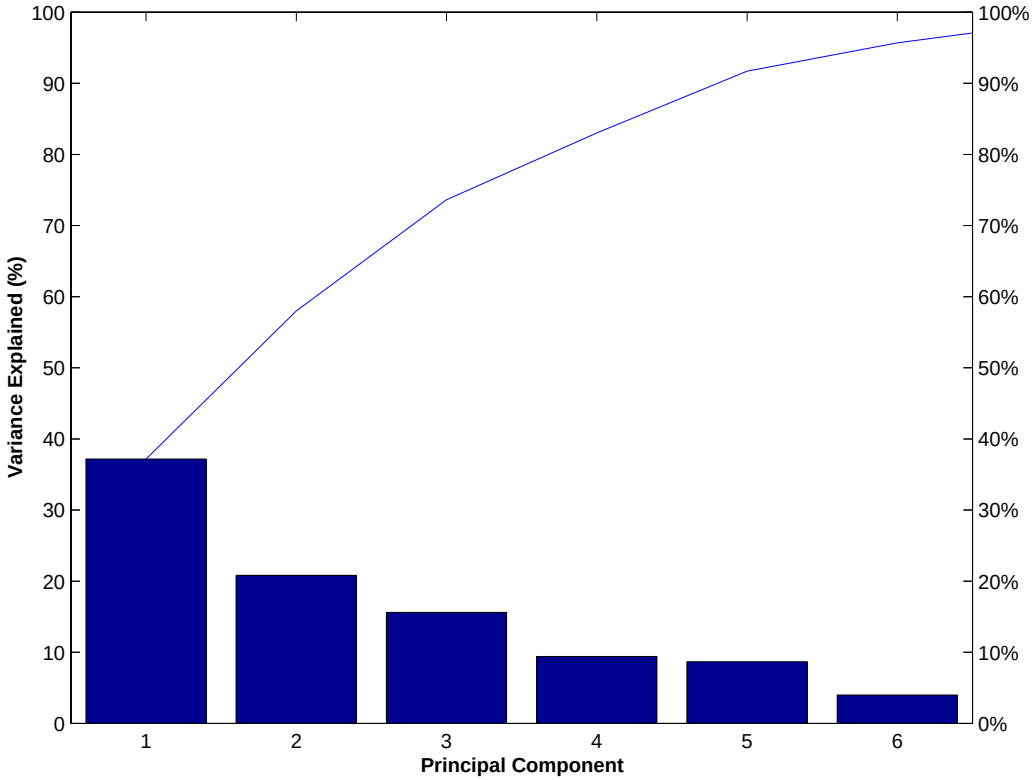

Figure 4.8: A Pareto plot displaying the individual and cumulative variance explained by each of the principal components.

Univariate analysis between the sediment groups

Analysis of the univariate statistics highlighted the major differences between the two groups identified by the HCA. The results of the Kruskal-Wallis test showed Group 2 sediments are significantly more nutrient rich with TP being the exception (Table 4.1). Nutrient concentrations for Group 2 sediments, in particular OC, N, PW NH4 and PW PO4, are typically 2-3 times those values in Group 1.

To investigate the differences between the two sediment groups in more detail, a second statistical analysis using grain size variables, not included in the cluster analysis, was also performed (Table 4.2). There were only four statistically significant textural differences between the two groups. Group 2 sediments contained a higher percentage of silts (4-63 μm), and a lower percentage of fine sands (125-250 μm), than the sediments in Group 1. This difference in fine fractions between the two groups explains the differences in the grainsize parameters of sorting and kurtosis. Using the classification system of Blott & Pye (2001), sediments in Group 2 are extremely poorly sorted and leptokurtic, while those in Group 1 are very poorly sorted and very leptokurtic.

Table 4.1: The results of a Kruskal-Wallis non-parametric analysis of the main groups identified by the cluster analysis. Variables with a statistically significant difference between the groups are highlighted in bold.

Geochemical Variable	Group 1 (n=14)	Group 2 (n=7)	p value
Carbonate (%)	72.87	77.79	0.4118
Organic Carbon (%)	0.48	1.38	**0.014**
Total Phosphorus (%)	0.049	0.043	0.681
Total Nitrogen (%)	0.079	0.121	**0.013**
PW: NH4 (μmol/L)	26.0	55.0	**0.011**
PW: PO4 (μmol/L)	4.4	10.6	**<0.001**
$\delta^{13}C$	2.46	3.27	**0.007**
$\delta^{15}N$	-19.35	-19.59	0.551

Table 4.2: The results of a Kruskal-Wallis non-parametric analysis of the main groups identified by the cluster analysis. The grain size variables presented in this table were not included in the cluster analysis. Variables with a statistically significant difference between the groups are highlighted in bold.

Geochemical Variable	Group 1 (n=14)	Group 2 (n=7)	p value
Mean Grain Size (μm)	192.91	150.86	0.179
Grain Size Sorting	4.6	6.5	**0.031**
Grain Size Skewness	-0.23	-0.28	0.156
Grain Size Kurtosis	1.77	1.20	**0.017**
Clay (%)	5.3	6.2	0.296
Silt (%)	12.3	20.2	**0.031**
Very Fine Sand (%)	15.2	20.2	0.117
Fine Sand (%)	28.4	21.3	**0.017**
Medium Sand (%)	21.6	14.6	0.052
Coarse Sand (%)	9.7	7.1	0.111
Very Coarse Sand (%)	4.3	3.1	0.263
Granule (%)	3.0	9.6	0.602

4.3.3 Spatial interpolation

The spatial distributions of the various geochemical variables follow a complex spatial pattern. The Kriging procedure produces a prediction of the spatial distribution of a particular variable and also facilitates the production of a standard error map, but it presupposes the data has captured the spatial correlation. Some variables exhibited low spatial correlation, and this accounts for the high standard error associated with these variables. When interpreting the data, both the spatial interpolation and the standard error map need to be considered; areas to the west and south-west of Rabbit Island and immediately east of Boston Island are particularly susceptible to high error. This is due to the lack of sampling sites in these regions.

The mean grain size for a majority of the tuna farming zone ranges between 60 to 140 μm (Figure 4.9). There are isolated pockets that contain coarser sediments. These areas are located directly east of Cape Donnington, south-east of Rabbit Island and south of Bollingbroke Point. For a majority of the region the standard error is up to 45 μm, which is relatively high when compared to the absolute value of the observations. A major reason for this uncertainty lies in the relatively low spatial correlation between sites. To establish lower standard errors a far higher resolution sampling grid would need to be implemented, which would be prohibitively costly.

The spatial distribution of carbonate exhibits a far higher spatial correlation than the mean grain size (Figure 4.10). There appears to be a significant south to north gradient in carbonate content. The shallow near-shore regions in the north have up to 25% less carbonate then the deeper offshore areas to

the south and south-east. The standard errors associated with this prediction present a similar distribution to those in the mean grain size error map, but with a lower overall error. This is largely due to a greater spatial correlation between sites. In the central northern study region there is a large region with an error of less than 5%.

The OC content appears to be lower in the north-west and north-east when compared to regions further south (Figure 4.11). However the standard error prediction map follows a very similar pattern to that as the prediction surface. This is suggestive of a very low spatial correlation. The prediction map must therefore be examined with caution. Due to the low spatial correlation the confidence in the predictive capacity of the surface is low for this variable.

The TP exhibits a strong north-south gradient with a low standard error (Figure 4.12). There is generally good spatial correlation between the sites which provides confidence in the prediction surface. The major feature being a band of high phosphorus concentration in the north compared to the south. The distribution peaks at station 9 at 0.06% compared to less than 0.03% in the south.

The distribution of TN follows a very different distribution to that of TP (Figure 4.13). Once again the standard error map displays reasonable spatial correlation between sites. A majority of the region has TN percentages of less than 0.08% with the exception of the southern entrance to Boston Bay and in the vicinity of site 36.

The concentrations of PWPO4 (Figure 4.14) and PWNH4 (Figure 4.15) exhibit similar characteristics through the central tuna farming zone to the

north of Cape Donnington. The two variables differ in the eastern region and in the vicinity of Rabbit Island. Both variables have very similar standard error maps that vary only in magnitude but not in spatial distribution. This is due to a good spatial correlation between sites.

The isotopic signatures of δ^{13}C (Figure 4.16) and δ^{15}N (Figure 4.17) display different spatial distributions. The error map of δ^{13}C suggests a high spatial correlation between sites. This gives confidence in the prediction surface. The main features are a lighter (more negative) signature of approximately -20.5, to the north-east of Cape Donnington, peaking at station 22. This area of lighter signatures is surrounded by a heavier signature of between -18.0 and -19.5. The δ^{15}N signature exhibits a strong band of heavier isotope signatures orientated on a south-west to north-east axis starting at the southern entrance to Boston Bay and extending through the central TFZ. Apart from this band, there is also a heavy isotopic signature at station 36 located to the east of Cape Donnington.

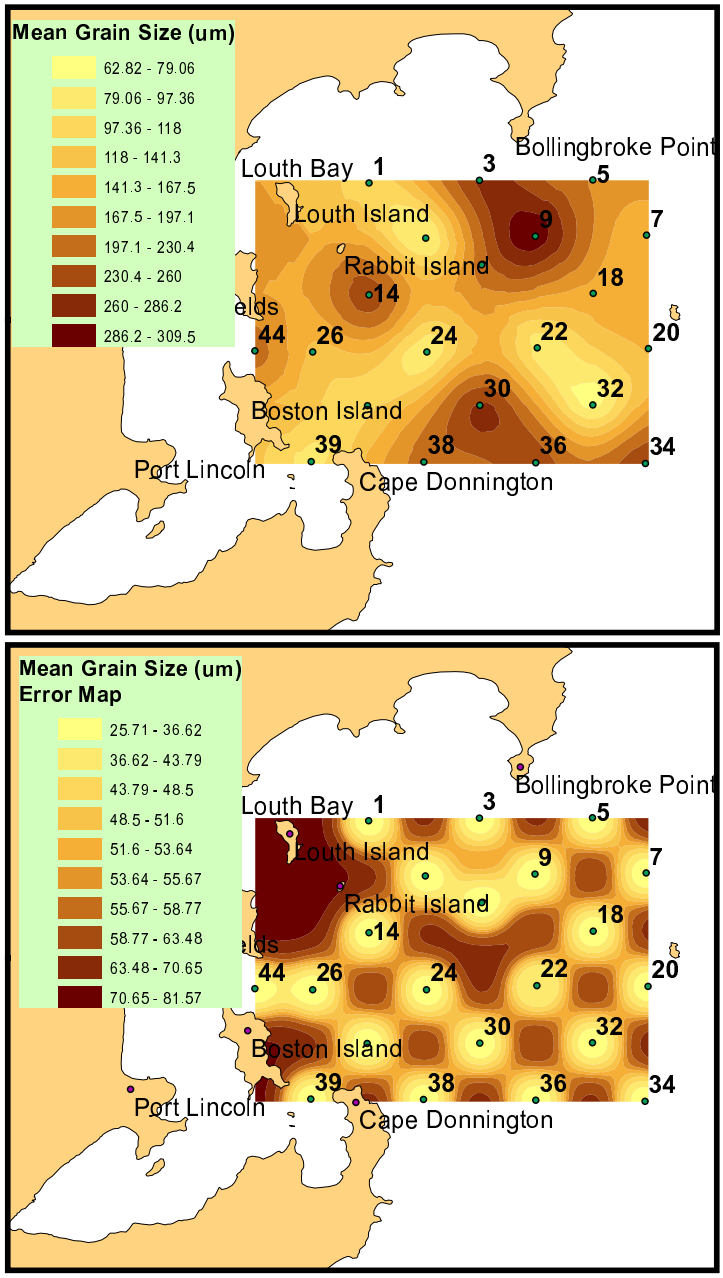

Figure 4.9: The interpolated spatial distribution of mean grain size (top) and the associate predicted standard error map (bottom).

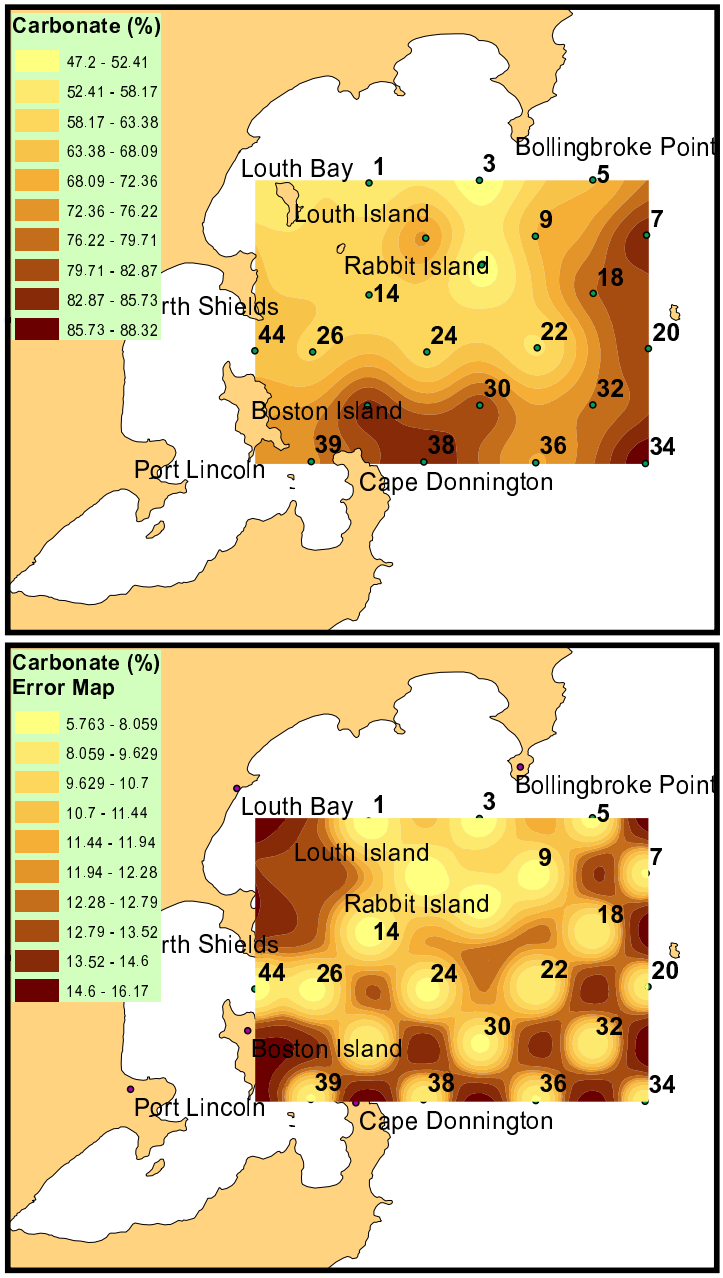

Figure 4.10: The interpolated spatial distribution of carbonate (top) and the associate predicted standard error map (bottom).

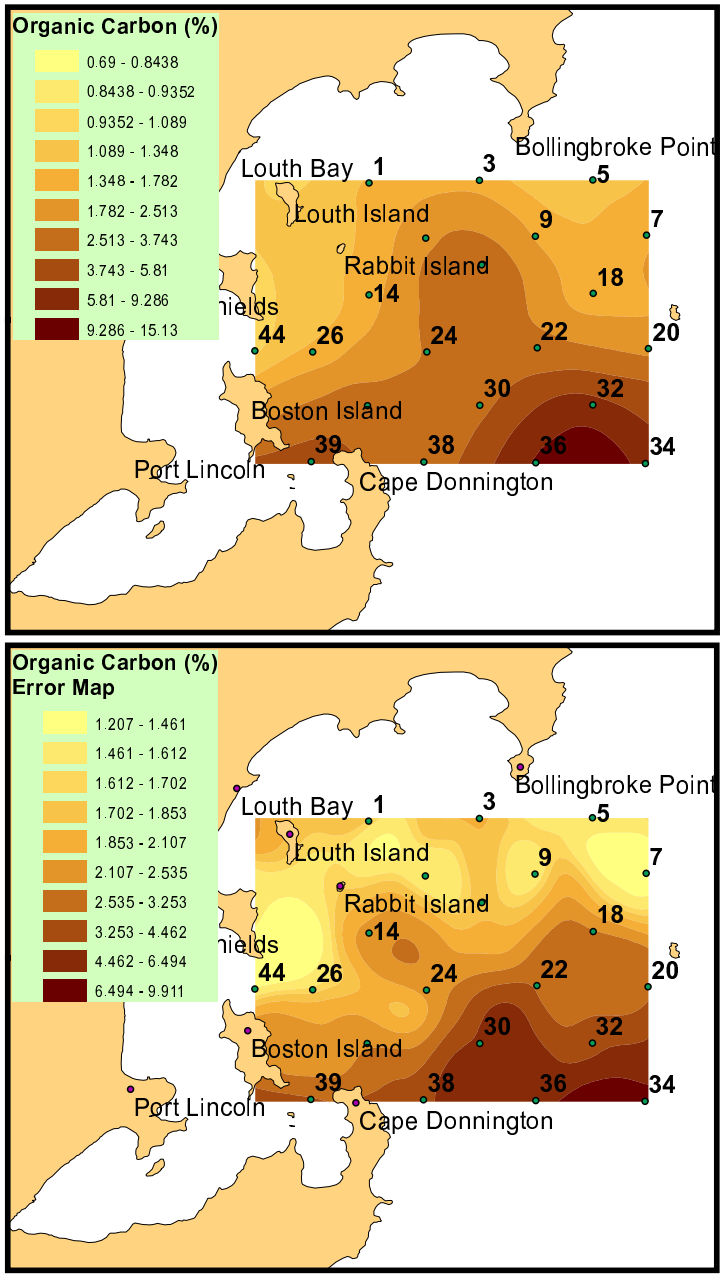

Figure 4.11: The interpolated spatial distribution of organic carbon (top) and the associate predicted standard error map (bottom).

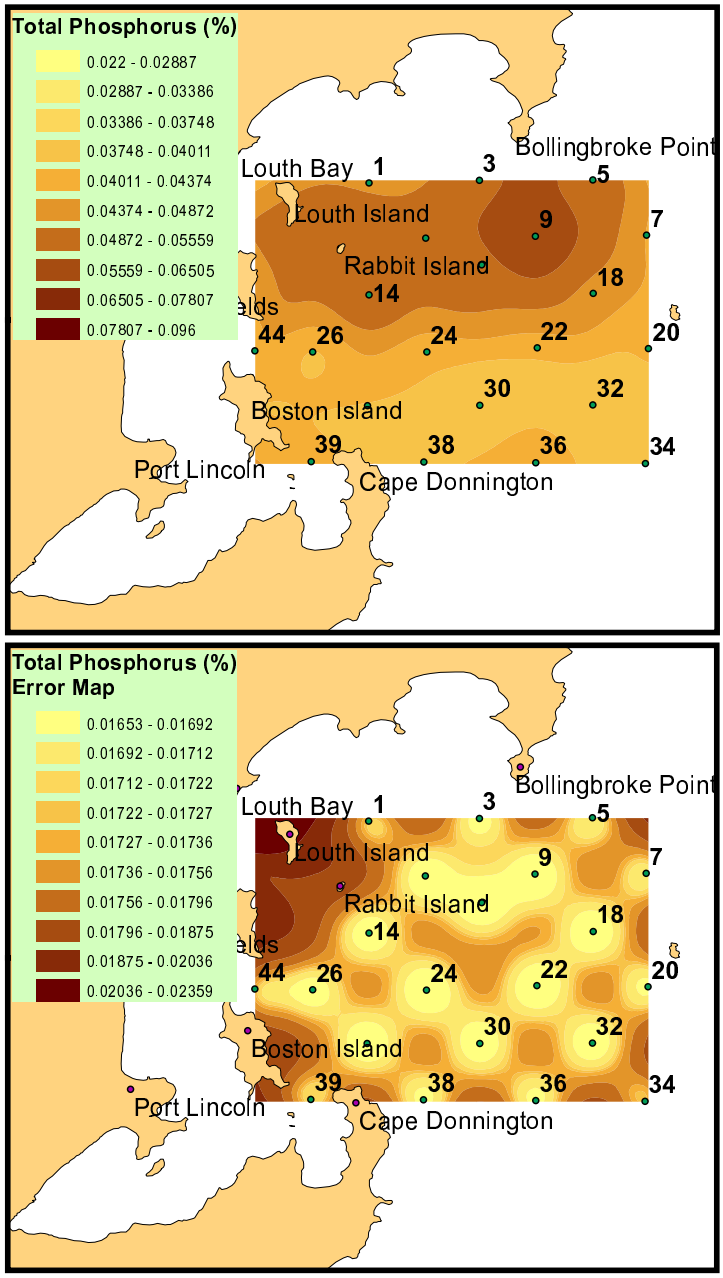

Figure 4.12: The interpolated spatial distribution of total phosphorus (top) and the associate predicted standard error map (bottom).

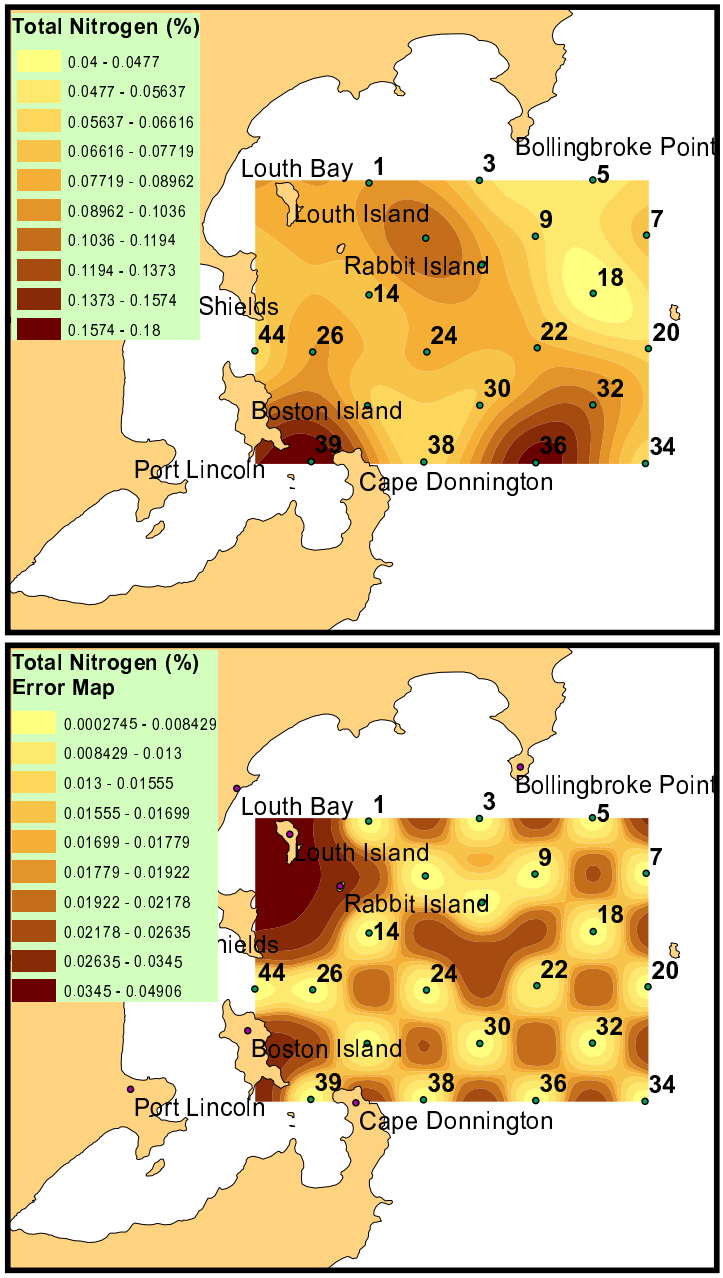

Figure 4.13: The interpolated spatial distribution of total nitrogen (top) and the associate predicted standard error map (bottom).

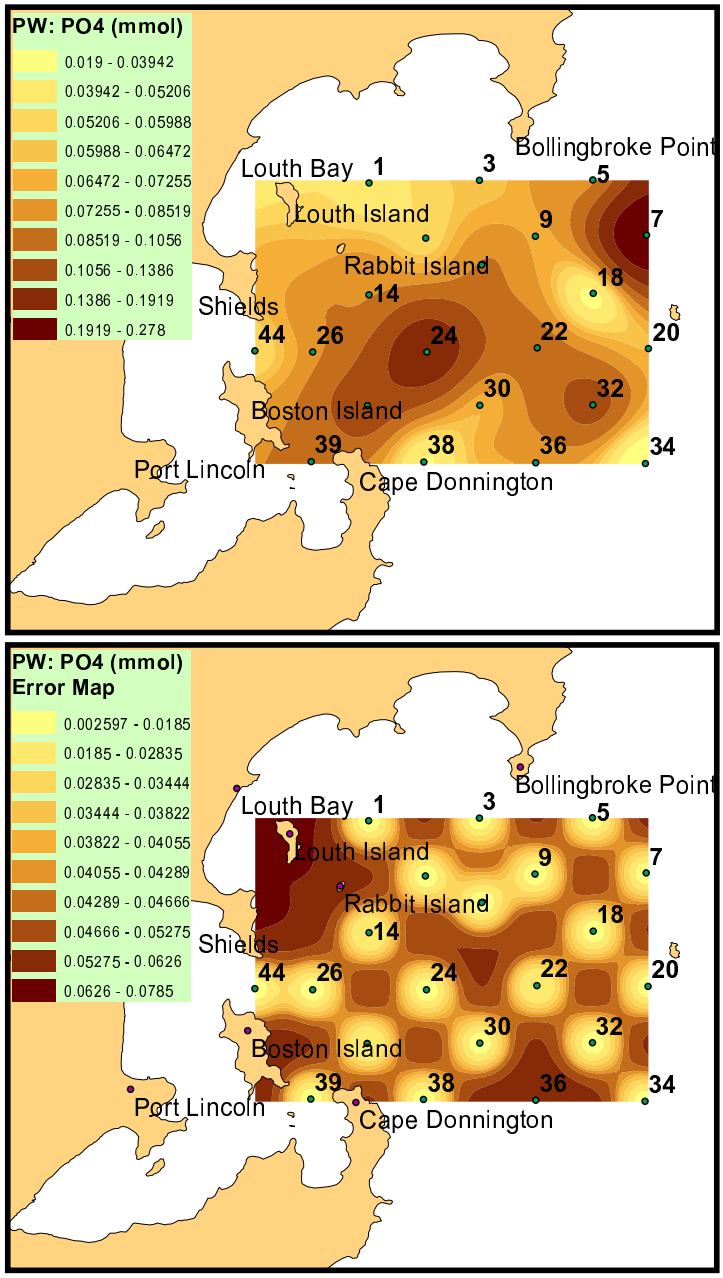

Figure 4.14: The interpolated spatial distribution of porewater phosphate (top) and the associate predicted standard error map (bottom).

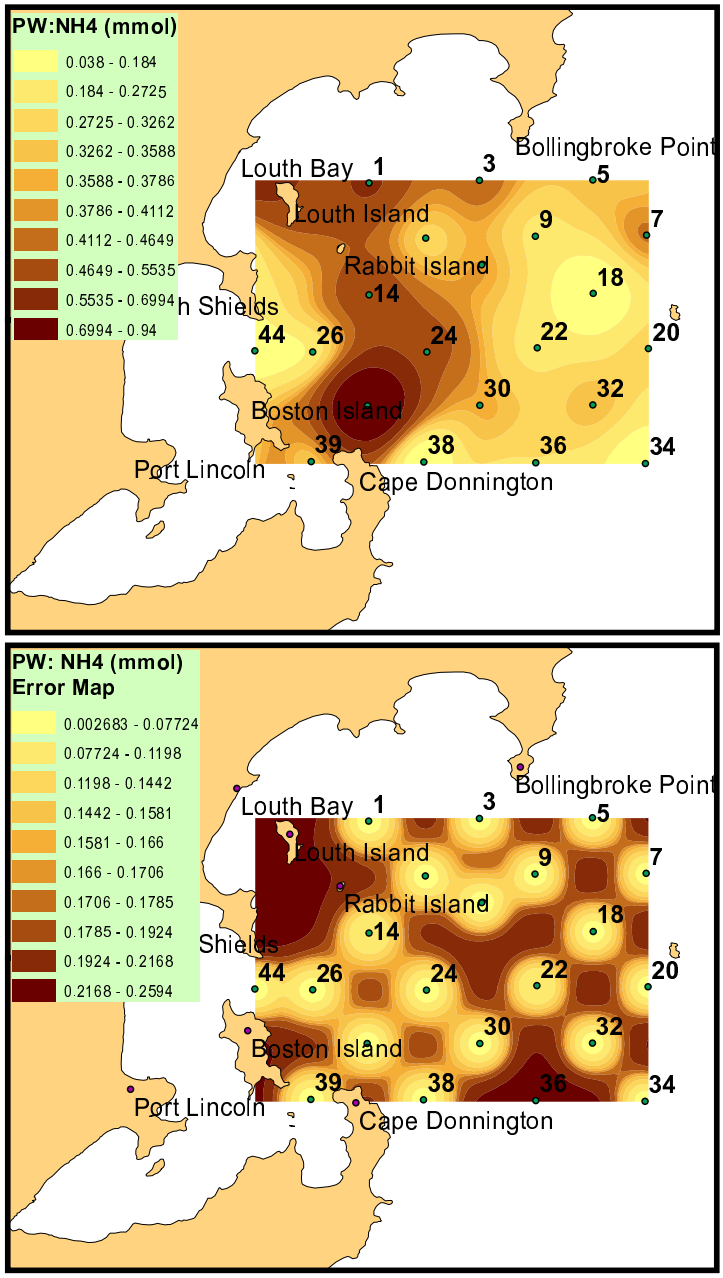

Figure 4.15: The interpolated spatial distribution of porewater ammonia (top) and the associate predicted standard error map (bottom).

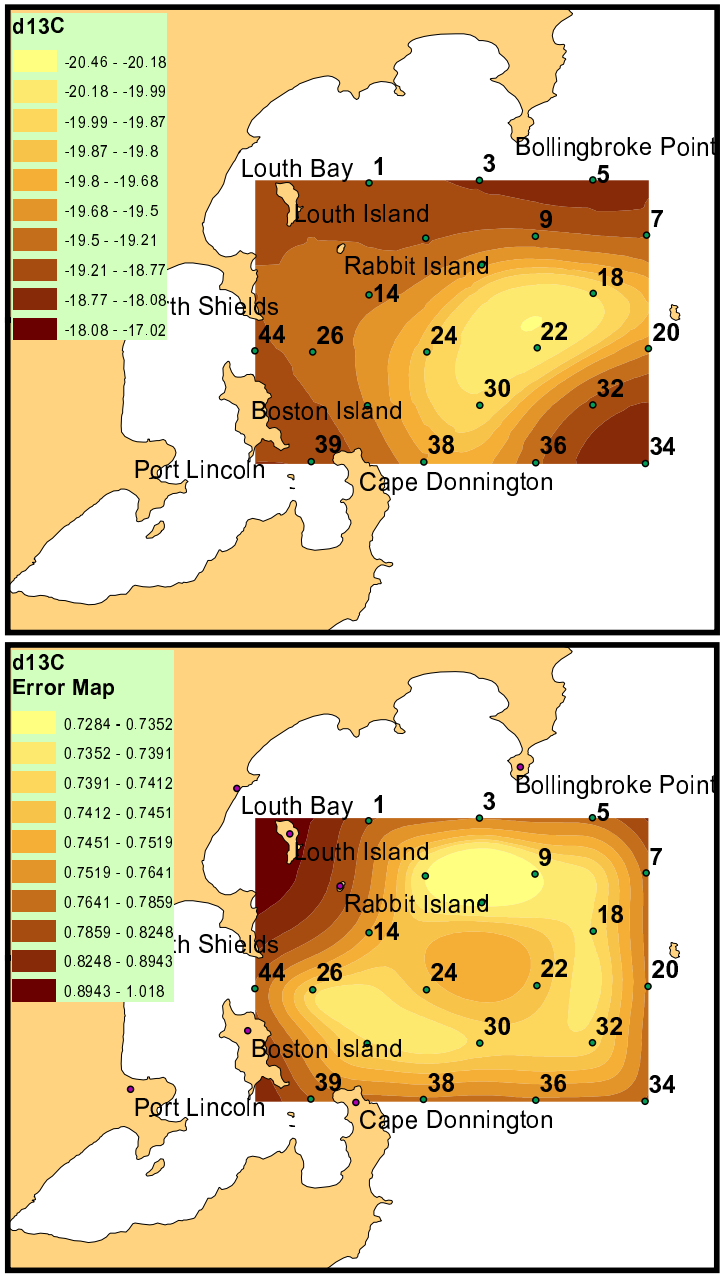

Figure 4.16: The interpolated spatial distribution of δ^{13}C (top) and the associate predicted standard error map (bottom).

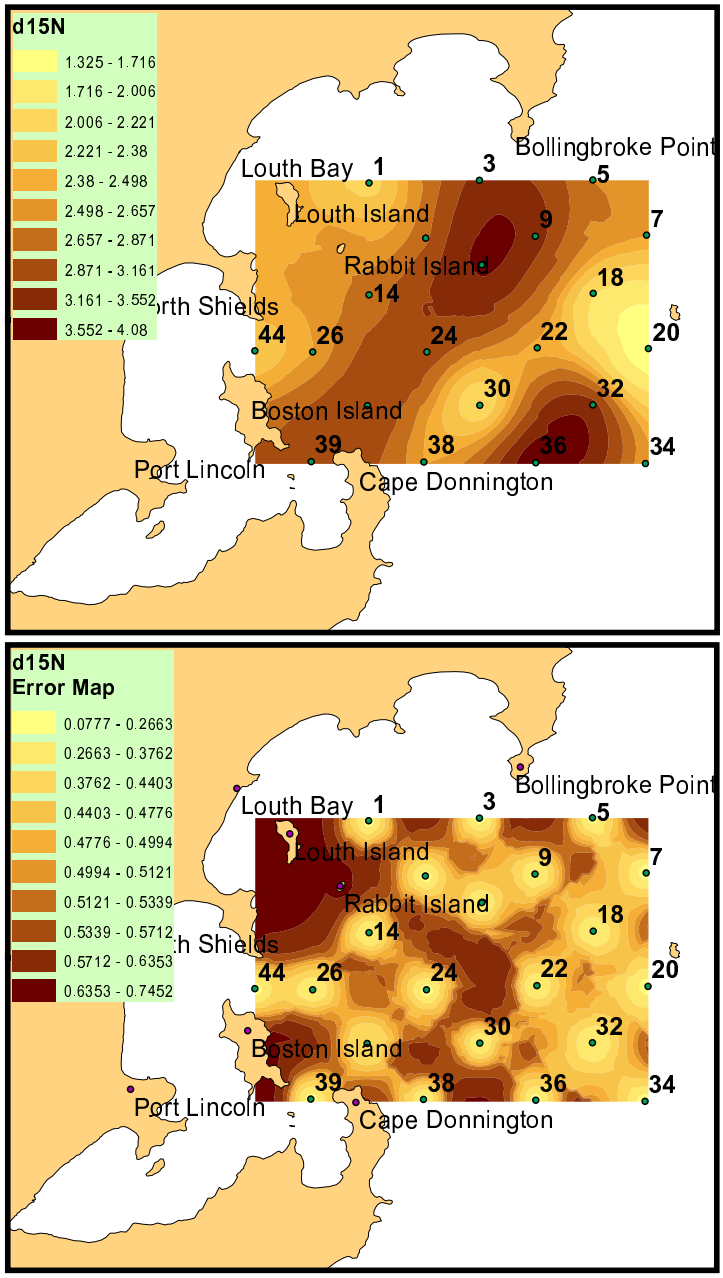

Figure 4.17: The interpolated spatial distribution of δ^{15}N (top) and the associate predicted standard error map (bottom).

4.4 Discussion

The two major sediment types identified in the cluster analysis of geochemical variables differ significantly in their textural nature, nutrient concentrations and isotopic signature. Group 2 sediments, derived from the central TFZ, have high fractions of silts. The higher fractions of fine material in Group 2 sediments are likely to originate from aquaculture activities, which is supported by the findings of sediment trap studies in Lauer (2005). As much of the tuna farming zone is located in a depositional area, the fine material, although somewhat dispersed by the tidal currents, is allowed to settle out on the seafloor. This addition of fine particulate matter leads to extremely poorly sorted sediments. The high fractions of fine material fill the interstitial spaces between the larger size fractions which reduces the permeability of the sediments. As the permeability of sediments decreases, the potential for the advective exchange of porewater nutrients with the overlying water column also decreases. The limited porewater exchange combined with higher fluxes of organic material from aquaculture activities potentially explain the richer sedimentary nutrient concentrations, typically 2-3 times the values found elsewhere in the region. This result agrees with the modelling study of Cardenas *et al.* (2008), who found the sediment biogeochemistry was affected by the sediment permeability under the influence of surface gravity waves.

The increased concentrations of nutrients in Group 2 sediments has potential implications to the aquaculture industry if these sediments were to become resuspended. The quantity of nutrients released will be dependent on the depth to which the sediments are resuspended and to what depth

advective exchange takes place in the sediments. While quantitative assessments of the depth to which resuspension takes place were not performed in Chapter 3, some studies have shown that in energetic areas, waves can cause the advective exchange of porewater nutrients to a depth of up to 50 cm in sandy sediments (Falter & Sansone, 2000). It is unlikely that these conditions will be present in the TFZ and a more realistic maximum depth of advective exchange is 5 - 10 cm. The reason for this adjustment is related to the region experiencing lower wave energy and having muddier sediments to those described in Falter & Sansone (2000).

To estimate the magnitude of the advective exchange of porewater nutrients during a resuspension event, the amount of nutrients released were plotted as a function of resuspension depth and porewater nutrient concentration (Figure 4.18).Sediments in this region have a porosity of approximately 0.35, which is typical of calcareous sands. The amount of porewater released: *Porewater released = Depth of resuspension* $\times$ *Porosity* $\times$ *Porewater Concentration.* With porewater NH_4 concentrations ranging between 0.4 and 1 mmol l^{-1} and PO_4 concentrations between 0.07 and 0.28 mmol l^{-1}, aquaculture activities located in the central tuna farming zone could expect 1.0 - 10.0 mmol m^{-2} of NH_4 and between 0.2 and 3.5 mmol of PO_4 m^{-2} to be released into the water column if the resuspension depth is between 2 - 4 cm. If this was mixed uniformly into the lower 10 m of the water column (observed resuspension events were confined to the lower 10 m of the water column, see Chapter 3), leading to concentrations between 0.1 to 1 mmol m^{-3} of NH_4 and 0.02 to 0.35 mmol of PO_4 m^{-3}. This represents an increase of up to 40% above the ambient levels of 2.5 mmol NH_4 m^{-3} and up to a 10 fold increase

above the ambient levels of 0.03 mmol PO_4 m^{-3} (personal communication). Given that the limiting nutrients in the area appear to change throughout the year (Thompson *et al.* , 2009) and that primary productivity is not limited by depth, the injection of porewater nutrients into the water column have the potential to stimulate significant levels of primary production.

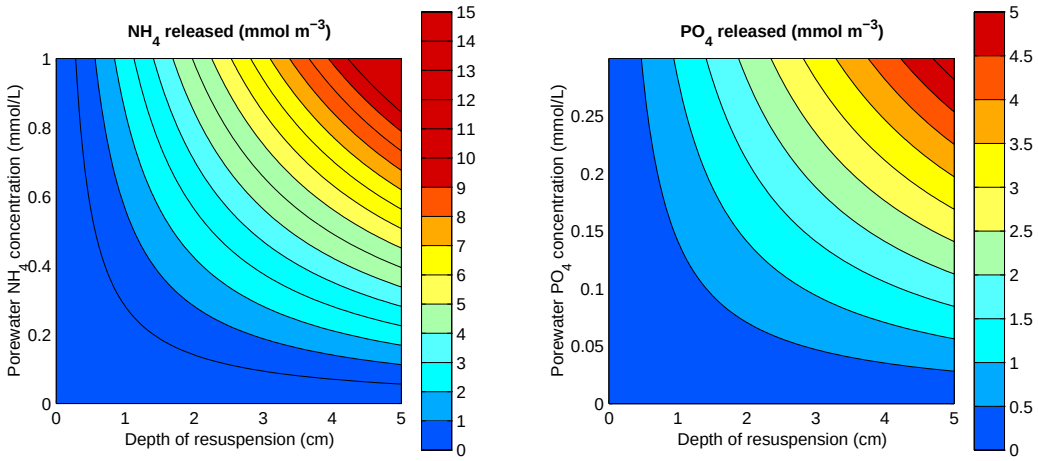

Figure 4.18: The release of porewater nutrients (mmol m^{-2}) into the water column due to sediment resuspension is shown as a function of depth of resuspension (cm) and the *in situ* porewater nutrient concentration (mmol L^{-1}) for NH_4 (left) and PO_4 (right).

The nutrient-rich region (Group 2 sediments) also has a characteristically heavier $\delta^{15}N$ isotopic signature. The heavier isotopic signature of the sediments in the central tuna farming zone suggests higher microbial activity due to the faster consumption of ^{14}N over ^{15}N (Brandes & Devol, 1997). This zone of high microbial turnover coincides with high porewater nutrient concentrations and is located in the depositional area running through the central tuna farming zone. It is likely that the high loads of organic matter originating from aquaculture activities will act to stimulate the benthic nitrogen cycling (see discussion in the following chapters). However there

does not appear to be a strong relationship between the observed geochemical distributions and the seafloor classification based on the wave regime of Chapter 3 (Table 4.3).

Table 4.3: The results of a Kruskal-Wallis non-parametric analysis of the sediment nutrient variables between the depositional and erosional zones identified in Chapter 3.

Geochemical Variable	Wave Group 1 (n=14)	Wave Group 2 (n=7)	p value
Carbonate (%)	72.5	78.6	0.1367
Organic Carbon (%)	0.72	0.90	1.0
Total Phosphorus (%)	0.04	0.05	0.6274
Total Nitrogen (%)	0.96	0.86	0.1516
PW: NH4 (μmol/L)	37.0	34.0	0.737
PW: PO4 (μmol/L)	7.1	5.0	0.1355
δ^{15}N	2.74	2.72	0.9702
δ^{13}C	-19.5	-19.3	0.94

The lack of any statistically significant difference in the geochemical composition of depositional and erosional areas suggests that the spatial distribution of geochemical variables are not only related to physical mechanisms, but possibly also the distance to sources of organic inputs (such as seagrass beds and aquaculture activities). The distance to organic matter sources is a difficult metric to include in a statistical test. This is due to the non-stationary nature of lease sites in time and space.

4.5 Conclusions

Three independent forms of cluster analysis and a MANOVA have identified two statistically different geochemical provinces in SW Spencer Gulf. There is a region that extends along a spatially coherent strip starting at the

southern entrance to Boston Bay with a major axis directed to the northeast. These sediments are far richer in nutrients, with typical concentrations approximately double those found elsewhere in the region.

There appears to be a strong relationship between the textural characteristics of the sediments and the geochemical variables. Further, the addition of fine fractions of sediments through aquaculture inputs is likely to reduce the permeability of the sediments. Consequently, the reduction in permeability limits the advective porewater exchange with the overlying water column allowing the accumulation of nutrients in both the porewaters and sediments.

If these nutrient rich sediments were to become resuspended during an energetic storm event, it is likely that the liberated porewater nutrients could increase the dissolved nutrient concentrations in the water column by a factor of between 0.4-10. This represents a major source of nutrients which could fuel primary productivity and potentially algal blooms.

Chapter 5

Denitrification: Bayesian Isotope Pairing Technique

5.1 Introduction

Recent advances in data assimilation techniques and computational power, combined with the remote sensing of ocean colour have resulted in a trend towards formal state and parameter estimation techniques within marine biogeochemical models (Harmon & Challenor, 1997; Natvik & Evensen, 2001; Dowd, 2006). A key factor in the successful application of these emerging physical-statistical models is the ability to provide realistic 'prior' information, in the form of probability distributions, for stochastic parameters, boundary and/or initial conditions within these models. The 'prior' distribution is usually constructed from previous knowledge of the system (Box & Tiao, 1992; Gelman *et al.* , 2003): one might survey the literature and derive a 'prior' from studies conducted in similar physical settings. The usual

approach is to take the mean and variance of the available data and fit a Gaussian, or other appropriate distribution; this would then be referred to as our 'informative prior'. If there had been no studies in any similar system, then an 'improper uninformative prior', usually in the form of a uniform distribution on a pre-defined interval, would be prescribed. By combining the 'prior' information with observational data through a data assimilation routine, the model state and stochastic parameters can be constrained to form a 'posterior' distribution.

In coastal marine biogeochemical models, a key process is the sedimentary denitrification rate, which acts as a loss term for dissolved inorganic nitrate. Denitrification permanently removes inorganic nitrogen from an ecosystem, thus counteracting the effects of enhanced nitrogen inputs (Libes, 1992; Eyre *et al.* , 2002). Denitrification is the reduction of NO_3^- and NO_2^- to N_2 and is often coupled to the reduction of Fe and S species (Codispoti *et al.* , 2001; Hulth *et al.* , 2005). The enzymes responsible for denitrification (nitrogenase) are inhibited by oxygen at concentrations greater than 5 μM (Codispoti *et al.* , 2001; Sigman *et al.* , 2003). In regions where the O_2 consumption rate is high enough to cause anaerobiosis, denitrification frequently occurs (Knowles, 1982). Denitrification is therefore constrained to areas within the water column and sediment horizons that are nearly anoxic in nature. The benthic nitrification/denitrification cycle is assumed to follow a strict vertical regime in which nitrification takes place in the oxic portion of the sediment that overlies anoxic portions where denitrification takes place. Accordingly, this coupled process is governed by the vertical advective/diffusive flux of nitrate and nitrite from oxic to anoxic layers (Hulth *et al.* , 2005).

Past marine denitrification studies have covered a diverse range of environments from estuaries and lakes through to the deep ocean, but to the best of my knowledge none have formed probability distributions for *in situ* denitrification rates. While many of the classic denitrification papers reviewed in Steingruber *et al.* (2001) give estimates of the mean and/or range of denitrification rates, there appears to be little or no information that could adequately prescribe a well constrained 'prior' probability distribution for sedimentary denitrification rates. This may have arisen due to a number of factors, ranging from study site locations, through to the lack of any statistically rigorous method to account for small-scale variability that may be present in the sediments.

Denitrification represents an important process in the nitrogen cycle in coastal marine ecosystems. Methods to estimate sedimentary denitrification rates can be classified as either direct or indirect. A direct method measures the flux of dinitrogen gas produced by the denitrification process, whereas indirect methods infer the denitrification rate from stoichiometric relationships. Two of the most common direct measurement techniques are the Isotope Pairing Technique (IPT) pioneered by Nielsen (1992a) and the N_2:Ar technique. A comparison between the techniques is presented in Eyre *et al.* (2002). The IPT technique can underestimate denitrification rates in oligotrophic regions where heterogeneous sediments are present (Ferguson & Eyre, 2007). Other *in situ* methods involve benthic flux chambers that measure the flux of N_2 from the sediments (Heggie *et al.* , 1999).

An example of an indirect technique is the inferred Net Denitrification (ND) rate calculated from the dissolved inorganic nitrogen (DIN) and dis-

solved inorganic phosphate (DIP) fluxes from the sediments, following the methods of Yamamoto *et al.* (2008) (see Chapter 6). The direct and indirect methods both require intact sediment cores to be taken. Accordingly, both are susceptible to errors associated with sampling and the effects of spatial variability.

The review paper of Steingruber *et al.* (2001) found that typical denitrification rates in coastal sediments range from 0.0 to 80.0 μmol m^{-2} h^{-1}, depending on the geochemistry and nutrient loads entering the system. Many of the reviewed studies were conducted in cohesive sediments with low porewater flushing and sited in relatively sheltered areas. In contrast the geochemistry and related microbial communities of permeable sediments, often exhibit substantial spatial variability over short length scales (0.1-1.0 m) (Precht & Huettel, 2003). An example is the oscillatory flow generated by surface gravity waves, which can flush porewater nutrients from the crests of sand ripples while leaving the porewater nutrients largely unaffected at the ripple base (Cardenas *et al.* , 2008). Traditional techniques to measure the denitrification rates in these regions do not explicitly account for the spatial variability often found in coastal sediments.

The region used for this study is located near Port Lincoln in South Australia (Figure 5.1). The area to the east of Boston Island is used intensively for finfish aquaculture and is hereon referred to as the tuna farming zone. During the Austral summer, southern bluefin tuna are caught on the adjacent continental shelf and are transported live back to the tuna farming zone for a value-adding process. The tuna are held in pontoons and fed a diet of locally-caught pilchards. Approximately 90% of the nitrogen derived

from the metabolism of tuna feed is released into the water column as either particulate or dissolved matter (Fernandes *et al.* , 2007b). The benthic metabolism adjacent to tuna aquaculture sites is far higher than the sites unaffected by aquaculture activities (Lauer, 2005). There have been no studies that examine the *in situ* sedimentary denitrification rates to quantify the loss of bio-available nitrogen from the system.

The sediments in the tuna farming zone are characterised as poorly sorted carbonate sands (see Chapter 4) being influenced by the inherent hydrodynamics of the site, which reflects a combination of locally-generated wind waves, swell from the Southern Ocean (Chapter 2), and lower-frequency tidal currents (Herzfeld *et al.* , 2009). This combination of textural characteristics and hydrodynamics suggests that the sediments are permeable and that the porewater can be subjected to advective exchange with the overlying water column. Modelling studies by Huettel *et al.* (2003) examined the effect of hydrodynamics on sediment biogeochemistry in a range of permeabilities and found that the regions where denitrification can take place can become very heterogeneous. Although traditional techniques of measuring denitrification (e.g. Nielsen (1992a); Cornwell *et al.* (1999)), cannot estimate spatial variability it is possible to explicitly take into account the effects of small-scale variability by using a Bayesian approach.

This chapter addresses the following issues:

1. The underlying assumptions of the IPT technique are validated for the study region.

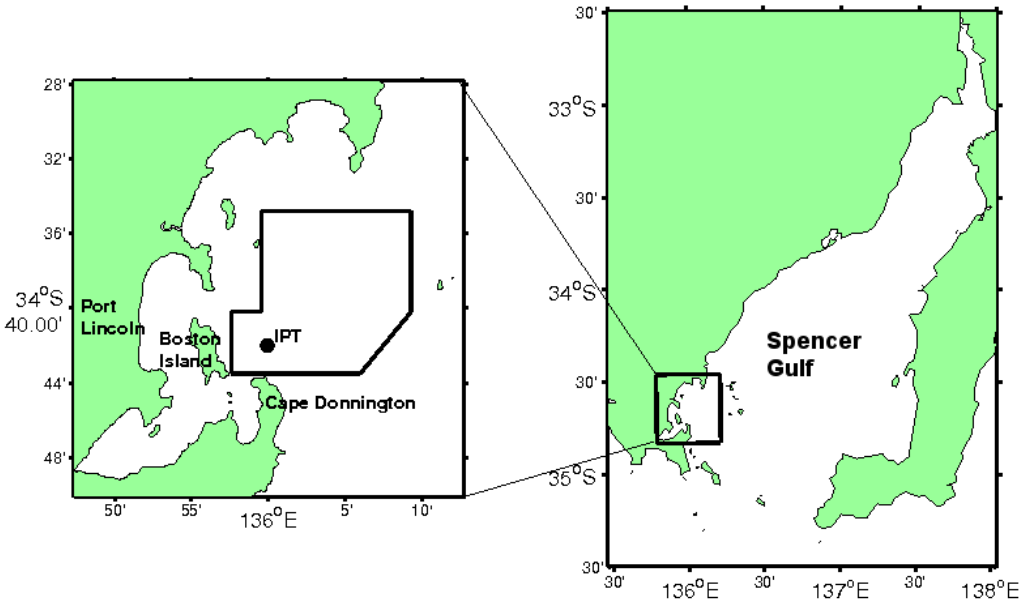

Figure 5.1: Map of the study region, showing the sampling site (IPT) and the boundary of the tuna farming zone.

2. Both standard and Bayesian methods are compared for the determination of the coupled sedimentary nitrification-denitrification rates.

3. The underlying physical conditions that influence the sedimentary biogeochemistry and the *in situ* denitrification rates are examined.

5.2 Materials and methods

Table 5.1: List of symbols and abbreviations used in this chapter.

Symbol	Description	Units
IPT	Isotope Pairing Technique	-
B-IPT	Bayesian Isotope Pairing Technique	
ND	Net Denitrification	μmol m^{-2} hr^{-1}
DIN	Dissolved Inorganic Nitrogen Flux	μmol m^{-2} hr^{-1}
DIP	Dissolved Inorganic Phosphate Flux	μmol m^{-2} hr^{-1}
$^{xx}N_2$	Stable Isotope of Di-nitrogen gas	-
$^{xx}N_2O$	Stable Isotope of nitrous oxide gas	-
^{xx}PR	Production Rate of a stable isotope	μmol m^{-2} hr^{-1}
D_{14}	The denitrification of the *in situ* $^{14}NO_3^-$	μmol m^{-2} hr^{-1}
D_{15}	The denitrification of the *in situ* $^{15}NO_3^-$	μmol m^{-2} hr^{-1}
D_{tot}	The total denitrification rate	μmol m^{-2} hr^{-1}
$D_{w,tot}$	The total denitrification rate from overlying water	μmol m^{-2} hr^{-1}
D_n	The coupled sedimentary nitrification/denitrification	μmol m^{-2} hr^{-1}
D_w	Denitrification from overlying water	μmol m^{-2} hr^{-1}
ϵ	Enrichment factor	-
UHP	Analytical grade Helium	-
GC-IRMS	Gas Chromatograph Isotope Ratio Mass Spectrometer	-

5.2.1 Study site and sampling procedures

Four time-series incubations using a slightly modified version of the popular IPT technique were undertaken using sediment cores taken at a site located in 22 m of water within the aquaculture zone near Pt Lincoln in South Australia (Figure 5.1). The area is characterised as very poorly sorted calcareous sediments with a carbonate ($CaCO_3$) content $> 80\%$. Sediment cores were collected with PVC tubes (10.5 cm in diameter and 30 cm long) by commercial divers within an area of 1 m^2 to limit the effect of large scale spatial variability. For each time-series incubation, the divers collected eight cores

to a depth of approximately 10 cm. Lids with rubber O-rings were placed on the cores and screwed down tightly. The cores were then extracted gently from the sediments, remaining vertical at all times. PVC caps were placed on the underside of the tubes, which were placed in a basket for retrieval. Once all cores were collected, the basket was recovered using the crane on the boat. The diver returned to the surface with the basket to prevent it from over turning while being lifted through the water column. All cores were checked for the clarity of the overlying water, which indicated that the core was undisturbed. Eighty litres of site water from 22 m depth was also collected using a water sampler. The cores and site water were then returned to the laboratory for incubation within 2 hours of collection. The *in situ* dissolved oxygen (DO) content and temperature were recorded from the site water upon collection.

5.2.2 Incubation procedure

The procedure used in this study is very similar to that published by Nielsen *et al.* (2000), with a few minor modifications. At the laboratory, 65 litres of site water was transferred into an opaque polycarbonate tank that sits in an ice bath. The cores were transferred to the tank and the lids removed. The site water was circulated through the tank and an aquarium heater maintained the temperature of the tank at the site temperature. Three replicates of tank water were collected for nutrient and isotopic analysis. The stable isotope of nitrogen, ^{14}N, exists as 99.634% by atoms compared to ^{15}N 0.366% (Karl *et al.* , 2002). $^{15}NO_3^-$ was then added to the tank water in the

form of $K^{15}NO_3$ (98 atom%), which when denitrified, lead to the enrichment of the $^{29}N_2$ and $^{30}N_2$ pools, giving a direct measurement of the denitrification rate. Three replicates of tank water were then taken for nutrient and isotopic analysis; these values were used to calculate the enrichment factor (ϵ) of the overlying water (see below).

The cores were left to preincubate for a period of 12 hours. It was determined from previous (unpublished) experiments that the preincubation was required for homogenous labelling of the sediments. After the 12 hour preincubation, three more replicates of tank water were taken for nutrient and isotopic analysis. Two cores were then sacrificed at the beginning of each incubation series and then one every hour thereafter for five hours or when the DO content dropped below 20% of the initial value. Cores to be incubated were capped with a PVC lid with a double O-ring seal and a magnetic stirrer was inserted into a port in the lid to prevent stratification. The incubation start time was set when the cores were capped.

The sacrificial procedure adheres to the following series of actions:

1. The time was noted and the lid of the core was removed,

2. Two replicate water samples were taken for nutrient analysis,

3. 1 ml of 50% w/v $ZnCl_2$ was added to the core to cease any microbial activity,

4. The sediment was stirred to a depth of 5 cm for a period of one minute, taking care not to create any bubbles. The slurry was allowed to settle for 2 minutes to allow the large particles to settle out,

5. Six replicate water samples were taken from the core with a 12 ml syringe with approximately 10 cm of silastic tubing on the end. The water was drawn very gently into the syringe and transferred into 12 ml Exetainers, taking care not to introduce atmospheric gas bubbles,

6. 0.2 ml of 50% w/v $ZnCl_2$ was added to each of the Exetainers. The Exetainers were capped and checked to make sure no atmospheric gases were trapped as bubbles in the containers,

7. The samples were stored in the dark at 4°C awaiting isotopic analysis.

5.2.3 Isotopic analysis

The isotopic analysis was carried out using a Sercon Gas Chromatograph Isotope Ratio Mass Spectrometer (GC-IRMS), located at the CSIRO Land and Water Laboratories at Urrbrae in South Australia. Isotopic analysis on both N_2 and N_2O was undertaken. In this study we only make use of the N_2 results. The IRMS was calibrated using a number of references. A specialty reference gas containing 2 ppm of N_2O and 1.5%N_2 along with four different concentrations of air diluted in He and also blanks filled with ultra high purity (UHP) He were passed though the IRMS before and after each run of samples. The response for each of the charge ratios for m/z $^{28}N_2$, $^{29}N_2$, $^{30}N_2$, $^{44}N_2O$, $^{45}N_2O$ and $^{46}N_2O$ was found to be linear over the expected experimental range. By using different concentrations of the various gas species, we could correct for any sensor drift over the batch run. For the analysis of both N_2 and N_2O, a 4 ml head space of UHP He was introduced into the Exetainers using a 2-way valve and a syringe (Nielsen *et al.* , 2000).

The Exetainers were then placed in an autosampler connected to the GC-IRMS. A 2 way syringe was used to bubble UHP He through each of the vials, referred to as sparging (personal communication, Mark Trimmer). Previous tests showed this method degassed greater than 99% of the dissolved N_2 and N_2O from the water sample. While the UHP He was bubbling through the water sample, the headspace was being continually swept into the GC-IRMS. The gas sample passed through a magnesium perchlorate trap to remove any water vapour from the sample, it then progressed into a Carbosorb then Shutze reagent trap to remove CO_2 and CO respectively. At this stage the sample was split, 50 μl was captured for N_2 analysis and the remainder of the sample progressed through the system for N_2O analysis. At no point did either sample pass through a copper reduction column. Due to the double cryo-focussing step, the isotopic analysis for each sample takes approximately 20 minutes. The N_2O data is not considered further in this study.

5.2.4 Direct method: Isotope Pairing Technique

The calculation of the denitrification rates based on the method of Nielsen (1992a) are formulated from the production rates of $^{29}N_2$ (^{29}PR) and $^{30}N_2$ (^{30}PR) with units of μmol m^{-2} h^{-1}. The denitrification of the added $^{15}NO_3^-$ (D_{15}), is given by:

$$D_{15} =^{29} PR + 2\,^{30}PR \tag{5.1}$$

The denitrification of the *in situ* $^{14}NO_3^-$ is:

$$D_{14} = D_{15}\frac{^{29}PR}{2\ ^{30}PR} \tag{5.2}$$

The total denitrification rate within the incubation chamber is:

$$D_{tot} = D_{14} + D_{15} \tag{5.3}$$

The total denitrification rate derived from the diffusion of $^{15}NO_3^-$ in the overlying water into the denitrification zone is:

$$D_{tot,w} = \frac{D_{tot}}{\epsilon} \tag{5.4}$$

Where ϵ is the enrichment of *in situ* NO_3^- defined by:

$$\epsilon = \frac{[^{15}NO_3^-]}{[^{14}NO_3^-] + [^{15}NO_3^-]} \tag{5.5}$$

The denitrification rate in the sediments from nitrate produced in the nitrification zone is given by:

$$D_n = D_{tot} - D_{tot,w} \tag{5.6}$$

And the *in situ* denitrification rate caused by the diffusion of *in situ* $^{14}NO_3^-$ from the overlying water column into the sediments is calculated by:

$$D_w = D_{tot,w}(1 - \epsilon) \tag{5.7}$$

There are 4 underlying assumptions that the Isotope Pairing Technique (IPT) relies on (Nielsen *et al.* , 2000):

1. A stable NO_3^- gradient across the sediment-water interface. This assumption can be tested through a linear increase of labeled N_2 in the chamber with time.

2. The addition of $^{15}NO_3^-$ does not interfere with the denitrification of *in situ* NO_3^-. The assumption can be tested by adding different concentration of $^{15}NO_3^-$ to the overlying water column. If the denitrification rate does not change with concentration then this assumption can be treated as valid.

3. The labelling of the sedimentary $^{14}NO_3^-$ with $^{15}NO_3^-$ must be homogeneous throughout the sediment layer. Usually achieved via a pre-incubation period to allow the $^{15}NO_3^-$ to diffuse into the sediment, which is typically validated through a linear increase in labeled N_2 in the chamber with time. Further work is being done on this assumption as high resolution profiling of sediment horizons become possible with the new generation of micro-sensors.

4. The portion of the denitrification rate that is derived from the water column should increase linearly with increased concentration of $^{15}NO_3^-$. This assumption can also be tested by adding different concentrations of $^{15}NO_3^-$.

Each of these assumptions are dealt with individually in the results section. The production rates of $^{29}N_2$ and $^{30}N_2$ are traditionally calculated by applying a Least Squares Linear Regression (LSLR) to the measured quantities of $^{29}N_2$ and $^{30}N_2$ with time. This approach works well if there is very

little scatter about the line of best fit. However, in permeable sediments it is possible that the effects of spatial variability in microbial communities can lead to significant scatter about this line. If this is the case, in the presence of only 5 to 6 data points, the Gaussian assumptions of the LSLR are prone to significantly overestimate the 95% confidence interval, and potentially miscalculate the slope. An alternative to the LSLR is Bayesian Linear regression (BLR), which does not rely on the same parametric assumptions as the LSLR (Gelman *et al.* , 2003).

Bayesian Linear Regression

The measured amounts of $^{29}N_2$ and $^{30}N_2$, with units of μmol m^{-3}, contained in each of the incubation chambers, are the foundations of the IPT. The typical approach is to apply a first order linear regression with respect to time to estimate the slope of the line that passes through (or close to) measured amounts of $^{29}N_2$ and $^{30}N_2$ and the y-intercept (b). The slopes of these lines are the production rates (PR) used in the IPT calculations. If there is very little variability between the cores, all the points should fall on or very near the straight line. If there is scatter about the line, which we assume is derived from spatial variability, then the parametric assumptions of linear regression can lead to errors in estimating not just the slope but also the confidence intervals of the slope. Spatial variability has been parameterised by τ

The relationship between the observations ($N_2(t)_{observed}$), PR, b and τ can be written as a conditional probability distribution, referred to as the posterior:

$$P[PR, b, \tau | N_2(t)_{observed}] \tag{5.8}$$

Which reads, 'The probability of PR, b and τ conditional on $\mathrm{N}_2(t)_{observed}$'.

The Bayesian statistical methods we have used are adapted from Gelman *et al.* (2003) and Gamerman & Lopes (2006). An introduction to this method and a proof of concept is contained in Appendix A and an example R script is contained in Appendix B. The advent of contemporary Markov Chain Monte Carlo (MCMC) techniques have led to a diverse range of algorithms that can be used within the broad field of Bayesian inference. We have applied a form of BLR using a Metropolis-Hastings Markov Chain Monte Carlo (M-H MCMC) simulation to approximate the distributions for the production rates of $^{29}\mathrm{N}_2$ and $^{30}\mathrm{N}_2$. The distributions of the production rates of $^{29}\mathrm{N}_2$ and $^{30}\mathrm{N}_2$ are then propagated through the conventional IPT calculations yielding distributions for D_n and D_w. We hereinafter refer to this method as the Bayesian-IPT (B-IPT). It is anticipated that the information contained in the distributions of D_n and D_w could be used as the prior distributions for denitrification rates in emerging biophysical-statistical ecosystem models.

5.3 Results

The production rates of $^{29}N_2$ and $^{30}N_2$ are presented first as these results are the foundations for the IPT calculations. The discrete distributions are then propagated through the IPT calculations to form discrete distributions for D_n and D_w. It is at this point that the results can be used to validate the underlying assumption of the IPT method. The observed denitrification rates are then discussed.

5.3.1 *In situ* production rates of $^{29}N_2$ and $^{30}N_2$

The application of the BLR yield distributions for ^{29}PR and ^{30}PR (Figure 5.2) and comparisons with the LSLR methods are detailed in Tables 5.2 and 5.3. The two methods gave very similar results with the exception of ^{30}PR in the incubation where $\epsilon = 0.98$. The disparity is largely associated with the scatter in this incubation. The 95% confidence interval predicted by the LSLR is nearly 25% greater than that predicted by the BLR method. The variability seen this these production rates are directly attributed to the small-scale spatial variability within an area of approximately 1 m^2.

Table 5.2: Production rates of $^{29}N_2$ in μmol m^{-2} h^{-1} (^{29}PR), estimated used LSLR and BLR. The results of the BLR are denoted in **bold**, LSLR are within the brackets.

	ϵ= **0.94**	ϵ= **0.95**	ϵ= **0.97**	ϵ= **0.98**
Mean	**1.72** (1.66)	**1.08** (1.08)	**4.78** (4.85)	**3.57** (3.56)
Median	**1.68** (-)	**1.08** (-)	**4.82** (-)	**3.57** (-)
2.5%	**0.33** (-0.39)	**0.79** (0.80)	**2.41** (2.11)	**2.25** (2.19)
97.5%	**3.47** (3.72)	**1.37** (1.37)	**6.74** (7.60)	**4.93** (4.93)
$\mathbf{R^2}$	**-** (0.67)	**-** (0.98)	**-** (0.97)	**-** (0.96)

Table 5.3: Production rates of $^{30}N_2$ in μmol m^{-2} h^{-1} (^{30}PR), estimated used LSLR and BLR. The results of the BLR are denoted in **bold**, LSLR are within the brackets.

	ϵ= **0.94**	ϵ= **0.95**	ϵ= **0.97**	ϵ= **0.98**
Mean	**6.19** (5.85)	**0.87** (0.85)	**10.00** (10.01)	**3.46** (2.16)
Median	**5.98** (-)	**0.86** (-)	**10.00** (-)	**3.02** (-)
2.5%	**0.993** (-2.42)	**0.23** (0.03)	**8.94** (8.81)	**0.19** (-6.75)
97.5%	**12.88** (14.12)	**1.63** (1.66)	**11.00** (11.21)	**9.4** (11.06)
R^2	**-** (0.63)	**-** (0.78)	**-** (1.00)	**-** (0.17)

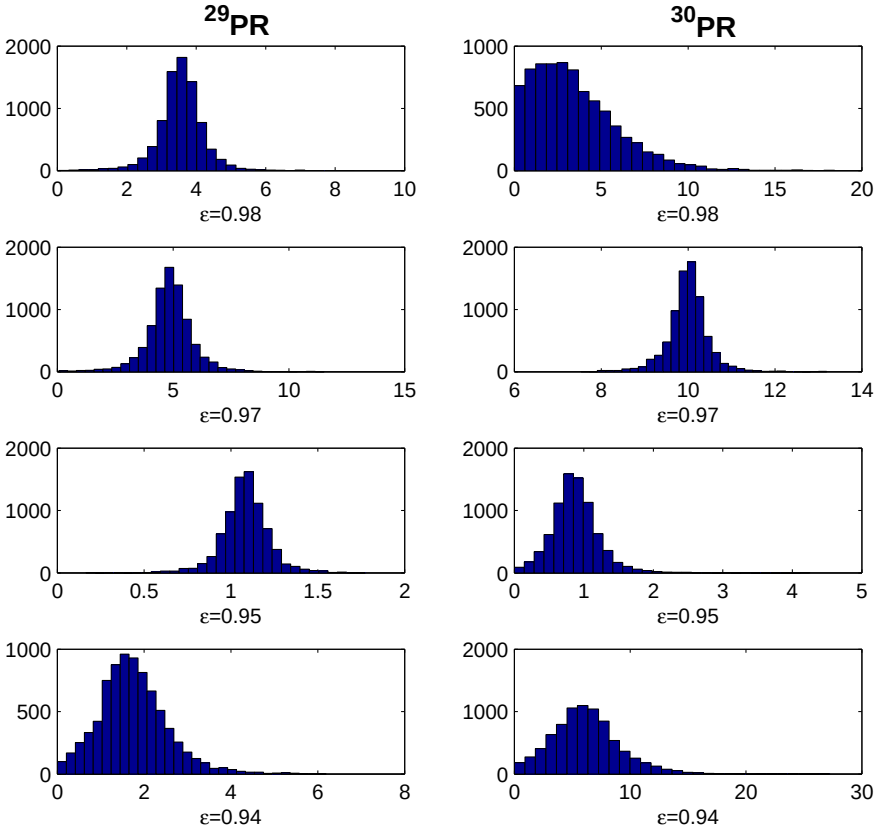

Figure 5.2: Histograms of ^{29}PR (left) and ^{30}PR (right) for each of the four incubation runs.

5.3.2 Validation of assumptions

Four underlying assumptions of the IPT technique must be validated to ensure the effects of processes such as the anaerobic oxidation of ammonia via nitrate (Anammox) (Trimmer *et al.* , 2006) do not impact upon the denitrification rate calculations. Briefly they are:

1. A stable $^{15}NO_3^-$ gradient across the sediment/water interface.
2. The addition of $^{15}NO_3^-$ does not interfere with the *in situ* denitrification rate of $^{14}NO_3^-$.
3. The labelling of the *in situ* $^{14}NO_3^-$ with $^{15}NO_3^-$ must be homogeneous.
4. $D_{tot,w}$ must increase linearly as a function of $^{15}NO_3^-$ concentration in the overlying water.

In order to validate these assumptions the production rates of $^{29}N_2$ and $^{30}N_2$ were measured using four time-series experiments conducted at increasing concentrations of $^{15}NO_3^-$ in the overlying water.

Due to the very low concentrations of *in situ* $^{14}NO_3^-$ (0.4 - 2.5, μM) even modest additions of labeled nitrate gave values of ϵ in the range of 0.94 to 0.98. We have therefore not been able to generate the large spread in enrichment factors reported in other studies.

Assumptions 1 and 3 are validated by a linear increase of $^{29}N_2$ and $^{30}N_2$ with respect to time in each of the cores. In all of the experiments, the production of $^{29}N_2$ and $^{30}N_2$ in each of the chambers increased linearly with time (Tables 5.2 and 5.3). The production of $^{29}N_2$ appeared to show less variability (higher R^2 values) than those of $^{30}N_2$. Due to highly enriched

nutrient concentrations, the production rates of $^{30}N_2$ are likely to have been more sensitive to spatial variability in the microbial community structure (see section 5.4).

To validate assumption 2, there should be no evident relationship between ϵ and D_n. A cursory examination of the relationship between ϵ and D_n suggests a weak positive linear relationship (Figure 5.3). However, due to the wide credibility intervals and very small spread in enrichment ratios, this results holds no statistical significance.

Assumption 4 implies a linear relationship between ϵ and $D_{tot,w}$. This assumption was also difficult to validate due to the narrow range of enrichment ratios. The denitrification rate of the labeled $^{15}NO_3^-$ increased minimally over the narrow range tested.

5.3.3 Denitrification rates

This is the first study to have applied the B-IPT approach to estimate the small scale variability in D_n and D_w. Distributions for D_n and D_w were generated using the traditional IPT calculations applied to each realised pair of ^{29}PR and ^{29}PR. The median values of the B-IPT distributions, were nearly identical to those of the traditional LSLR IPT. The 95% credibility intervals for the D_n rates in the four time-series experiments ranged from 0.5 through to nearly 25 μmol m^{-2} h^{-1} and the denitrification derived from the water column was an order of magnitude smaller at between 0.12 and 2.5 μmol m^{-2} h^{-1}. The histograms of the distributions of D_n and D_w rates are distinctly non-normal in shape and appear to follow a log-normal distribution

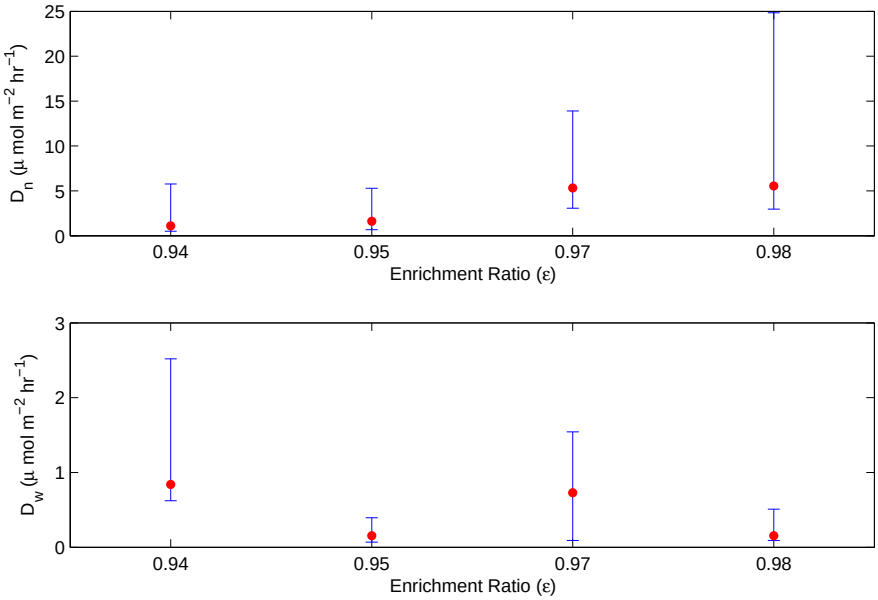

Figure 5.3: The median (red marker) and 95% credibility interval (blue bars) for the coupled nitrification/denitrification (upper panel) and denitrification derived from dissolved NO_3^- from the water column (lower panel) using B-IPT at different values of ϵ.

(Figure 5.4).

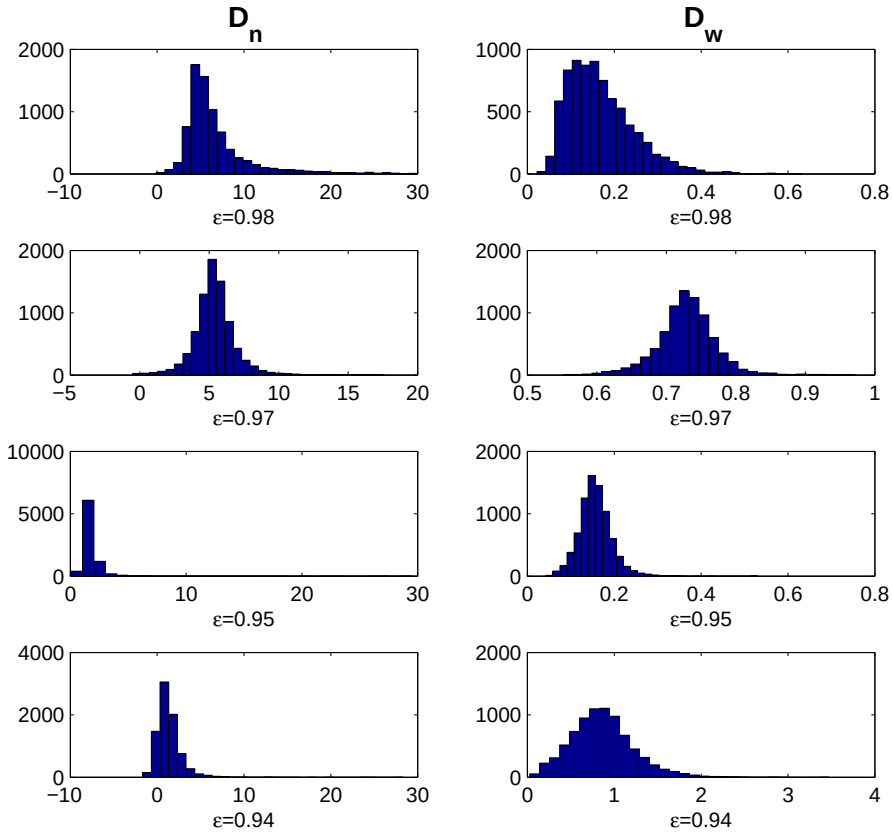

Figure 5.4: Distributions of denitrification rates calculated using the B-IPT method of the coupled sedimentary nitrification-denitrification rate (D_n) in the sediments (left) and denitrification rates derived from dissolved NO_3^- contained in the water column diffusing into the sediments (right) at different values of ϵ

5.4 Discussion

Two of the four underlying assumptions of the IPT were difficult to validate in this study due to the narrow spread in enrichment ratios, compounded by the variability in D_n and D_w between incubations. Anammox in this system is likely to have minimal impact upon the production rates of $^{29}N_2$ due to the permeable sediments and hydrodynamic regime maintaining dissolved oxygen levels at near saturation in the near bottom water and upper layers of the sediments, confirmed by the redox profiles of Lauer (2005). It is therefore highly likely that the underlying assumptions of the IPT are valid in this study.

The B-IPT and the standard IPT technique yielded similar 'mean' production rates of $^{29}N_2$ and $^{30}N_2$. The difference between the techniques lay in the tighter 95% credibility intervals predicted by the B-IPT in comparison to the wide 95% confidence intervals predicted by the standard IPT. This difference is due to the non-parametric assumptions of the Bayesian Linear Regression used in the B-IPT technique. Bayesian Linear Regression is a non-parametric technique and is therefore more suited to applications where non-normal distributions are present, as in this study. The parametric assumptions of the Least Squares Linear Regression can cause an over-estimation of the 95% confidence intervals in these cases. The tighter credibility intervals predicted by the B-IPT yields a more informative and consistant 'prior' distribution for a stochastic denitrification parameter in biophysical-statistical models.

The measured denitrification rates were found to be quite low when com-

pared with other coastal denitrification studies that were reviewed in Steingruber *et al.* (2001). When the ratio of D_n and D_w is examined, less than 10% of the nitrate that is denitrified is derived from the water column; it originates almost exclusively from the nitrification zone in the oxic layer of the sediments. This is a key finding which highlights the importance of nutrient cycling within the sediments of Spencer Gulf. In areas that receive substantial loads of organic material to the sediment surface, it is expected that this will stimulate the benthic metabolism and enhance the *in situ* nitrification rate. As 90% of the nitrate that is denitrified originates from the nitrification zone of the sediments, denitrification may be stimulated in a similar way. The effect of organic matter originating from aquaculture activities on the sedimentary denitrification rate will be examined in more detail in Chapter 6.

Due to the tightly coupled nitrification/denitrification rate and the permeable nature of the sediments, small-scale variations in the sedimentary morphology caused by the hydrodynamic regime may contribute to the observed variability between cores in each of the incubations. It appears that inhomogeneities in the sediments that occur on the scale that sediment cores were collected, have a significant impact on the denitrification rates.

The variability between cores is evident in the predicted values of σ (Figure 5.5), which follow a distinctly log-normal distribution. The small-scale variability in some incubations were generally fairly low with σ ranging between 2 and 8, resulting in a coefficient of variation of between 10 and 20 %. The distributions of σ for the production rates of $^{30}N_2$ at $\epsilon = 0.94$ and 0.98, were larger by a factor of 5 to 10 times those of other distributions. This

directly affects the distributions of the production rates for these incubations and results in a wider spread of D_n rates for these incubations. It therefore appears that the production rate of $^{30}N_2$ displays higher variability between cores than that of $^{29}N_2$. This finding is supported by the wider 95% credibility intervals for these incubations, and raises the question, 'What is causing such high variability between cores?'

The physical and geochemical characteristics of the sediments are likely to play a significant role in determining the *in situ* denitrification rates. In permeable sediments subjected to oscillatory flows, generated by surface gravity waves, ripples form on the seabed. Under the combined influence of tidal currents and wave-induced orbital velocities, the biogeochemistry of the ripple crest and ripple base can be markedly different (Cardenas *et al.* , 2008). The predominant hydrodynamic regime causes flushing of the near surface porewater nutrients in the ripple crest, while the ripple base can generally be sheltered from this advective flux. Cardenas *et al.* (2008) and Huettel *et al.* (2003) found that permeable sediments subjected to oscillatory flow exhibited patchy variability in their geochemistry and related microbial communities between the crests and troughs of sand ripples. The porewater nutrients in the crest of the sand ripples are typically rapidly flushed and remain well oxygenated while the troughs are subjected to lower flushing rates and support higher denitrification rates. It appears that this mechanism is causing substantial variability in the sediments, which manifests itself in the high levels of variance seen in Figure 5.5.

A further improvement to the B-IPT procedure used in this study would be to investigate the covariance structure between the ^{29}PR and ^{30}PR, which

have thus far been ignored. By accounting for this covariance structure, it is likely that the posterior will be further constrained yielding even tighter 95% credibility intervals.

Other possible reasons for the observed variability in the sediments may relate to the existences of physical barriers such as scallop shells that may reduce the diffusive exchange of the porewaters with the overlying water column. The existence of microphytobenthos on the surface of the sediments may also act to enhance the denitrification rates when they are present. We did not observed any such material in our cores, although microphytobenthos biomass was not explicitly observed. It is also possible that benthic infauna may also act to enhance the denitrification rate. Benthic infauna biomass was not measured in this study.

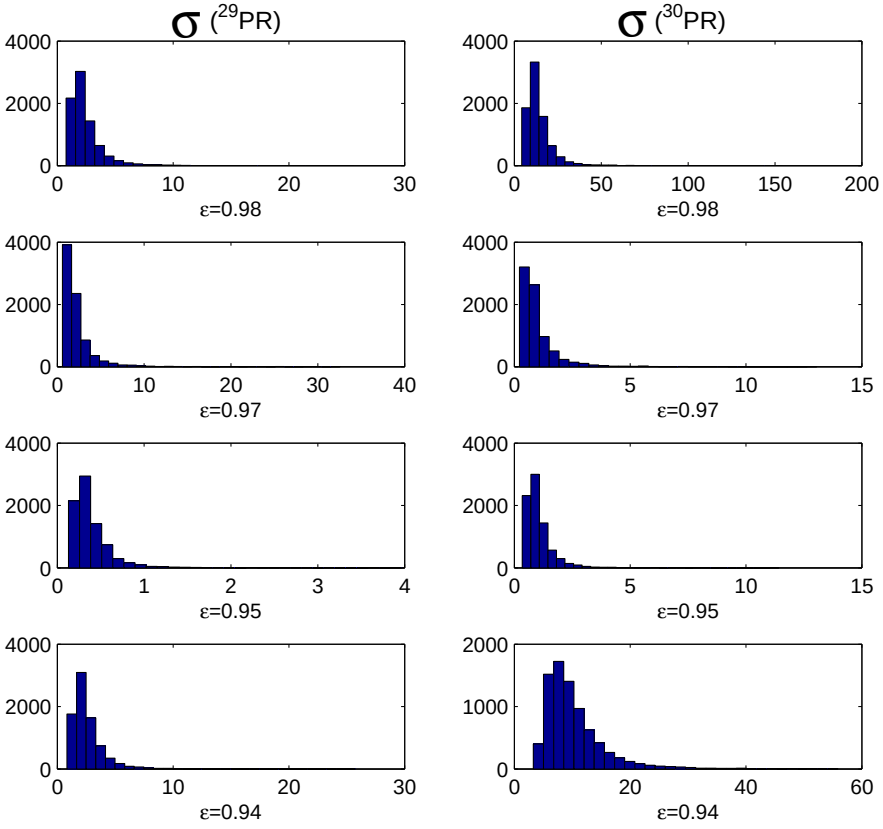

Figure 5.5: The distributions of σ for ^{29}PR (left) and ^{30}PR (right) for each value of ϵ.

5.5 Conclusion

A new approach using Bayesian Linear Regression has yielded distributions for the production rates of $^{29}N_2$ and $^{30}N_2$. This method explicitly accounts for differences between cores and can yield information on the effects of spatial variability through the precision parameter (τ). The mean production rates are comparable to those derived using standard Least Squares Linear Regression. The advantage of the Bayesian Linear Regression is tighter 95% credibility intervals when compared to those derived using standard Least Squares Linear Regression. The distributions of $^{29}N_2$ and $^{30}N_2$ were then propagated through the traditional IPT calculations of Nielsen (1992a), to yield distributions for D_n and D_w, this method has been referred to as the Bayesian Isotope Pairing Technique (B-IPT). By generating distributions of D_n and D_w, using a non-parametric procedure, this approach has the potential to lead to better constrained 'prior' information, that can be derived from non-normal distributions, for denitrification parameters in emerging physical-statistical biogeochemical models.

Denitrification rates were low (0.1-10 μmol m^{-2} h^{-1}) compared with many other coastal denitrification studies. The low denitrification rates were attributed to the energetic hydrodynamics of the site and coarse permeable nature of the sediments, which lead to systematic flushing of the porewaters.

To the author's knowledge, this is the first study to quantitatively estimate the small-scale spatial variability between cores in a denitrification study. This was achieved through explicitly including the variability through the parameter σ in the Bayesian Linear Regression algorithm. This is of

significant benefit if working in heterogeneous sediments. To quote R. A. Fisher:

> *'Uncertainty does not preclude rigour, provided the degree of uncertainty is known.'*

The standard and Bayesian approaches applied in this study have given comparable estimates of denitrification rates in heterogeneous sediments, but the Bayesian approach extracts more information from the experimental data, returns a better estimate of the uncertainty, and provides a more rigorous basis on which to construct subsequent marine biogeochemical models.

Chapter 6

Denitrification: spatio-temporal variability

6.1 Introduction

The introduction of nutrients through anthropogenic activities, such as aquaculture, can lead to imbalances within the marine ecosystem (Buschmann *et al.* , 2006; Kalantzi & Karakassis, 2006). Complex spatially resolved marine biogeochemical (BGC) models are often used to investigate nutrient cycling pathways and the likely effects of various management scenarios (Wild-Allen *et al.* , 2004; Murray & Parslow, 1999; Arhonditsis & Brett, 2004). The process of denitrification in these models is often treated as a tuning parameter as there have been few studies that examine both the temporal and spatial variations in the nitrogen loss pathways. This lack of denitrification data in relevant environmental systems has often lead to poorly constrained models. Furthermore, there have been very few investigations of the impact of finfish

aquaculture on sedimentary denitrification rates (see however, Christensen *et al.* (2000)).

The most commonly perceived impact of aquaculture on the marine ecosystem is the deposition of waste, composed of uneaten feed and metabolites, to the seabed surrounding the pens (Kalantzi & Karakassis, 2006). Ecologically, the effects of aquaculture depend on the inherent hydrodynamic circulation of the area. In regions of moderate to strong flushing, wastes are dispersed over an area of up to 100 m, with the epibenthic impact decreasing with distance from the pontoon edge (Cheshire *et al.* , 1996a,b). In areas of weak flushing there is a more concentrated area of waste deposition, typically confined to within 35 m of the perimeter of the pontoon (Crawford, 2003; Edgar *et al.* , 2005). However, the findings of Vita & Marin (2007) show that northern bluefin tuna aquaculture in the western Mediterranean affects the benthos up to 220 m from the pontoon boundary. Findings of Chapter 4 suggest a more subtle impact associated with southern bluefin tuna aquaculture in Spencer Gulf, leading to silt build up over a much larger area and changes in the textural and geochemical characteristics of the sediments on a regional scale. The disparity between these findings is linked to hydrodynamic conditions and the nature of the wastes associated with different industries.

The aquaculture industry within Spencer Gulf (Figure 6.1) stems from the reduction of the Southern Bluefin Tuna (SBT) quota from 14500 tonnes in 1988/1989 to the current level of 5265 tonnes. The wild-caught fish are subjected to a value-adding aquaculture program similar to the feed-lotting of livestock. This aquaculture has increased from 17 tonnes of farmed tuna in 1991, to 5000 tonnes currently. Since 1997 the SBT farms have been relocated

from the protected waters of Boston Bay, to the outside of Boston Island in south-west Spencer Gulf. The relocation was prompted by a sediment resuspension episode in 1996, affecting sites mostly within Boston Bay. This event led to the mortality of approximately 75% of the farmed tuna (Clarke, 1996). It is thought that the present location is less prone to events that may lead to mass mortalities, as the higher current speeds of the area are thought to disperse waste products over a wider area.

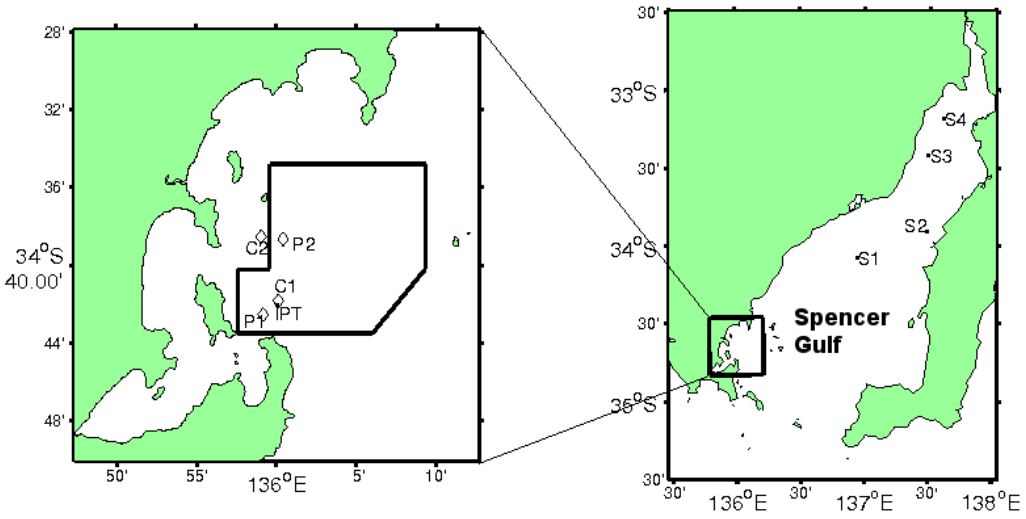

Figure 6.1: Map of the study region in south-west Spencer Gulf (left) showing the study sites. The approximate location of the tuna farming zone (black boundary) and the Spencer Gulf regional sites (right) where benthic flux data is also available (S1 to S4).

Historically there have been very few studies that have examined the nutrient and biogeochemical regime of Spencer Gulf, let alone in the tuna farming zone near Port Lincoln. Smith & Veeh (1989) report the findings from field observations taken between the 27^{th} and 30^{th} of May 1987, whereby water samples were collected at 25 sites between the entrance and head of Spencer Gulf. When examining the results from this study one must keep in

mind that the data only accounts for a snapshot in time. It was found that fishery yield from this system accounted for an unusually low proportion of the primary production. This was attributed to the low nutritional value of the seagrass in the system which was 20-30% of the value derived from planktonic carbon. Smith & Veeh (1989) suggested that N requirements in Spencer Gulf are met by N fixation. The limiting nutrient may be P, but against this is the observation that only 90% of the phosphate in the water column is removed by primary production. It is possible, therefore, that some other material is exhausted before P, thus allowing 10% P to remain in the system. On short time scales it may be that the system is limited by N or other trace elements. Indeed, the recent findings of Thompson *et al.* (2009) support those of Smith & Veeh (1989), suggesting that the limiting nutrient varies throughout the year, between N, P and Si. Furthermore, Thompson *et al.* (2009) suggest that the dynamics of nutrient limitation in SW Spencer Gulf are driven by a combination of seasonal flushing and nutrient regeneration in the sediments. The role of sedimentation within the Gulf is suspected to account for only a small fraction of the net organic production with most of the particulate organic matter being exported to the Southern Ocean.

The benthic metabolism in Spencer Gulf is discussed in Lauer (2005), who suggests that oxygen uptake rates and ammonium mineralisation in the vicinity of tuna pens exceed those found due to natural variability. When the raw flux data are examined (Figure 6.2), there are four notable features:

1. For all months the flux of dissolved inorganic nutrients from the sediments at the pontoon sites exceeds those at the control sites by up to

three orders of magnitude.

2. When the results are considered within the context of the annual residual circulation, there appears to be an upstream/downstream effect. The fluxes at sites C2 and P2 are greater than those at the downstream sites of C1 and P1.

3. During the tuna farming season from May until July, the PO_4^{3-} flux is at least the same magnitude as, if not greater than, the combined NH_4^++NO_x flux. This is reversed during the summer months after the tuna farming season has ended. If organic material were being consumed in the sediments at approximately the Redfield ratio of 106:16:1 for C, N and P respectively, then one would expect the fluxes of NH_4 and NO_x to be far higher than the fluxes of PO_4^{3-}.

4. During May and July, the NH_4 flux is substantially larger than the NO_x flux. A difference of this magnitude is not seen at any of the control sites.

Sediment trap studies were conducted in parallel to the benthic flux studies in Lauer (2005), at the control sites C1 and C2 (Figure 6.3). Again there appears to be a seasonal cycle in the N:P ratios of the sinking particulate matter, which differs from the constant Redfield ratio of 16:1 for N and P respectively. This deviation from the Redfield ratios is likely to be driven by the leaching of labile nutrients from tuna faeces and particulate feed, which typically have low N:P ratios ranging between 2:1 and 4:1 (Fernandes *et al.* , 2007a). It therefore appears that the seasonal variation in N:P ratios is

linked to the seasonal stocking of the aquaculture pens in the tuna farming zone.

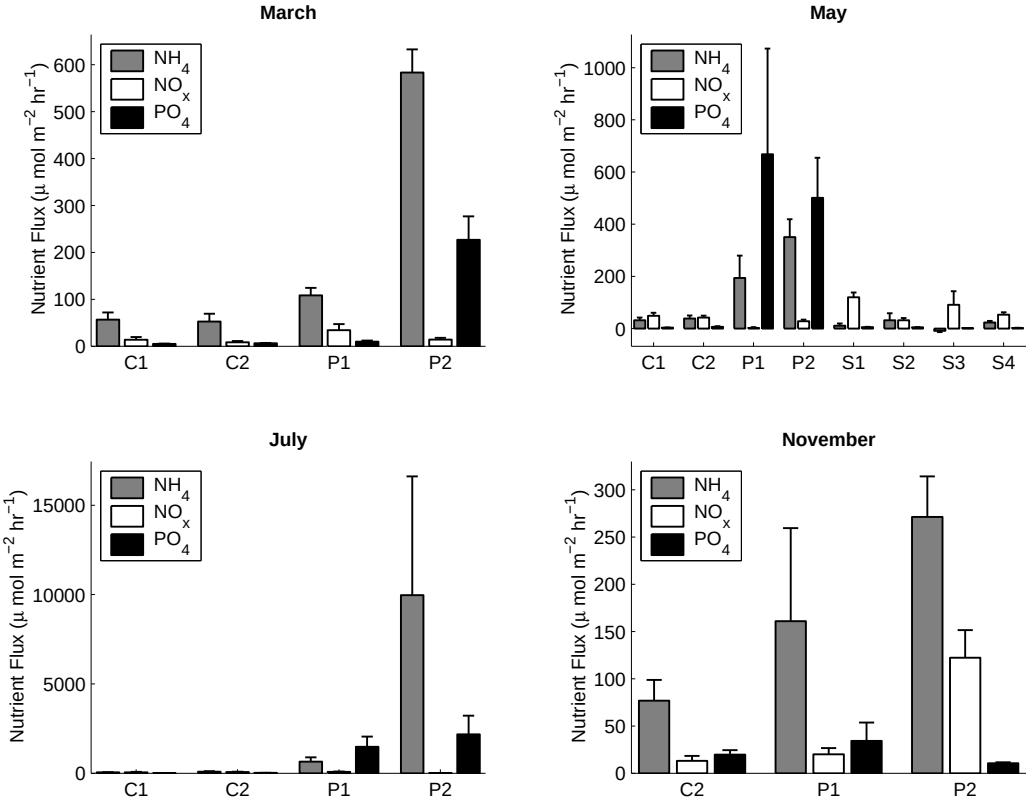

Figure 6.2: The benthic fluxes of NO_x, NH_4^+ and PO_4^{3-} for March, May, July and November 2004 in sites adjacent to tuna pens (P1 and P2), control sites within the tuna farming zone (C1 and C2) and within Spencer Gulf (S1 to S4) from Lauer (2005). For site location refer to Figure 6.1.

There have been no studies that examine the net loss of nitrogen from the system through advection, sedimentation or denitrification. Furthermore, it is also likely that dissimilatory reduction of nitrate to ammonia (DNRA) may also be taking place as the flux of NH_4^+ far exceeds that of NO_x. However, at the pontoon sites, there appears to be a net loss of dissolved inorganic nitrogen from the system, even when the process of DNRA is considered.

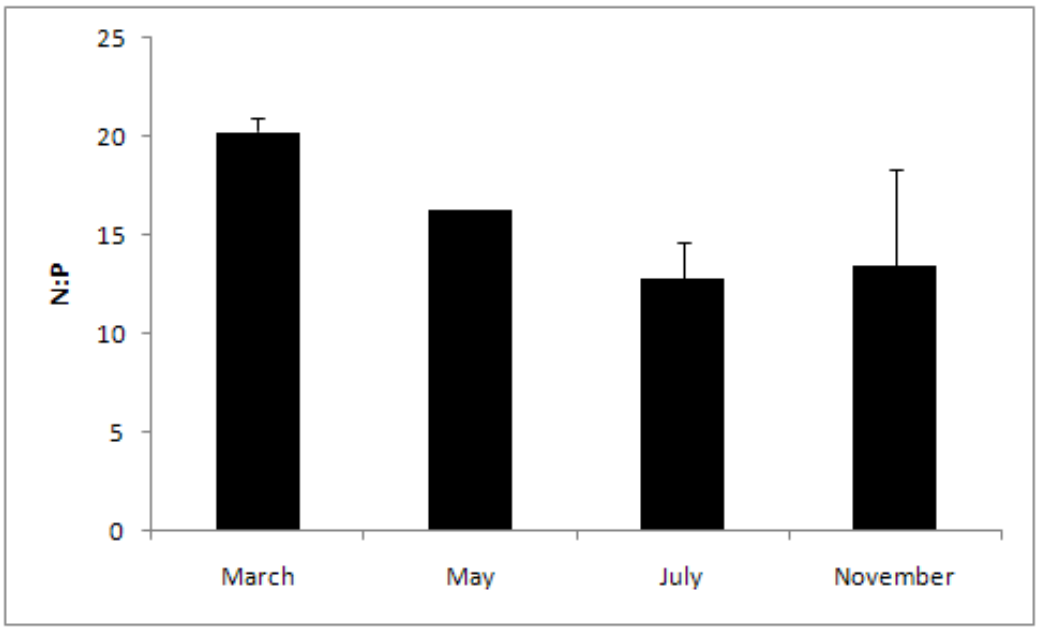

Figure 6.3: The N:P ratios of the sinking particulate matter collected during sediment trap studies in the tuna farming zone.

This chapter reports and discusses as follows:

1. Previously reported benthic nutrient flux data are used to infer the net denitrification rate at a number of sites in the tuna farming zone, and to compare these with other regions in Spencer Gulf.

2. The temporal and spatial variability in denitrification rates are assessed and are related to the regional aquaculture activities.

3. The effect of underlying physical and anthropogenic factors that influence the sedimentary nutrient cycling.

This is the first investigation to asses the impacts of high nutrient loads from intensive aquaculture activities on sedimentary denitrification rates in an otherwise oligotrophic system dominated by coarse calcareous sediments.

6.2 Methods

A list of symbols and abbreviations used in this chapter are contained in Table 6.1.

Table 6.1: List of symbols and abbreviations used in Chapter 6.

Symbol	Description	Units
IPT	Isotope Pairing Technique	-
B-IPT	Bayesian Isotope Pairing Technique	
ND	Net Denitrification	μmol m^{-2} hr^{-1}
NEM	Net Ecosystem Metabolism	μmol N m^{-2} hr^{-1}
DIN	Dissolved Inorganic Nitrogen Flux	μmol N m^{-2} hr^{-1}
DIP	Dissolved Inorganic Phosphate Flux	μmol P m^{-2} hr^{-1}
N	Nitrogen	μmol
P	Phosphate	μmol
NO_x	Nitrate + Nitrite	μmol
NH_4	Ammonium	μmol
PO_4	Phosphate	μmol

The study of Lauer (2005) investigated the effects of aquaculture on the benthic metabolism in the tune farming zone. In this study, intact sediment cores were collected and the oxygen uptake rates, benthic fluxes of dissolved inorganic nitrogen (DIN) and phosphorus (DIP) were recorded at the sites shown in Figure 6.1. Sediment trap studies also recorded the N:P ratio's of sinking particulate matter. This study takes a similar approach to LaMontagne *et al.* (2002), who used dissolved inorganic nutrient flux measurements to quantify nutrient regeneration in Waiquot Bay, Massachusetts. The benthic net ecosystem metabolism (NEM) can be estimated by the flux of dissolved inorganic carbon (DIC) from the sediments (Yamamoto *et al.* , 2008; Robson *et al.* , 2008; Kalnejais *et al.* , 1999). In the absence of DIC flux data, it is possible to derive estimate NEM from the DIP flux and the

particulate N:P ratio (Yamamoto *et al.* , 2008):

$$NEM = \Delta DIC \approx \Delta DIP \left(\frac{N}{P}\right)_{particle} \tag{6.1}$$

where Δ indicates a flux from the sediments. By subtracting the measured DIN flux from the the NEM, it is possible to evaluate whether there is a net loss or gain of DIN in the sediments, through the indirect measurement of the net denitrification (ND):

$$ND = NEM - \Delta DIN \tag{6.2}$$

If the ND flux is negative, then the benthic ecosystem is producing excess DIN, whereas if the value of ND is positive, there is a net loss of DIN which is assumed to be due to denitrification in the sediments. If there is a net loss of DIN from the system, it is possible to estimate the percentage of DIN lost, based on the denitrification efficiency:

$$ND_{efficiency} = \frac{ND}{NEM} \times 100 \tag{6.3}$$

6.3 Results

6.3.1 Comparison of the net denitrification and Bayesian Isotope Pairing Technique

Denitrification rates calculated using the Bayesian-IPT (see chapter 5) are similar to those estimated from the NEM at a similar site and month. The

denitrification rates obtained using B-IPT ranged from 2.8 to 20 μmol m^{-2} h^{-1}, while the benthic nutrient flux data used in the ND calculations predicted a mean denitrification rate for C1 in March of 28.2 μmol m^{-2} h^{-1}, with a 95% confidence interval ranging between -13.2 and 70.1 μmol m^{-2} h^{-1}. The ND rates displayed far greater variability, which we attribute to a difference in sampling methodology, i.e. ship deployed coring as opposed to diver collection, causing sampling over a greater area. An additional reason in the differences between B-IPT and ND rates arise from the B-IPT measurements occurring in early April of 2008, whereas the flux measurements were taken in March of 2004. The area exhibits a seasonal cycle (discussed below) where there is a transition from net denitrification in March to net nitrification in May. The IPT study was conducted during this transitional period.

6.3.2 Temporal variation in net denitrification rates

The ND rates calculated from the nutrient flux data of Lauer (2005) exhibit a strong seasonal cycle (Figure 6.4) and also substantial differences between the control sites (C1 and C2) and the aquaculture pontoon sites (P1 and P2). The seasonal variation in ND rates at C1 transition from denitrification in March (28.2 μmol m^{-2} h^{-1}) , through to nitrification in May (-21.4 μmol m^{-2} h^{-1}) and July(-30.9 μmol m^{-2} h^{-1}). The other control site (C2) behaves differently, with the ND rates suggesting year round denitrification, with a minimum in May of 28.4 μmol m^{-2} h^{-1} and peaking between July and November at 140 to 150 μmol m^{-2} h^{-1}.

The ND rates adjacent to aquaculture activities displayed a similar seasonal cycle to C2, except the magnitude of the denitrification rates were larger by a factor of approximately 1000. Sites P1 and P2 displayed a systematic increase in denitrification beginning in March and increasing over May and July, peaking at well over 20 mmol m^{-2} h^{-1}. The ND rates at each of these sites for November dropped dramatically, with P2 transitioning to net nitrification in the sediments. The denitrification rate at P1 declined to the same order of magnitude as the control site C1.

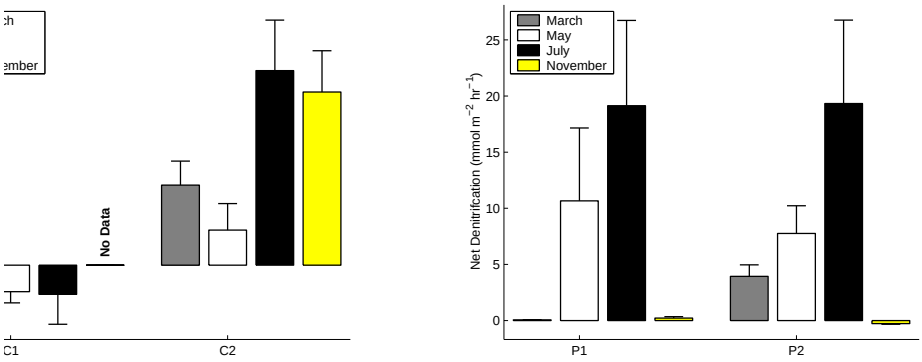

Figure 6.4: The ND rates calculated from the nutrient flux data at the control sites (C1 and C2) and near two tuna pontoons (P1 and P2). The bars indicate the standard deviation. There was no flux data for November at site C1.

6.3.3 Regional variation in net denitrification rates

The ND rates at the control sites (C1 and C2) and elsewhere in Spencer Gulf were calculated for May 2004 (Figure 6.5). The majority of ND rates indicated that the system was in net nitrification, with the exception of sites C2 and S3.

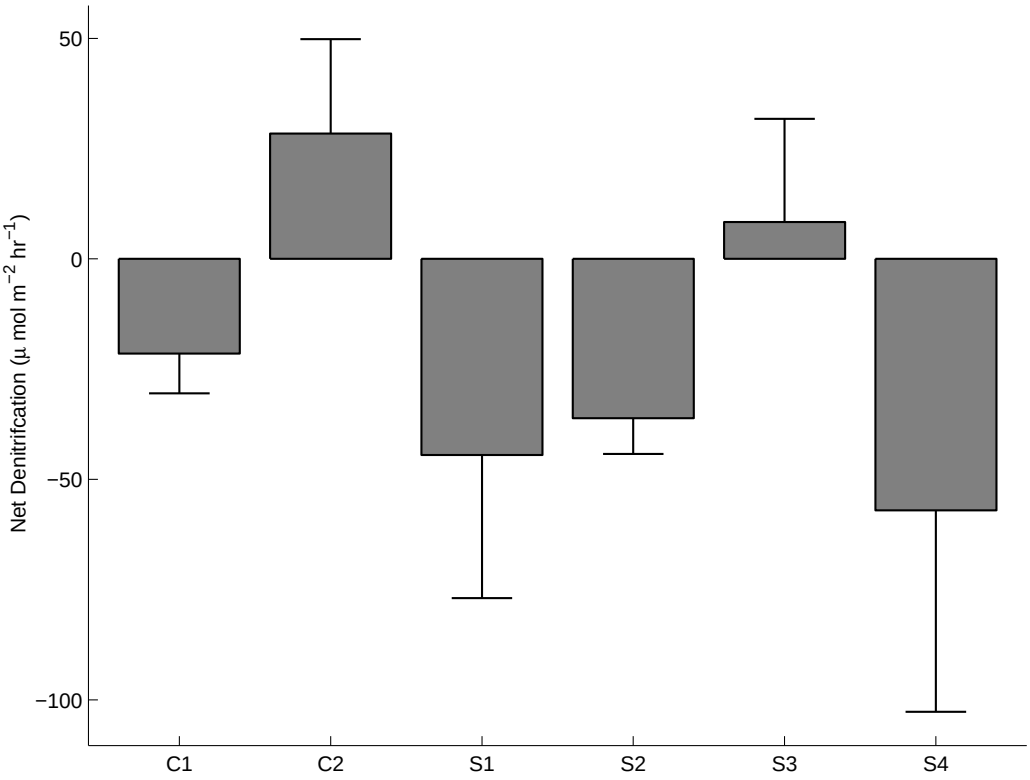

Figure 6.5: The ND rates during May for the control sites (C1 and C2) and regional Spencer Gulf sites (S1, S2, S3 and S4).

6.4 Discussion

There is good agreement between the B-IPT rates and ND rates calculated using the fluxes of DIN and DIP from the sediments. However, the variability between replicate cores is much higher for the ND rates. This is attributed to the sampling methods whereby cores were collected over a 10-20 m^2 area through the use of a ship deployed HAPS Corer (Lauer, 2005), whereas those cores used in the B-IPT method were collected by divers in a 1 m^2 area. Therefore the area of collection between replicate cores used for the estimation of ND rates is similar to the size of the area sampled between incubations in the B-IPT results (see Chapter 5). A second reason for the differences are due to the experiments being conducted in different years, albeit in a similar month and the same area.

The ND rates at C2 were substantially higher than those at C1 (which transitions to net nitrification from autumn onwards). There is an underlying difference in the physical nature of the two sites. C1 is afforded protection from incoming swell energy by Cape Donnington and is located in an area with a lower significant orbital velocity than C2 (see Chapter 3). This difference in wave regime has a direct impact on the textural characteristics of the sediments, which are comparatively finer at C1 when compared to C2 (Chapter 4). Furthermore, when the annual residual currents are examined, there is a clockwise circulation with oceanic waters entering the region from the south-east and advecting any dissolved and particulate organic matter to the north-west. Organic matter originating from aquaculture activities in the south-eastern section of the tuna farming zone is therefore advected past

C2 and during calm periods has the ability to settle out of the water column. It is therefore likely that there is a significant upstream-downstream effect in the tuna farming zone.

The ND rates at P1 and P2 appear to continue rising throughout the farming season and drop rapidly after harvest has occurred. There is no evidence that either site has approached its maximum capacity to remove DIN from the sediments. Both sites behave in a similar manner despite the underlying differences in wave regime, geochemical nature and management practices. This is surprising given that the tuna pontoons adjacent to P2 had a lower stocking density and a higher feeding rate than P1 (Lauer, 2005). P2 reverts to net nitrification at the end of the farming season, while P1 continues to remove DIN from the system. This may be explained by the variation in sediment type between the two sites, with the coarser sediments at P2 allowing a greater advective flux of nutrients out of the sediments and a deeper oxic zone for nitrification to take place.

The estimated ND rates are sensitive to the N:P ratios used in the calculation of the NEM. If the alternative N:P ratios are used at P1 and P2 derived from the tuna faeces (fed baitfish) reported in Fernandes *et al.* (2007a), this has significant ramifications for the calculated ND rates. The N:P ratios from the traps have a mean of approximate 16 with a range of between 12 and 20, which are close to Redfield ratios. This is an order of magnitude greater than N:P ratios of the faeces which have a mean 1.82 and a range of between 1.2-4.25 (Fernandes *et al.* , 2007a), which will essentially result in a reduction of the NEM by approximately one order of magnitude. Therefore the ND rates will reduce from around 15 mmol m^{-2} hr^{-1} to 1.5 mmol m^{-2}

hr^{-1}, also causing a reduction in the denitrification efficiencies. Regardless of the ratio used, DIN is being removed from the system under the aquaculture pens, while at the control sites DIN is being produced in the sediments.

The ND rates at all sites exhibited a seasonal cycle, with those adjacent to aquaculture activities having rates substantially higher than those at the control sites during the Austral winter. This period coincides with the SBT aquaculture season. During this period approximately 90% of the feed given to the tuna is excreted as organic matter into the water column (Fernandes *et al.* , 2007b). The direct result of this is the stimulation of benthic metabolism during this period (Lauer, 2005). If we assume that the effect of the tuna pontoons is limited to a 100 m radius, then approximately 2.2 - 7.13 mol N m^{-2} day^{-1} reaches the seafloor during the tuna farming season (Fernandes *et al.* , 2007b). The sediments adjacent to the pontoons have the ability to remove between 0.24 - 0.58 mol N m^{-2} day^{-1}, this represents a loss of approximately 4 - 25% of the particulate nitrogen reaching the seafloor. When these rates are presented as a fraction of the NEM, deemed the denitrifcation efficiency, benthic processes can remove approximately 80 - 90 % nitrogen flux predicted by the NEM during the tuna farming season (Figure 6.6). The control sites had substantially lower denitrifcation efficiencies, yet due to the upstream-downstream effect C2 had higher efficiencies than C1.

The effect of finfish aquaculture on the stimulation of benthic metabolism has also been throughly investigated by Christensen *et al.* (2000) albeit in a substantially different situation: the site was a relatively sheltered and shallow Fjord on the Danish coast; the species studied were sea trout. By contrast the tuna farming zone near Port Lincoln is exposed to energetic

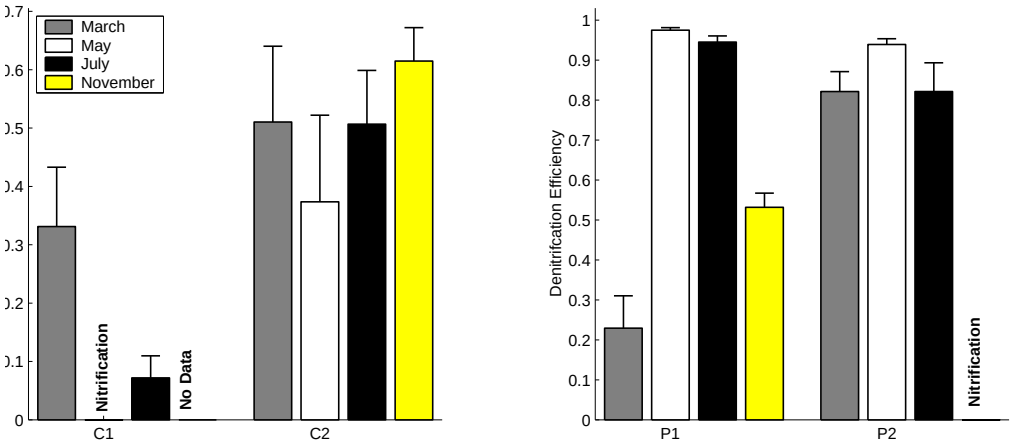

Figure 6.6: The net denitrification efficiencies calculated from the ND and NEM rates at the control sites (C1 and C2) and near two tuna pontoons (P1 and P2). There was no flux data for November at site C1.

hydrodynamic conditions. The denitrification rates adjacent to aquaculture activities in Christensen *et al.* (2000) were found to be comparable to the control sites, with the major nitrate loss pathway being through dissimilatory nitrate reduction to ammonia (DNRA). Our findings suggest a different response in the sediments. The fact that the NH_4 fluxes exceed the NO_3 flux, suggests that although the process of DNRA may be present, there is still a substantial net loss of DIN from the sediments; this must be interpreted as a loss through denitrification. This denitrification represents a fundamentally different response between the two studies. Adjacent to the aquaculture pens in Port Lincoln, nitrate is lost from the system via denitrification, whereas the transformation of nitrate to ammonia via DNRA merely represents a transfer of nutrients between two different nutrient pools. The similarity between the two systems lies in the stimulation of benthic metabolism through high organic matter loadings from aquaculture activities. There are, however,

stark differences in the nutrient cycling pathways.

Many denitrification studies have been conducted in sheltered environments where the sediments are dominated by cohesive muds. This leads to lower porewater flushing and a shallower oxygenated zone in the sediments, which in consequence support higher denitrification rates. The sediments adjacent to the aquaculture activities display higher fractions of silt-sized particles (Chapter 4). The presence of these finer grain size fraction reduces the permeability of otherwise coarse calcareous sediments. This decrease in permeability will lead to lower flushing of the porewater nutrients adjacent to aquaculture activities. Hopkinson *et al.* (2001) suggested that variations in nutrient fluxes from the sediments of eastern Massachusetts was due to sediment mixing or porewater flushing. Furthermore, the percentage of denitrified DIN displayed a positive correlation to depth, which, in the light of our results, would suggest that deeper sites were less influenced by surface waves.

In a study of the pelagic nutrient cycle of the tuna farming zone, Thompson *et al.* (2009) found that the limiting nutrient of the pelagic ecosystem was nitrogen between the months of February - August, phosphorus in September and silica in November. Thompson *et al.* (2009) also found there was little evidence of an external source (such as advection from the deep ocean) of N, P or Si suggesting remineralisation of nutrients within the Gulf is an important process.

The high denitrification rates in the fine nutrient rich sediments adjacent to aquaculture pontoons appear to limit the dissolved inorganic nitrogen flux from the sediments into the overlying water column, while at the control sites

the DIN flux into the water column was minimal. If the sediments followed a similar regime to those reported in Christensen *et al.* (2000), it is likely that the additional flux of nitrogen in the water column could stimulate significant levels of primary productivity. To this end it is favourable to the aquaculture industry that the sediments in the tuna farming zone are able to act as a sink for DIN.

The regional variation of ND rates during May elsewhere in Spencer Gulf suggested that a majority of the region was in net nitrification. If the Spencer Gulf behaves in a similar pattern to C1 in the tuna farming zone, then the sediments are likely to be removing DIN from the system during the Austral summer, while in winter this processes reverses and there is a net flux of DIN from the sediments.

The implications of this seasonal cycle, when examined in conjunction with the distinct hydrodynamic regions and flushing cycles identified in Kämpf *et al.* (2009), suggest that there are two distinct biogeochemical provinces within Spencer Gulf. This result agrees with the findings of Smith & Veeh (1989), who found that there was a distinct relationship between salinity and DIP, with the upper and lower regions of the Gulf behaving in a different manner. The area south of Wallaroo is flushed on an annual basis in response to the thermohaline flushing, while the upper region experiences flushing time scales 2-3 years. The lower region of the Gulf therefore responds to a combination of the local cycling of nutrients and the import/export of DIN from ocean waters. This is in contrast to the upper section of the Gulf, which is much more reliant of the local cycling of nutrients rather than an advective flux from the open ocean.

6.5 Conclusions

The ND rates derived using the nutrient flux data of Lauer (2005) range from -40 μmol m^{-2} h^{-1} (net nitrification) through to 120 μmol m^{-2} h^{-1} at the control sites. Aquaculture activities, suppling high organic loads to the sediment surface, stimulate the sedimentary denitrification rates which exceed those at the control sites by a factor of up to 1000.

The temporal variations in the ND rates at C1 and C2 are markedly different, largely due to the sediment types and the residual circulation. In the sediments of C1, there is a transition from net denitrification in the summer months, to net nitrification in the winter months. This is in contrast to the cycle at C2, where there is consistent denitrification occurring year round and peaking during November. The difference in behaviour is attributed to an upstream/downstream affect that causes a variation in organic matter reaching the sediment surface.

The net denitrification rates at aquaculture sites again follow a strict seasonal regime that differed from the control site C1. Both P1 and P2 peaked in July and had dramatically declined by November. The denitrification rates at these sites exceeded those at the controls by 3 orders of magnitude. The seasonal cycle corresponds remarkably well with the tuna farming season that sees an increase in stocking density during the Austral winter. During August nearly all of the tuna are harvested. It appears that the denitrification rates adjacent to the aquaculture sites are stimulated by the loading of organic matter from farm wastes. It is advantageous that the sediments remove the excess DIN produced in the sediments via denitrification, with

efficiencies as high as 90%; this reduces the DIN flux into the water column which could otherwise stimulate pelagic primary productivity.

The spatial variation in net denitrification calculated in May 2004 suggests that a majority of Spencer Gulf has transitioned to net nitrification at this stage supplying dissolved inorganic nitrogen to the water column. From the findings of this study and a review of the literature it is still unclear whether Spencer Gulf acts as a source or sink for dissolved inorganic nitrogen. We do however speculate that the importance of the nitrogen cycling as a source of DIN, varies throughout the region. In areas that are seasonally flushed in the lower half of Spencer Gulf, the combination of marine import/export of DIN may dominate over the flux of DIN from the sediments. The region north of Wallaroo, may rely heavily on the cycling of DIN through the sediments to supply a substantial fraction of the DIN required for primary productivity.

Chapter 7

General summary and conclusion

A major component of this study was to elucidate the linkages between the physical and biogeochemical conditions present in the tuna farming zone of south-west Spencer Gulf. From the study of Fernandes *et al.* (2006), it was apparent that the wave regime of this area influences the sediment biogeochemistry. A multidisciplinary approach using a combination of numerical models, field and laboratory studies has been applied.

The application of a wave model to the central coastline of South Australia facilitated the nesting of a high resolution grid that covered the tuna farming zone and adjacent coastal embayments. Two major mooring deployments were undertaken for the *in situ* validation of the wave model. There was excellent agreement between the observed and modelled wave heights at all *in situ* locations. Remotely-sensed wave data were also used in the validation of the wave model and a 10% negative bias was found south of Kangaroo

Island largely due to open ocean forcing which is derived from MesoWAM, the Australian Bureau of Meteorology's operational wave-forecasting model. There were substantial variations in the wave regime between the exposed southern coastline and the sheltered coastal regions in the gulfs. Within the tuna farming zone the exposed locations to the north and east of Cape Donnington experienced a mixture of swell and wind-waves with swell accounting for between 40% and 60% of the total wave energy. There is a strong east-west gradient in the swell energy, and it progressively decreases further inshore as the swell is dissipated due to bottom friction.

It is this interaction between the swell and seafloor which can cause sediment resuspension events in the tuna farming zone. Swell entering the region from directly south causes the greatest swell height. Winds from the north-east through to south-east generate the highest wind waves. However, due to their relatively short period, these wind-waves are generally not able to generate high bottom orbital velocities near the seafloor and therefore are not capable of eroding bed sediments. Swell that is refracted into the tuna farming zone generate the highest bottom orbital velocities.

To explore the relationship between the wave regime and textural characteristics of the sediments in the tuna farming zone, the relationship between the wave-induced bottom orbital velocity (U_b) and the sediment mean grain-size (MGS) was investigated. As the wave-induced bottom shear stress (τ_w) is proportional to U_b^2 and MGS, the variable of U_b^2 was used as a proxy for the wave induced bottom shear stress so as to remain independent of MGS. There was a statistically significant relationship between the mean value of the highest $\frac{1}{3}$ U_b^2 values and the MGS. I have called the highest $\frac{1}{3}$ U_b values

the significant orbital velocity (U_{sig}) which is analogous to the concept of significant wave height.

I found that sediments that had a mean grainsize less than 180 μm were not present in areas that were subjected to U_{sig} greater than 0.078 m s^{-1}. These results suggest that waves winnow out the fine grained sediments which are then advected by the residual currents and settle out in depositional areas. These areas are characterised as having high fractions of fine sediments and the U_{sig} velocities are typically below 0.07 m s^{-1}. From this relationship between U_{sig} and mean grain size I developed a seafloor classification map that was extended to cover the fine scale domain. Based on the seafloor classification, much of the tuna farming zone was found to be in a depositional region.

Sediment resuspension events have caused significant economic losses to the southern bluefin tuna aquaculture industry in the past. The management practices have been modified as a result and the tuna farming zone has been relocated to an area where there is increased dispersal of tuna wastes. A number of small sediment resuspension events were captured using the Echo Intensities (EI) from acoustic Doppler current profilers (ADCP). The relationship between τ_w and EI, differed between areas of coarse and fine sediment fractions. Where coarse fractions dominated, EI and τ_w followed a linear relationship. This is explained by the high settling velocities of the dominant coarse fractions. In areas dominated by fine sediments, as τ_w increases EI also increases but as τ_w decreases after a wave event, EI remains high due to the low settling velocities of the fine fractions. The vertical structure of the EI signal suggests that these regular resuspension events are

often contained in the lower 10 m of the water column and are indicative of the resuspension of a shallow 'fluff' layer of unconsolidated sediments, corroborating the modelling results of Margvelashvili (2009).

A spatial interpolation between sampling sites yielded insight into the spatial variation in sediment geochemistry. Three different cluster analyses concurred in defining two major geochemical provinces within south-west Spencer Gulf. A nutrient-rich region running through the central tuna farming zone contained porewater nutrient concentrations approximately twice those found elsewhere in the region. The isotopic signature of nitrogen in this area was heavier, suggesting increased microbial turnover of nutrients. The two geochemical provinces were not exclusively tied to the wave derived seafloor classification. Nevertheless, a majority of the zone did fall within the depositional classification. It therefore appears that the geochemistry is related not only to the ambient and physical characteristics but also to anthropogenic influences from aquaculture activities.

My results indicate that if a large, widespread sediment resuspension event took place, the advective release of porewater nutrients could increase the ambient concentrations of water column nutrients by between 1.4 and 10 times the background concentration. This represents a substantial increase in available nutrients in an otherwise oligotrophic region. If there were no other limiting nutrient (silica or iron), then it is likely that an algal bloom could be initiated.

The denitrification rates were examined in undisturbed natural sediments to the north of Cape Donnington. The Isotope Pairing Technique was applied to study the coupled sedimentary nitrification-denitrification rates and also

those due to the diffusion of dissolved nitrate into the sediments from the water column. There appeared to be some small-scale spatial variability within the sediments that manifested itself in the variable production of labeled dinitrogen gas during time-series incubation experiments. A new technique using Bayesian Linear Regression (BLR) was applied to quantitatively take into account this spatial variability. The BLR yielded discrete distributions for the production rates of labeled N_2, which were up to 25% tighter than those predicted with standard least squares linear regression techniques. The discrete distributions of labeled N_2 were then propagated through IPT calculations, referred to as Bayesian-IPT (B-IPT), yielding discrete distributions for the coupled nitrification-denitrification rates and also for the rates associated with the diffusion of dissolved nitrate from the overlying water column.

The ability of the B-IPT to quantitatively account for variability between replicate cores yields an objective metric to assess the effects of small scale spatial variability within the sediments. My findings enhance the work of Huettel *et al.* (2003) and Codispoti *et al.* (2001) through developing a technique that can quantitatively measure the variability associated with inhomogeneous permeable sediments in wave affected areas.

Another major advantage of using the B-IPT technique relates to the emerging field of biophysical-statistical modelling, whereby time derivatives of state variables are the result of stochastic processes, which could include sedimentary denitrification. The stochastic processes are formulated with stochastic parameters which are sampled from 'prior' distributions, the model is then evaluated against observations, yielding a 'posterior' distribution for the state variables and stochastic parameters. If using the standard IPT

method, for which a broad or uninformative 'prior' is implicit, the inference routine of the biophysical-statistical model would be far less efficient. Using the results from the B-IPT will increase the efficiency of an inference routine by providing an informative 'prior' from which to sample.

The spatial distribution and seasonal cycle in denitrification rates were inferred from the nutrient flux data collected by Lauer (2005). The net denitrification (ND) was calculated as the difference between the net ecosystem metabolism, estimated from the dissolved inorganic phosphate flux, and the observed dissolved inorganic nitrogen flux. Any difference between these two estimates was assumed to arise from the effect of denitrification. The inferred ND rates were similar to those obtained using the B-IPT method. At a control site in the south of the tuna farming zone, the seasonal cycle transitions from net denitrification in summer, to net nitrification in autumn and winter. The second control site examined, located near Rabbit Island, displayed year round denitrification which had a minimum in May and peaked in November. Elsewhere in Spencer Gulf, the sediments appeared to be in net nitrification during May. The ND rates adjacent to aquaculture activities were three orders of magnitude greater than those at the control sites, with maximum rates at the end of the tuna farming season in July. The supply of organic matter from the aquaculture activities appears to substantially stimulate the benthic metabolism, a finding in agreement with those of Lauer (2005).

There is a common underlying theme that connects the geochemical and biological processes operating within the tuna farming zone in south-west Spencer Gulf. The combined effect of the hydrodynamics and proximity to anthropogenic sources of organic matter have created a number of complex

interactions. Farm sites in depositional areas supply silty material to the sediments which reduces their permeability, which in turn reduces the advective exchange of porewater nutrients. Within the tuna farming zone, organic matter that reaches the seafloor is converted to dissolved inorganic nitrogen via ammonification and nitrification, which is efficiently denitrified within the sediments. High denitrification rates are possible in regions subjected to high loads of organic matter, which adjacent to aquaculture activities progressively increased throughout the farming season. The observed ND rates did not plateau and raises the question, '*What is the maximum possible denitrification rate adjacent to aquaculture activities?*'. Furthermore, there appears to be a strong upstream/downstream effect in the tuna farming zone, which is linked to a combination of the hydrodynamics and aquaculture, with the downstream control site denitrifying year round, in contrast to the upstream site. Elsewhere in Spencer Gulf, the nutrient cycling within the sediments may play an important role in the recycling of nutrients in areas with poor connectivity with open ocean waters.

The key findings of this thesis can be summarised as follows:

- Modelling results have identified that swell entering the mouth of Spencer Gulf from directly south causes the greatest swell heights in the central tuna farming zone.

- Winds from the north-east through to south-east generate the greatest wind-wave heights in the central tuna farming zone. This is directly related to the available fetch.

- There are regular resuspension events within the tuna farming zone,

several have been observed from echo intensity observations derived from moored acoustic doppler current profilers, these are typically confined to the lower 10 m of the water column.

- In the deeper central sections of the tuna farming zone swell poses the greatest sediment resuspension risk.

- In areas considered as depositional, fine fractions of sediments can build up leading to lower sediment permeability.

- The permeability of sediments and the proximity to aquaculture activities have direct implications for the porewater nutrients. In depositional areas near tuna farms the porewater nutrients were twice the concentration observed elsewhere in the region.

- The wave regime of the region causes small-scale spatial variability of the biogeochemistry within the sediments.

- The traditional approach to measuring denitrification in these sediments cannot explicitly account for this small scale spatial variability. The B-IPT technique developed in this thesis allows for this and results in tighter confidence intervals. Furthermore the B-IPT technique provides well constrained 'prior' distributions for the denitrification parameters in emerging biophysical statistical models.

- The net denitrification rates show seasonal variability and very steep spatial gradients.

- The combination of depositional regions and anthropogenic inputs can increase the net denitrification rate by three orders of magnitude.

- Adjacent to aquaculture pontoons, the denitrification efficiency in high, removing up to 90% of the DIN produced in the sediments.

Implications for aquaculture

Swell entering the Spencer Gulf from the south poses the greatest resuspension risk to aquaculture activities. The tuna farming zone is largely depositional with some erosional areas in the south east. Within the depositional zone there is some variation in textural characteristics which have direct implications in the ability of sediments to cycle nutrients and recover at the end of the tuna farming season. The finer sediments have a slightly greater capacity to remove dissolved inorganic nitrogen from the system via denitrification, with efficiencies $> 95\%$ during the tuna farming season. In contrast, coarser sediments have a lower efficiency ranging between 82% - 92%.

Here arises a dilemma; one could argue that the confinement of aquaculture activities to areas of fine sediments is beneficial due to the high denitrification efficiencies removing most of the dissolved inorganic nitrogen produced in the sediments. While on the other hand, in areas with coarse sediments, the slightly lower denitrification efficiencies combined with a high NH_4 flux due to dissimilatory reduction of nitrate to ammonia (DNRA), will lead to more dissolved inorganic nitrogen diffusing into the water column. However, if an extreme weather event occurs and resuspends large areas of sediments from the finer depositional zones containing high porewater nu-

trient concentrations, this will not only lead to the release of substantial amounts of nutrients into the water column but can also destroy the denitrification zone in the sediments. This has a two-fold impact on the pelagic ecosystem; extra nutrients may promote high levels of primary production and subsequent harmful algae blooms, while the sediments will no longer be able to remove excess nitrogen from the benthic ecosystem. Hence, the placement of tuna farms in higher energy environments is comparatively less risky.

This thesis has investigated the linkages between the inherent hydrodynamic regime of the tuna farming zone with the observed sediment biogeochemistry. While the sediments adjacent to aquaculture activities have been significantly altered, it appears that they are able to remove substantial quantities of dissolved inorganic nitrogen from the system. Several knowledge gaps exist that could not be answered by this study:

1. A more detailed investigation into the resuspension thresholds of the two textural sediment groups using flume studies will lead to a better assessment of the relative resuspension risk across the tuna farming zone.

2. The geochemical maps produced in Chapter 4 displayed fine scale variability that was difficult to investigate using our coarse grid. While the large scale trends have been captured, the local effects of aquaculture could be investigated more thoroughly with a finer sampling grid.

3. Using the dissolved inorganic nutrient fluxes from the sediments has indicated that there are high rates of denitrification adjacent to the

aquaculture pens. However, these results are sensitive to the N:P ratio used to estimate the net ecosystem metabolism. A more detailed study extending the B-IPT to measure the rates near these pens would result in a better understanding of the relative contributions of denitrification, DNRA and anaerobic oxidation of nitrate to ammonia.

Recommendations for future research and closing remarks

Suggestions for future research have been made throughout the discussion sections of many of the chapters. To recount these suggestions:

- The wave model applied in this study is forced with readily available forecast products, obtainable from the Bureau of Meteorology. Pilot tests have shown that it would be relatively straight-forward to apply this as an operational forecasting model forced with both winds and open ocean swell. This could be a useful tool in the forward planning of marine operations in this area, and if coupled with a hydrodynamic and sediment model, a useful management tool in predicting the onset of sediment resuspension events. Furthermore, if a real time wave instrument were located in the tuna farming zone, more accurate extreme statistics could be investigated.

- In the near future, the new Australian Community Climate and Earth-Systems Simulator (ACCESS) and the Australian implementation of the Wave Watch 3 (WW3) wave model, will have the ability to provide not only singular estimates of the wind and wave fields, but rather an ensemble of estimates, each slightly different. By forcing SWAN with

different combinations of these ensemble members, it will be possible to assess the degree of model uncertainty arising from the forcing data.

- Some geochemical variables will benefit from being sampled at a higher spatial resolution, this will yield better spatial interpolations with lower standard errors.

- Due to the Net Ecosystem Metabolism used to infer the Net Denitrification rates being particularly sensitive to the N:P ratio of the sinking particulate matter. It would be useful to extend the Bayesian Isotope pairing Technique study closer to the aquaculture activities to directly measure the denitrification rates adjacent to the tuna pontoons.

This thesis has used a combination of fieldwork, numerical modelling and laboratory studies to explore the relationships between the physical-mechanical processes, sediment biogeochemistry and aquaculture activities in south-west Spencer Gulf. This is the first study of its kind in this area and formed part of the Aquafin CRC: Risk and Response Project. The cross disciplinary nature of the studies presented in this thesis has provided a sound foundation for further research into physical and biogeochemical processes operating in this complex coastal region.

Appendix A

Bayesian Linear Regression

Before this approach is applied to the experimental data collected in the tuna farming zone, a proof of concept is given using a synthetically created dataset with known parameter values. The BLR approach is compared with the standard linear regression approach which will provide insight into the advantages and shortcomings of each method.

A.1 Introduction

If A and B are two random events, then the probability, $P[A \cap B]$ that both occur can be written in two ways:

$$P[A \cap B] = P[A].P[B|A] = P[B].P[A|B] \tag{A.1}$$

where P[A] and P[B] are 'prior' probabilities of A and B respectively and $P[B|A]$ and $P[A|B]$ are conditional probabilities. The above can be recast

as:

$$P[B|A] = \frac{P[B].P[A|B]}{P[A]} \tag{A.2}$$

which is commonly referred to as Bayes' theorem.

Applying this in the present context, we are treating the data as one random variable (A), and the parameter to be estimated (B) as the other. Then the above expressed in words is as follows;

'The probability that the parameters take on a given set of values, given our experimental results ($P[B|A]$) is equal to the prior probability of the parameter values ($P[B]$), multiplied by the conditional probability of the experimental data given the parameters ($P[A|B]$), divided by the probability of the experimental data, ($P[A]$).'

The first two terms constituting the numerator of equation A.1 are easy to calculate. Counter-intuitively the denominator, $P[A]$ need never be calculated, as it amounts to a normalising constant. To see this, consider that the sum of all possible probabilities for the parameter values must be one; they amount to a set of mutually exclusive and exhaustive outcomes. i.e,

$$\sum P[B|A]_{allpossibilities} = 1 \tag{A.3}$$

In practice, we can therefore initially ignore the denominator of equation A.1, we calculate the sum, over all possible parameter values, of the numerator $P[B].P[A|B]$, and that sum is necessarily the normalising constant $P[A]$.

The above describes the traditional Bayesian approach, which would have

been the simplest approach to the analysis of the data in the thesis. The parameter space has only three dimensions; PR, b and τ. A perfectly adequate approach would be to explore this parameter space by visiting each point on a 3D grid. In low dimensional space, a discretised grid is adequate, but as the number of parameters, n, increases, the strategy of visiting every point in n-space becomes computationally more expensive. For n of 3 or 4, a personal computer is adequate, but as n increases we require a computationally more efficient approach. The Monte-Carlo approach to Bayesian estimation will accommodate dimensions orders of magnitude higher (see, for example Gamerman & Lopes (2006)), and as the present state-of-the-art physical-statistical models typically contain 10 - 30 stochastic parameters (unpublished), the technique used in this thesis can be upscaled to explore the higher dimensional space of such models.

A.2 Formulation

To formulate this problem in a Bayesian framework, we use an underlying process model and an observation model. The process model is given by:

$$^{xx}N_2(t)_{process} = PR \times t + b \tag{A.4}$$

where $^{xx}N_2(t)_{process}$ μmol is the amount of labeled dinitrogen gas present in the incubation chamber at time t. PR μmol m^{-2} h^{-1} is the production rate of N_2 and b is the y-intercept. In the presence of small scale spatial variability

with measurement error, it is not possible to observe the true process. To this end an observation model is formulated and is given by:

$$^{xx}N_2(t)_{observed} =^{xx} N_2(t)_{process} + \zeta \tag{A.5}$$

where ζ is an additive error term that arises from small scale spatial variability in the sediments and measurement error. The measurement error on the GC-IRMS is small ($< 1\%$), therefore we assume ζ is dominated by the small scale spatial variability. ζ is drawn from the Gaussian distribution:

$$\zeta \sim \mathcal{N}(0, \sigma^2) \tag{A.6}$$

where σ^2 is the variance. If the sediment biogeochemistry were homogeneous, i.e. there was no small scale spatial variability in the sediments, σ^2 would be 0. The normal distribution ($\mathcal{N}$) is parameterised using the precision (τ) where $\tau = \sigma^{-2}$.

Therefore, we want to sample from the posterior distribution:

$$P[PR, b|^{xx}N_2(t)_{observed}] \tag{A.7}$$

Which reads, 'The probability of PR and b conditional on $^{xx}N_2(t)_{observed}$, which can be written as:

$$P[PR, b|^{xx}N_2(t)_{observed}] \sim \frac{\beta^\alpha}{\Gamma(\alpha)}\tau^{\alpha-1}e^{-\beta\tau}\prod_{i=1}^{n}\sqrt{\frac{\tau}{2\pi}}e^{\frac{-\tau(^{xx}N_2(t)_{observed}-^{xx}N_2(t)_{process})^2}{2}} \tag{A.8}$$

It is not possible to analytically solve the 'posterior', so an alternative approach is needed. It is possible to sample this distribution using the M-H MCMC algorithm (Gelman *et al.* , 2003; Gamerman & Lopes, 2006). The posterior has been parameterised such that PR and b are given a uniform (improper) priors on the interval [0,inf], and diffuse Gamma (Γ) for τ,

$$PR \sim U[0, \inf] \tag{A.9}$$

$$b \sim U[0, \inf] \tag{A.10}$$

$$\tau \sim \Gamma[\alpha, \beta] \tag{A.11}$$

The Gamma distribution is defined by the fixed parameters of α and β, which are each assigned values of 0.01 respectively. A thorough explanation of these techniques can be found in Gelman *et al.* (2003) and Gamerman & Lopes (2006). The underlying concept is that a Markov chain is created

with samples from the joint distribution of PR and b. Briefly, given a target distribution $p(X)$ and a proposal distribution $q(Y|X)$, where X is the parameter vector containing PR, b and τ, and Y is a vector containing the new proposals for PR, b and τ. The M-H MCMC algorithm generates a Markov Chain $X_1, X_2 \dots X_N$ from p. The chain is initialised at X_1 with reasonable estimates of PR, b and τ, a proposal Y is then drawn from the proposal distribution $q(Y|X_i)$ and this point is accepted with an acceptance probability (AP),

$$AP = min(1, \frac{P[Y]}{P[X]}) \tag{A.12}$$

If the candidate Y is accepted then $X_{i+1} = Y_i$, otherwise $X_{i+1} = X_i$. The chain X, will then converge towards the posterior $P[PR, b|^{xx}N_2(t)_{observed}]$.

A.3 Synthetic Data Generation

As a proof of concept, a synthetic dataset using known values for PR and b with additional artificial noise ζ was created to compare the results using LSLR and BLR. The synthetic dataset was created using the following 2 step procedure:

1. Using the process model A.2 'true' values of $N_2(t)$ are generated, where the parameters are set to: $PR = 8$, $t = 0 \dots 6$, $b = 20$.

2. Synthetic observations are then generated using the observation model where i.i.d. white noise, $\zeta \sim \mathcal{N}(0, \sigma = 8)$, is added to the 'true' values

of ${}^{xx}N_2(t)$. This represents field observations in the presence of small scale spatial variability.

A.4 Results

Both the LSLR and BLR techniques were applied to the synthetic dataset, yielding similar results with a few differences that are discussed below. A key performance measure in evaluating the results of the BLR is the 'mixing' displayed by the Markov Chains, for each of the parameters. 'Mixing' refers to the ability of the MCMC algorithm to efficiently explore parameter space. The Markov Chains displayed excellent mixing in parameter space and are shown to illustrate the concept of mixing (Figure A.1), and were subsampled every 20^{th} value to avoid any serial correlation that may be present. The least squares and Bayesian linear regression predicted the value for PR to be 8.28 and 8.23, respectively (Table A.1). Both methods over predicted the true value of the slope (PR) by approximately 3%. Tests with less additive noise resulted in estimations of PR very close to the 'true' value (not shown) by both methods. In the presence of substantial noise, the advantage of the Bayesian method was the tighter 95% credibility interval which extended from 2.54 to 13.84 giving a range of 11.3, which was 24% narrower than the LSLR confidence intervals. In natural systems the error term may not be Gaussian in nature, therefore the non-parametric assumptions underlying the Bayesian method can account for this, yielding substantial improvements over LSLR. Furthermore, is is possible to get a quantitative estimate of the error term, which is in this case is parameterised by τ. The pairwise plots

of PR, b and τ show a distinct correlation between PR and b, which was to be expected (Figure A.2). This relationship is also obvious in the two dimensional kernel density estimate (Figure A.3).

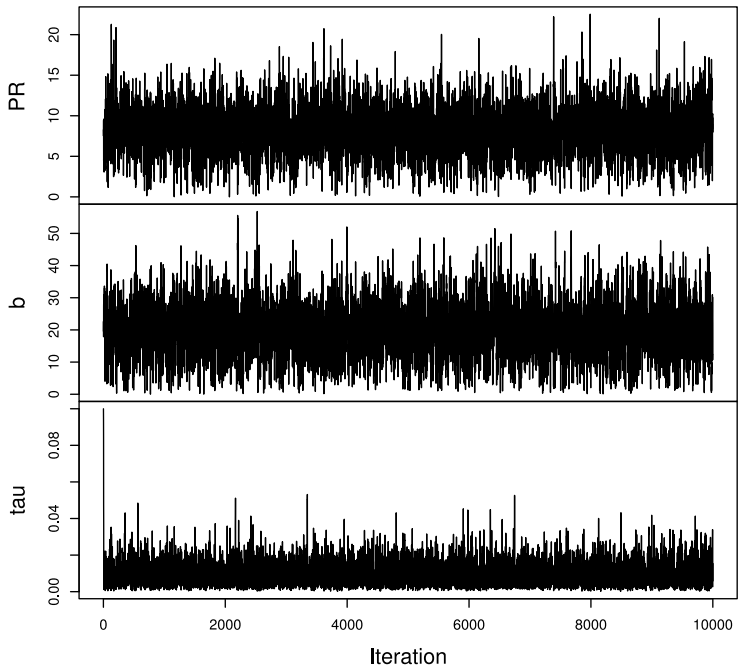

Figure A.1: The Markov Chain for the parameters PR, b and τ used in the synthetic dataset.

It is possible to get a quantitative estimate of the variability between the cores using the Markov Chain of τ. τ is related to the standard deviation (σ) via, $\sigma = \sqrt{1/\tau}$. Once again the assumption is that σ arises due to the

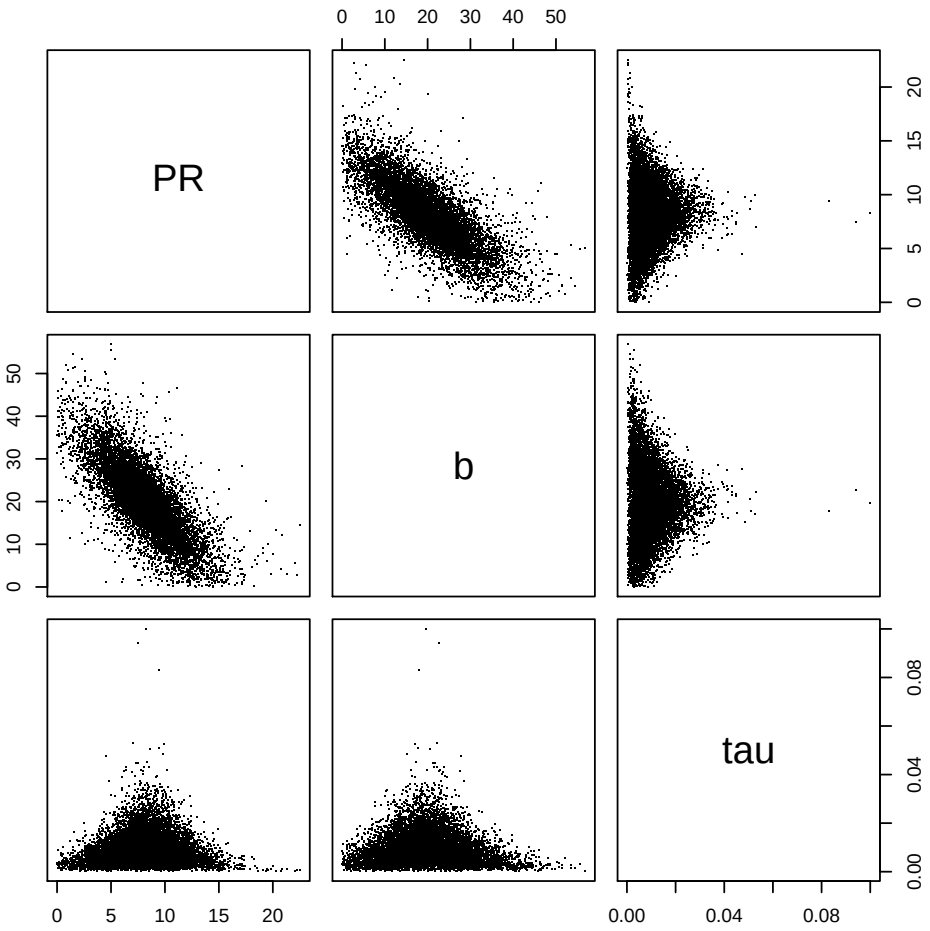

Figure A.2: Pairwise plot of the Markov Chain for the parameters PR, b and τ used in the synthetic dataset.

Table A.1: Comparison between the summary statistics of PR using Least Squares Linear Regression (LSLR) and Bayesian Linear Regression (BLR) from the synthetic dataset.

	Real Value	**LSLR**	**BLR**
Mean	8	8.28	8.23
Median	8	8.28	8.16
2.5%	-	1.25	2.54
97.5%	-	15.30	13.84
$\mathbf{R}^2$	1	0.72	-

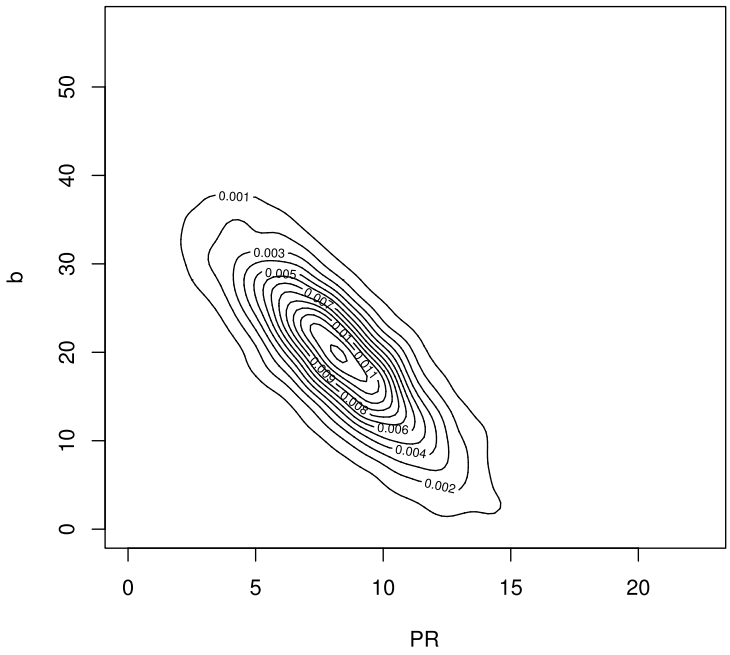

Figure A.3: The two-dimensional kernel density plot of the parameters PR and b. The true values were $PR = 8$ and $b = 20$.

heterogeneous nature of the sediments between cores. From the parameter estimation routine, σ is found to have a median value of 11.3, the histogram of σ (Figure A.4) displays a sharp peak around this value and is a slight overestimation of the prescribed real value of 8 used to generate the synthetic observations (Equation A.2).

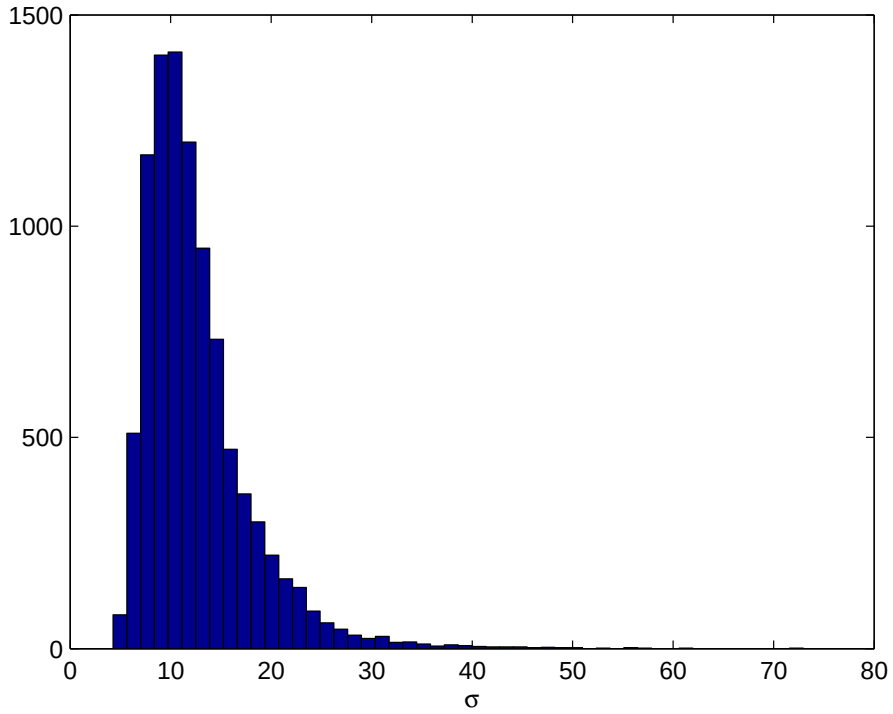

Figure A.4: The histogram of σ from the synthetic observational dataset.

Appendix B

Bayesian Linear Regression: Example R script

```
## Metropolis-Hastings sampler for Bayesian Linear Regression
blr.mh <- function(x,y,X1,q.sd,
                   alpha=0.01,beta=0.01,
                   iters=1000,sub=20) {

  ## The log posterior
  logp <- function(X) {
    f <- X[1]*x+X[2]
    sum(dnorm(y,f,1/sqrt(X[3]),log=T))+dgamma(X[3],alpha,beta,log=T)
  }

  ## Initialize X and Xs
  X <- X1
```

```
Xs <- matrix(0,iters,3)
colnames(Xs) <- c("PR","b","tau")

## Compute log posterior at X
logp.X <- logp(X)

for(k1 in 1:iters) {
  for(k2 in 1:sub) {
    ## Get next proposal point
    Y <- rnorm(3,X,q.sd)

    ## Ensure all components positive
    if(all(Y > 0)) {
      ## Compute log posterior at Y
      logp.Y <- logp(Y)
      ## Metropolis Hastings rule
      if(logp.Y - logp.X > log(runif(1))) {
        ## Proposal accepted - Y replaces X
        X <- Y
        logp.X <- logp.Y
      }
    }
  }
  ## Only sample the chain every sub iters
  Xs[k1,] <- X
```

```
  }
  Xs
}

## Read the synthetic data set
d <- read.table("synobs.txt",header=T)
lfit <- lm(X29N ~ Hour, data = d)
fit <- blr.mh(d$Hour,d$X29N,c(lfit$coefficients[2],lfit$coefficients[1],0.01),c(

## Estimate the posterior marginal means, standard deviations and
## quantiles
apply(fit[-(1:2000),],2,function(x)
      c(mn=mean(x),sd=sqrt(var(x)),quantile(x,c(0.025,0.5,0.975))))

summary(lfit)
confint(lfit)

## Plot the chains
plot(as.ts(fit),main="Markov Chains")

## Pairwise plots
pairs(fit,pch=".")

## 2D kernel density estimate for a,b
library(MASS)
```

```
dns <- kde2d(fit[(2000:10000),1],fit[(2000:10000),2],n=100)
contour(dns,xlab="a",ylab="b")

write.table(fit, "output.txt", row.names = F, sep = "\t")

## Cleanup
rm(blr.mh,d,fit,dns)
```

References

Alves, J., & Banner, M. L. 2003. Performance of a saturation-based dissipation-rate source term in modeling the fetch-limited evolution of wind waves. *Journal Of Physical Oceanography*, **33**(6), 1274–1298.

Arhonditsis, G. B., & Brett, M. T. 2004. Evaluation of the current state of mechanistic aquatic biogeochemical modeling. *Marine Ecology-Progress Series*, **271**, 13–26.

Babanin, A. V., & van der Westhuysen, A. J. 2008. Physics of 'saturation-based' dissipation functions proposed for wave forecast models. *Journal Of Physical Oceanography*, **38**(8), 1831–1841.

Blott, S. J., & Pye, K. 2001. Gradistat: a grain size distribution and statistics package for the analysis of unconsolidated sediments. *Earth Surface Processes and Landforms*, **26**, 1237–1248.

Booij, N., Ris, R. C., & Holthuijsen, L. H. 1999. A third-generation wave model for coastal regions - 1. Model description and validation. *Journal Of Geophysical Research-Oceans*, **104**(C4), 7649–7666.

Box, G. E. P., & Tiao, G. C. 1992. *Bayesian inference in statistical analysis*. Wiley classics library edn. New York: Wiley.

Brandes, J. A., & Devol, A. H. 1997. Isotopic fractionation of oxygen and nitrogen in coastal marine sediments. *Geochimica Et Cosmochimica Acta*, **61**(9), 1793–1801.

Buschmann, A. H., Riquelme, V. A., Hernandez-Gonzalez, M. C., Varela, D., Jimenez, J. E., Henriquez, L. A., Vergara, P. A., Guinez, R., & Filun, L. 2006. A review of the impacts of salmonid farming on marine coastal ecosystems in the southeast Pacific. *ICES Journal of Marine Science*, **63**, 1338–1345.

Cardenas, M. B., Cook, P. L. M., Jiang, H. S., & Traykovski, P. 2008. Constraining denitrification in permeable wave-influenced marine sediment using linked hydrodynamic and biogeochemical modeling. *Earth and Planetary Science Letters*, **275**(1-2), 127–137.

Cavaleri, L., Alves, Jhgm, Ardhuin, F., Babanin, A., Banner, M., Belibassakis, K., Benoit, M., Donelan, M., Groeneweg, J., Herbers, T. H. C., Hwang, P., Janssen, Paem, Janssen, T., Lavrenov, I. V., Magne, R., Monbaliu, J., Onorato, M., Polnikov, V., Resio, D., Rogers, W. E., Sheremet, A., Smith, J. M., Tolman, H. L., van Vledder, G., Wolf, J., & Young, I. 2007. Wave modelling - The state of the art. *Progress in Oceanography*, **75**(4), 603–674.

Cheshire, A., Westphalen, G., Kildea, T., Smart, A., & Clarke, S. 1996a. *In-*

vestigating the environmental effects of sea-cage tuna farming. I. Methodology for investigating seafloor souring. Tech. rept. University of Adelaide.

Cheshire, A., Westphalen, G., Smart, A., & Clarke, S. 1996b. *Investigating the environmental effects of sea-cage tuna farming. II. The effects of sea-cages.* Tech. rept. University of Adelaide.

Chester, R. 2003. *Marine Geochemistry.* 2 edn. Malden, MA: Blackwell Science Ltd.

Christensen, P. B., Rysgaard, S., Sloth, N. P., Dalsgaard, T., & Schwaerter, S. 2000. Sediment mineralization, nutrient fluxes, denitrification and dissimilatory nitrate reduction to ammonium in an estuarine fjord with sea cage trout farms. *Aquatic Microbial Ecology*, **21**(1), 73–84.

Christensen, P. B., Glud, R. N., Dalsgaard, T., & Gillespie, P. 2003. Impacts of longline mussel farming on oxygen and nitrogen dynamics and biological communities of coastal sediments. *Aquaculture*, **218**(1-4), 567–588.

Clarke, S. F. 1996. *Tuna Mortalities: April - May 1996.*

Codispoti, L.A., Brandes, J.A., Christensen, J.P., Devol, A.H., Naqvi, S.W.A., Paerl, H.W., & Yoshinari, T. 2001. The oceanic fixed nitrogen and nitrous oxide budgets: Moving targets as we enter the anthropocene? *Scientia Marina*, **65**(Suppliment 2), 85–105.

Cornwell, J.C., Kemp, W. M., & Kana, T.M. 1999. Denitrification in coastal ecosystems: methods, environmental controls, and ecostsem level controls, a review. *Aquatic Ecology*, **33**, 41–54.

Crawford, C. 2003. Environmental management of marine aquaculture in Tasmania, Australia. *Aquaculture*, **226**, 129–138.

Cressie, Noel A. C. 1993. *Statistics for spatial data*. Rev. edn. New York ; Chichester: Wiley.

Diego-McGlone, M. L. S., Azanza, R. V., Villanoy, C. L., & Jacinto, G. S. 2008. Eutrophic waters, algal bloom and fish kill in fish farming areas in Bolinao, Pangasinan, Philippines. Pergamon-Elsevier Science Ltd.

Dowd, M. 2006. A sequential Monte Carlo approach for marine ecological prediction. *Environmetrics*, **17**(5), 435–455.

Edgar, G. J., Macleod, C. K., Mawbrey, R. B., & Shields, D. 2005. Broad-scale effects of marine salmonid aquaculture on macrobenthos and the sediment environment in southeastern Tasmania. *Journal of Experimental Marine Biology and Ecology*, **327**, 70–90.

Eyre, B.D., Rysgaard, S., Dalsgaard, T., & Christensen, P.B. 2002. Comparison of istope pairing and N2:Ar methods for measuring sediment denitrification-Assupmptions, Modifications and Implications. *Estuaries*, **25**(6A), 1077–1087.

Falter, J. L., & Sansone, F. J. 2000. Hydraulic control of pore water geochemistry within the oxic-suboxic zone of a permeable sediment. *Limnology And Oceanography*, **45**(3), 550–557.

Fenton, J. D., & McKee, W. D. 1990. On Calculating The Lengths Of Water-Waves. *Coastal Engineering*, **14**(6), 499–513.

Ferguson, A. J. P., & Eyre, B. D. 2007. Seasonal discrepancies in denitrification measured by isotope pairing and N-2 : Ar techniques. *Marine Ecology-Progress Series*, **350**, 19–27.

Fernandes, M., Cheshire, A., & Doonan, A. 2006. Sediment geochemistry in lower Spencer Gulf, South Australia: implications for southern bluefin tuna farming. *Australian Journal of Earth Sciences*, **53**, 421–432.

Fernandes, M., M., Angove, T., Sedawie, & A., Cheshire. 2007a. Dissolved nutrient release from solid wastes of southern bluefin tuna (Thunnus maccoyii, Castelnau) aquaculture. *Aquaculture Research*, **38**(4), 388–397.

Fernandes, M., Lauer, P., Cheshire, A., & Angove, M. 2007b. Preliminary model of nitrogen loads from southern bluefin tuna aquaculture. *Marine Pollution Bulletin*, **54**(9), 1321–1332.

Fredsoe, J., & Deigaard, R. 1992. *Mechanics of Coastal Sediment Transport.* Advanced Series on Ocean Engineering, vol. 3. Singapore: World Scientific Publishing.

Fuller, M. K., Bone, Y., Gostin, V. A., & Von Der Borch, C. C. 1994. Holocene cool-water carbonate and terrigenous sediements from southern Spencer Gulf, South Australia. *Australian Journal of Earth Sciences*, **41**, 353–363.

Gamerman, D., & Lopes, H. F. 2006. *Markov chain Monte Carlo : stochastic simulation for Bayesian inference.* 2nd edn. Texts in statistical science 68. Boca Raton: Taylor and Francis.

Gelman, A., Carlin, J. B., Stern, H. S., & Rubin, D. B. 2003. *Bayesian data analysis.* 2nd edn. Texts in statistical science. Boca Raton, Florida.: Chapman and Hall, CRC Press.

Grzechnik, M. P. 2000. *Three dimensional tide and surge modelling and layered particle tracking techniques applied to southern Australian coastal seas.* Ph.D. thesis.

Guillen, J., Jimenez, J. A., Palanques, A., Gracia, V., Puig, P., & Sanchez-Arcilla, A. 2002. Sediment resuspension across a microtidal, low-energy inner shelf. *Continental Shelf Research*, **22**(2), 305–325.

Hamblin, P. F., Zhu, D. Z., Chiocchio, F., He, C., & Charlton, M. N. 2000. Monitoring suspended sediment plumes by optical and acoustical methods with application to sand capping. *Canadian Journal Of Civil Engineering*, **27**(1), 125–137.

Harmon, R., & Challenor, P. 1997. A Markov chain Monte Carlo method for estimation and assimilation into models. *Ecological Modelling*, **101**(1), 41–59.

Harris, P. T. 1994. Comparison of tropical, carbonate and temperate, siliciclastic tidally dominated sedimentary deposits: Examples from the Australian continental shelf. *Australian Journal of Earth Sciences*, **41**, 241–254.

Hasselmann, K., Barnett, T.P., Bouws, E., Carlson, H., Cartwright, D.E., Enke, K., Ewing, J.A., Gienapp, H., Hasselmann, D.E., Kruseman, P.,

Meerburg, A., Mller, P., Olbers, D.J., Richter, K., Sell, W., & Walden., H. 1973. Measurements of wind-wave growth and swell decay during the Joint North Sea Wave Project (JONSWAP). *Ergnzungsheft zur Deutschen Hydrographischen Zeitschrift Reihe*, **A(8)**(12), 95.

Hauser, Danile, Kahma, Kimmo, Krogstad, Harald E., Lehner, Susanne, Monbaliu, Jaak A. J., & Wyatt, Lucy R. 2005. *Cost Action 714 Measuring and analysing the directionalspectra of ocean waves.* Tech. rept.

Hecky, R. E., & Kilham, P. 1988. Nutrient limitation of phytoplankton in freshwater and marine environments - a review of recent-evidence on the effects of enrichment. *Limnology and Oceanography*, **33**(4), 796–822.

Hedges, J. I., & Stern, J. H. 1984. Carbon and nitrogen determinations of carbonate containing solids. *Limnology and Oceanography*, **29**, 657–663.

Heggie, D.T., Skyring, G.W., Orchardo, J., Longmore, A.R., Nicholson, G.J., & Berelson, W.M. 1999. Denitrification and denitrifying efficiencies in sediments of Port Phillip Bay: direct determinations of biogenic N2 and N-metabolite fluxes with implications for water quality. *Marine and Freshwater Research*, **50**, 589–596.

Hemer, M. A., & Bye, J. A. T. 1999. The swell climate of the South Australian Sea. *Transactions Of The Royal Society Of South Australia*, **123**, 107–113.

Herbert, R. A. 1999. Nitrogen cycling in coastal marine ecosystems. *Fems Microbiology Reviews*, **23**(5), 563–590.

Herzfeld, M., Middleton, J. F., Andrewartha, J., Luick, J., & Leeying, W. 2009. *Chapter 1. Hydrodynamic modelling and observations of the tuna farming zone, Spencer Gulf.* Tech. rept. South Australian Research and Development Institute.

Hollander, M. 1973. *Nonparametric Statistical Methods.* New York: Wiley.

Holthuijsen, L. H. 2007. *Waves in Oceanic and Coastal Waters.* 1 edn. New York, USA: Cambridge University Press.

Hopkinson, C. S., Giblin, A. E., & Tucker, J. 2001. Benthic metabolism and nutrient regeneration on the continental shelf of Eastern Massachusetts, USA. *Marine Ecology-Progress Series*, **224**, 1–19.

Huettel, M., Roy, H., Precht, E., & Ehrenhauss, S. 2003. Hydrodynamical impact on biogeochemical processes in aquatic sediments. *Pages 231–236 of: 9th International Symposium on the Interactions between Sediments and Water.* Banff, Canada: Kluwer Academic Publ.

Hulth, S., Aller, R. C., Canfield, D. E., Dalsgaard, T., Engstrom, P., Gilbert, F., Sundback, K., & Thamdrup, B. 2005. Nitrogen removal in marine environments: recent findings and future research challenges. *Marine Chemistry*, **94**(1-4), 125–145.

Jahnke, R., Richards, M., Nelson, J., Robertson, C., Rao, A., & Jahnke, D. 2005. Organic matter remineralization and porewater exchange rates in permeable South Atlantic Bight continental shelf sediments. *Continental Shelf Research*, **25**(12-13), 1433–1452.

Janssen, P.A.E.M. 1991. Quais-linear theory of wind-wave generation applied to wave forecasting. *Journal Of Physical Oceanography*, **21**(11), 1631–1642.

Kalantzi, I., & Karakassis, I. 2006. Benthic impacts of fish farming: Meta-analysis of community and geochemical data. *Marine Pollution Bulletin*, **52**, 484–493.

Kalnejais, L., McMahon, K., & Robb, M. 1999. Swan-Canning Estuary, Western Australia. *Pages 74–90 of:* Smith, S.V., & Crossland, C.J. (eds), *Australasian Estuarine Systems Carbon, Nitrogen and Phosphorus Fluxes. LOICZ Reports and Studies No. 12,.* Netherlands: Texel.

Kämpf, J. 2007. On the magnitude of upwelling fluxes in shelf-break canyons. *Continental Shelf Research*, **27**(17), 2211–2223.

Kämpf, J., Brokensha, C., & Bolton, T. 2009. Hindcasts of the fate of desalination brine in large inverse estuaries: Spencer Gulf and Gulf St. Vincent, South Australia. *Desalination and Water Treatment*, **2**, 325–333.

Karl, D., Michaels, A., Bergman, B., Capone, D., Carpenter, E., Letelier, R., Lipschultz, F., Paerl, H., Sigman, D., & Stal, L. 2002. Dinitrogen fixation in the world's oceans. *Biogeochemistry*, **57/58**, 47–98.

Kemp, W. M., Sampou, P., Caffrey, J., Mayer, M., Henriksen, K., & Boynton, W. R. 1990. Ammonium recycling versus denitrification in Chesapeake Bay sediments. *Limnology and Oceanography*, **35**(7), 1545–1563.

Klein, H. 2003. Investigating sediment re-mobilisation due to wave action by

means of ADCP echo intensity data Field data from the Tromper Wiek, western Baltic Sea. *Estuarine Coastal And Shelf Science*, **58**(3), 467–474.

Knowles, R. 1982. Denitrification. *Microbiological Reviews*, **46**(1), 43–70.

Komen, G.J., Hasselmann, S., & Hasselman, K. 1984. On the existence of a fully developed wind-sea spectrum. *Journal Of Physical Oceanography*, **14**(8), 1271–1285.

LaMontagne, M., Astorga, V., Giblin, A. E., & Valiela, I. 2002. Denitrification and the stoichiometry of nutrient regeneration in Waquoit Bay, Massachusetts. *Estuaries*, **25**(2), 272–281.

Lauer, P. R. 2005. *Benthic metabolism addjacent to southern bluefin tuna (Thunnus maccoyii) pontoons in South Australia*. Ph.D. thesis.

Lawrence, D., Dagg, M. J., Liu, H. B., Cummings, S. R., Ortner, P. B., & Kelble, C. 2004. Wind events and benthic-pelagic coupling in a shallow subtropical bay in Florida. *Marine Ecology-Progress Series*, **266**, 1–13.

Lennon, G. W., Bowers, D. G., Nunes, R. A., Scott, B. D., Ali, M., Boyle, J., Cai, W. J., Herzfeld, M., Johansson, G., Nield, S., Petrusevics, P., Stephenson, P., Suskin, A. A., & Wijffels, S. E. A. 1987. Gravity currents and the release of salt from an inverse estuary. *Nature*, **327**(6124), 695–697.

Libes, S. M. 1992. *Introduction to Marine Biogeochemistry*. Brisbane: John Wiley and Sons.

Margvelashvili, N. 2009. *Chapter 4. Numerical modelling of the sediment*

dynamics in the Port Lincoln region. Tech. rept. South Australian Research and Development Institute: Aquatic Sciences.

McClatchie, S., Middleton, J. F., & Ward, T. M. 2006. Water mass analysis and alongshore variation in upwelling intensity in the eastern Great Australian Bight. *Journal Of Geophysical Research-Oceans*, **111**(C8).

McClatchie, S., Rogers, P. J., & McLeay, L. 2007. Importance of scale to the relationship between abundance of sardine larvae, stability, and food. *Limnology And Oceanography*, **52**(4), 1570–1579.

Middleton, J. F., & Bye, J. A. T. 2007. A review of the shelf-slope circulation along Australia's southern shelves: Cape Leeuwin to Portland. *Progress In Oceanography*, **75**(1), 1–41.

Middleton, J. F., & Platov, G. 2003. The mean summertime circulation along Australia's southern shelves: A numerical study. *Journal Of Physical Oceanography*, **33**(11), 2270–2287.

Murray, A.G., & Parslow, J.S. 1999. Modelling of nutrient impacts in Port Phillip Bay - a semi-enclosed marine Australian ecosystem. *Marine and Freshwater Research*, **50**, 597–611.

Natvik, L. J., & Evensen, G. 2001. Assimilation of ocean colour data into a biochemical model of the North Atlantic - Part 1. Data assimilation experiments. *Pages 127–153 of: 33rd International Liege Colloquium on Ocean Dynamics*. Liege, Belgium: Elsevier Science Bv.

Nielsen, L.P. 1992a. Denitrification in sediment determined from nitrogen isotope pairing. *FEMS Microbiology Ecology*, **86**, 357–362.

Nielsen, L.P., Brotas, V., Viaroli, P., Underwood, G., Nedwell, D. B., Sundbck, K., Rysgaard, S., Miles, A., Bartoli, M., Dong, L., Thornton, D.C.O., Ottosen, L.D.M., Castaldelli, G., & Risgaard-Petersen, N. 2000. *Protocol handbook for NICE - Nitrogen Cycling in Estuaries: a project under the EU research programme: Marine Science and Technology (MAST III).*

Nielsen, P. 1992b. *Coastal Bottom Boundary Layers and Sediment Transport.* Advanced Series on Ocean Engineering, vol. 4. Singapore: World Scientific Publishing.

Noye, J. 1984. Physical processes and pollution in the waters of Spencer Gulf. *Marine Geology*, **61**, 197–220.

Nunes, R. A., & Lennon, G. W. 1986. Physical property distributions and seasonal trends in Spencer Gulf, South Australia: an inverse estuary. *Australian Journal of Marine and Freshwater Research*, **37**, 39–53.

Paphitis, D., & Collins, M. B. 2005. Sediment resuspension events wihtin the (microtidal) coastal waters of Thermaikos Gulf, northern Greece. *Continental Shelf Research*, **25**, 2350–2365.

Pattiaratchi, C., Newgard, J., & Hollings, B. 2007. *Physical oceanographic studies of Adelaide coastal waters using high-resolution modelling, in-situ observations and satellite techniques.* Tech. rept. School of Environmental Systems Engineering, The University of Western Australia.

Petrusevics, P. M. 1993. SST Fronts in inverse estuaries, South Australia - Indicators of reduced gulf - shelf exchange. *Australian Journal of Marine and Freshwater Research*, **44**, 305–323.

Porter-Smith, R., Harris, P. T., Andersen, O. B., Coleman, R., Greenslade, D., & Jenkins, C. J. 2004. Classification of the Australian continental shelf based on predicted sediment threshold exceedence from tidal currents and swell waves. *Marine Geology*, **211**, 1–20.

Precht, E., & Huettel, M. 2003. Advective pore-water exchange driven by surface gravity waves and its ecological implications. *Limnology and Oceanography*, **48**(4), 1674–1684.

Ris, R. C., Holthuijsen, L. H., & Booij, N. 1999. A third-generation wave model for coastal regions - 2. Verification. *Journal Of Geophysical Research-Oceans*, **104**(C4), 7667–7681.

Robson, BJ., Bukaveckas, P., & Hamilton, D. 2008. Modelling and mass balance assessments of nutrient retention in a seasonally-flowing estuary (Swan River Estuary, Western Australia). *Estuarine, Coastal and Shelf Science*, **76**, 282–292.

Rogers, W. E., Hwang, P. A., & Wang, D. W. 2003. Investigation of wave growth and decay in the SWAN model: Three regional-scale applications. *Journal Of Physical Oceanography*, **33**(2), 366–389.

Sigman, D.M., Robinson, R., Knapp, A. N., van Geen, A., McCorckle, D. C., Brandes, J. A., & Thunell, R.C. 2003. Distinguishing between water col-

umn and sedimentary denitrification in the Santa Barbara Basin using stable isotopes of nitrate. *Geochemistry, Geophysics and Geosystems*, **4**(5), 1–20.

Smith, S.V., & Veeh, H. H. 1989. Mass Balance of Biogeochemically Active Materials (C,N,P) in a Hypersaline Gulf. *Estuarine, Coastal and Shelf Science*, **29**, 195–215.

Smyth, C., Hay, A. E., Hill, P. S., & Schillinger, D. 2006. Acoustic observations of vertical and horizontal swimming velocities of a diel migrator. *Journal Of Marine Research*, **64**(5), 723–743.

Steingruber, S. M., Friedrich, J., Gachter, R., & Wehrli, B. 2001. Measurement of denitrification in sediments with the 15N isotope pairing technnique. *Applied and Environmental Microbiology*, **67**(9), 3771–3778.

Tanner, J. E., & Volkman, J. K. 2009. *Aquafin CRC - FRDC Southern Bluefin Tuna Aquaculture Subprogram : risk and response : understanding the tuna farming environment*. West Beach, SA: Aquafin CRC.

Thompson, P., Fernandes, M., Tanner, J., Volkman, J., Wild-Allen, K., Jones, E. M., & van Ruth, P. 2009. *Chapter 5. Nutrients*. Tech. rept. South Australian Research and Development Institute: Aquatic Sciences.

Tragou, E., Zervakis, V., Papageogiou, E., Stavrakis, S., & Lykousis, V. 2005. Monitoring the physical forcing of resuspension events in the Thermaikos Gulf - NW Aegean during 2001-2002. *Continental Shelf Research*, **25**, 2315–2331.

Trimmer, M., Risgaard-Petersen, N., Nicholls, J. C., & Engstrom, P. 2006. Direct measurement of anaerobic ammonium oxidation (anammox) and denitrification in intact sediment cores. *Marine Ecology-Progress Series*, **326**, 37–47.

van der Westhuysen, A. J., Zijlema, M., & Battjes, J. A. 2007. Nonlinear saturation-based whitecapping dissipation in SWAN for deep and shallow water. *Coastal Engineering*, **54**(2), 151–170.

Vita, R., & Marin, A. 2007. Environmental impact of capture-based bluefin tuna aquaculture on benthic communities in the western Mediterranean. *Aquaculture Research*, **38**(4), 331–339.

Wild-Allen, K., Parslow, J.S., Herzfeld, M., Sakov, P., Andrewartha, J., & Rosebrock, U. 2004. *Biogeochemical Modelling of the D'Entrecasteaux Channel and Huon Estuary. Technical Report.* Technical Report. CMAR CSIRO.

Wu, R. S. S. 1995. The environmental impact of marine fish culture: Towards a sustainable future. Pergamon-Elsevier Science Ltd.

Yamamoto, T., Hiraga, N., Takeshita, K., & Hashimoto, T. 2008. An estimation of net ecosystem metabolism and net denitrification of the Seto Inland Sea, Japan. *Ecological Modelling*, **215**(1-3), 55–68.

You, Z. J. 2005. Fine sediment resuspension dynamics in a large semi-enclosed bay. *Ocean Engineering*, **32**(16), 1982–1993.